SCUOLA DI DOTTORATO
UNIVERSITÀ DEGLI STUDI DI MILANO-BICOCCA

Department of Materials Science

PhD program in Materials Science and Nanotechnology – Cycle XXXV

Quantum Mechanical Modeling of Physical and Chemical Properties of Fe_3O_4 Nanoparticles and Surfaces for Nanomedicine and Energy Conversion

Surname: Bianchetti

Name: Enrico

Registration number: 793668

Tutor: Prof. Cristiana Di Valentin

Coordinator: Prof. Marco Bernasconi

ACADEMIC YEAR 2021/2020

Contents

Chapter 1

Introduction

The first magnetic material known to human beings is magnetite (Fe_3O_4), whose natural crystals are shown in Figure 1.1. The first experience with magnetism was through Fe_3O_4 containing rocks: compass-like instruments based on Fe_3O_4 were already used for religious purposes in China as early as 200 BC. The development of Fe_3O_4-based compasses for navigation occurred in Europe as early as 850 AD. Fe_3O_4 was at the forefront of scientific discoveries in science also through the 20th century. For example, Fe_3O_4 was one of the first mineral structure solved by Bragg in 1915 [1], and one of the first metal-insulator transitions was reported for Fe_3O_4 by Verwey in 1939 [2]. Furthermore, Néel [3] made Fe_3O_4 the prototypical example of his theory of ferrimagnetism.

Fe_3O_4 belongs to the wide family of iron oxides. The iron oxides are all based on a close packed O^{-II} anion lattice, with high spin Fe cations occupying octahedrally (Fe_{Oct}) and tetrahedrally (Fe_{Tet}) coordinated interstitial sites. Under reducing conditions, wüstite ($Fe_{1-x}O$) is formed. It crystallizes in the rocksalt structure with Fe^{II} in octahedral sites and is often non-stechiometric due to cation deficiency. Under oxidizing conditions, haematite (α-Fe_2O_3) in formed. It crystallizes in the corundum structure with Fe^{III} in octahedral sites. Under intermediate conditions, there is the formation of magnetite (Fe_3O_4), an inverse spinel with Fe^{III} in the tetrahedral sites and a 50:50 mixture of Fe^{II} and Fe^{III} in octahedral sites. The direct oxidation of Fe_3O_4 converts the Fe^{II} to Fe^{III} without any changes in the inverse spinel structure and with the appearance of compensating Fe vacancies in the octahedral sublattice. In the case of extreme oxidizing conditions, all Fe atoms become oxidized to Fe^{III}, and maghemite (γ-Fe_2O_3) is formed. Even if γ-Fe_2O_3 is metastable against transformation to α-Fe_2O_3, it exists because the conversion from the inverse spinel to the corundum structure requires the O^{-II} lattice to be converted from the face-centered cubic to hexagonal close-packed one. On the contrary, transformation between $Fe_{1-x}O$, FeO_4, and γ-Fe_2O_3 is quite fluid because it only requires a rearrangement of the cations within the same face-centered cubic

Figure 1.1: Natural crystals of Fe_3O_4.

O^{-II} lattice.

The permanent magnetism in iron oxides arises from the exchange coupling between different cations sublattices [4, 5]. Since the Fe−Fe distances are too large for direct exchange, the superexchange through the O^{-II} anions (Fe−O−Fe) is dominant and controls the magnetic ordering. The sign of this interaction generates a variety of magnetic phases ranging from antiferromagnetic to ferrimagnetic going through a series of relatively exotic magnetic phases.

Nowadays, the most important use of iron oxides is as a source of Fe, which is subsequently processed to produce steel [6]. Rocks containing high amounts of haematite and magnetite are mined from the ground. The iron oxides are then easily reduced by carbo-thermal reduction ($Fe_2O_3 + 3CO \rightarrow 2Fe + 3CO_2$ and $Fe_3O_4 + 4CO \rightarrow 3Fe + 4CO_2$, respectively). Other common uses of iron oxides include coatings for corrosion protection and catalysts for industrial reactions, such as the water-gas shift reaction ($H_2O + CO \rightarrow H_2 + CO_2$) [7].

Recently, there has been a resurgence of interest by the scientific community into iron oxide materials. Tartaj et al. [8] describe how the exciting properties of iron oxides, together with their environmental friendliness, low biotoxicity, facile synthesis, natural abundance, and economic viability, make them suitable for a variety of applications in a wide range of emerging fields. The interest for the use of iron oxide nanoparticles (IONPs) in biomedical applications grew up because some of the iron oxide phases, being magnetic, can be manipulated by an external magnetic field. This property opens the possibility to exploit iron oxide systems as markers for magnetic separation of example cells, as carriers for targeted drug

delivery, and as heat sources for hyperthermia treatment against cancer [9–16]. Furthermore, in a specific size range, IONPs show a superparamagnetic behavior [17], making them suitable as contrast agents for magnetic resonance imaging (MRI) [9–16]. The promising applications in the fields of energy storage, in particular the use of α-Fe_2O_3 as an anode material for lithium ion batteries, were highlighted [18]. In addition, iron oxides are found to be promising materials for the storage and disposal of radioactive wastes, such as technetium compounds [19, 20]. α-Fe_2O_3 attracted interest also for the photoelectrochemical water splitting ($2H_2O \rightarrow O_2 + 2H_2$), which is a way to convert solar energy into chemical energy, i.e., chemical bonds, without the use of fossil fuels. Characteristics as oxidative robustness, band gap of ca 2 eV (in the range of visible light adsorption), and valence band edge potential (much higher to that required for water oxidation) provide a good starting point for the preparation of α-Fe_2O_3-based photoanodes [21, 22]. Similarly, Fe_3O_4 is found to be a promising material for the preparation of an efficient anode electrocatalyst for the electrochemical water splitting [23–26]. In this case, sunlight is substituted by the electricity as energy source to make the cell work. Finally, iron oxides may play a key role also in the chemical industry. Iron oxides-based catalysts are involved in the Fenton reaction, i.e., the decomposition of H_2O_2 that is used to oxidize and inactivate contaminants [27]. They are also involved in the Fischer-Tropsch process, which transforms carbon monoxide and hydrogen in liquid hydrocarbons [28]. This reaction is regaining attention because it is a key step in the production of liquid fuels from gasification of biomass. Another interesting example is given by the commercial production of styrene by dehydrogenation of ethylbenzene in presence of a large quantity of steam at 600-700 °C. Replacing the steam with CO_2 combined with iron oxides-base catalysts may be an energy-saving and environmental-friendly alternative [29].

Being involved in various crucial applications related to the above mentioned emerging fields, Fe_3O_4-based materials are one of the *hottest* topics in the scientific research worldwide. In the next paragraph the state of the art of magnetite bulk, surfaces, and nanoparticles (NPs) characteristics and properties is presented and discussed, together with the most relevant applications.

1.1 State of the art of computational and experimental studies on magnetite

1.1.1 Bulk

At room temperature, Fe_3O_4 crystallizes in an inverse spinel structure with O^{-II} anions arranged in a slightly distorted face-centered cubic lattice and high spin Fe cations occupying tetrahedral and octahedral interstitial sites (see Figure 1.2).

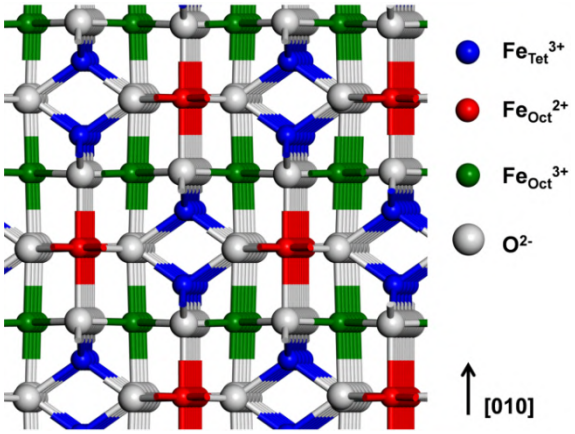

Figure 1.2: Structure of bulk magnetite. The color coding of the atoms is given in the legend on the right. Figure adapted from Reference [33].

Both divalent and trivalent Fe cations exist in Fe_3O_4, in a ratio of Fe^{II}:Fe^{III} = 1:2, with tetrahedral sites occupied by Fe^{III} and octahedral sites occupied by an equal number of Fe^{II} and Fe^{III}. The presence of unpaired electrons into the cations sublattices (Fe^{II} and Fe^{III} present high spin d^6 and d^5 configurations, and four and five unpaired electrons, respectively) determines the magnetism of Fe_3O_4. Below 858 K, Fe_3O_4 is a ferrimagnet with the cations at octahedral sites coupling antiferromagnetically with the cations at tetrahedral sites. As already mentioned in the previous section, the magnetic coupling between cations sublattices is determined by the superexchange through O^{-II} (Fe−O−Fe) [4, 5]. In Fe_3O_4, and more in general in spinels, the superexchange interaction in the case of Fe_{Oct}−O−Fe_{Oct} is ferromagnetic because the angle is close to 90°. On the contrary, in the case of Fe_{Oct}−O−Fe_{Tet}, being the angle close to 125°, it is antiferromagnetic, resulting in a net ferrimagnetic order because the number of the Fe_{Oct} cations is twice that of the Fe_{Tet} ones. The electrical conductivity of Fe_3O_4 is around 250 Ω^{-1} cm^{-1} at room temperature, like a poor metal [2, 30]. On cooling from room temperature to 120 K, the electrical conductivity decreases gradually and suddenly drops by two orders of magnitude at around 120 K, when the crystal structure changes from cubic to monoclinic symmetry [31, 32], which is called Verwey transition [2, 30].

Attracted by the puzzling Verwey transition, researchers devoted many efforts to the study of Fe_3O_4 electronic properties. By photoemission spectroscopy (PES) and scanning tunneling spectroscopy (STS), some of them concluded that Fe_3O_4 is (i) a half-metal above the Verwey transition temperature (T_V) because the valence band emission in PES [34–37] and the signal in STS [38] start from the vicinity of the Fermi level (E_F) and (ii) a semiconductor below T_V because a band gap of 0.14-0.30 eV exists at E_F. However, other researchers concluded that the band

gap in Fe_3O_4 did not collapse even above T_V. For example, using high-resolution PES, Park et al. [39] found that the band gap was merely reduced to ∼50 meV on heating through T_V. Later on, by a STS study, Jordan et al. [40] proposed that a ∼200 meV gap exists above T_V. More recently, a STS investigation conduced by Hevroni et al. [41] on Fe_3O_4 nanocrystals revealed that a band gap of 140-250 meV is present below T_V and of 75 ± 10 meV above it. At this point, it is clear that the electronic nature of Fe_3O_4 above T_V is still under debate, on the experimental side. On the contrary, from the theoretical side, all density functional theory (DFT) calculations for bulk magnetite in cubic phase led to a coincident conclusion, i.e., magnetite above T_V is half-metal ferrimagnet [42–46].

Another critical issue regarding Fe_3O_4, especially on the theoretical side, is the charge ordering. Verwey originally proposed that the statistical distribution of Fe^{II} and Fe^{III} at octahedral sites would lead to some type of order at low temperature [2]. In recent years, both experiments [32, 47–49] and DFT calculations [50–53] approved the charge ordering at octahedral sites below T_V. Above T_V, according to the Anderson's condition, the long-range charge ordering could be lost, whereas the short-range one should be maintained [54]. Recent X-ray diffuse scattering experiments conducted by Bosak et al. show that short-range charge ordering survives up to room temperature [55]. However, the DFT studies for Fe_3O_4 above T_V, i.e., in the cubic phase, converge in an average iron valence state of +2.5 at octahedral sites [42–46].

In order to put an end the debate on the electronic properties of Fe_3O_4 and solve the inconsistency between previous DFT calculations and X-ray diffuse scattering experiments on the charge order, Liu and Di Valentin recently reinvestigated theoretically Fe_3O_4 above T_V, i.e., in the cubic phase [33]. Through a wide set of DFT+U and hybrid functional calculations, imposing the symmetry constraint ($Fd\bar{3}m$ space group) only on atomic positions and not on electron density, they were able to predict a charge Fe^{II}/Fe^{III} disproportion. The charge difference between Fe^{II}_{Oct} and Fe^{III}_{Oct} is not 1.0 e but ∼0.3 e, which is similar to the charge ordering in the low temperature phase as reported before, and consequently enough to allow the arbitrary assignment of the +2 and +3 oxidation state. The calculated magnetic moments of Fe_{Tet} are -4.21 μ_B from HSE06, -4.14 μ_B from B3LYP, and -3.96 μ_B from PBE+U (U=3.5 eV), which are in good agreement with the experimental value of ~ -4.2 μ_B [56, 57]. In accordance with the charge disproportionation, the magnetic moments of Fe_{Oct} ions are also divided into two groups. Experimentally, because of the frequent hopping of electrons between Fe^{II}_{Oct} and Fe^{III}_{Oct}, an average magnetic moment at octahedral sites can be measured (3.97 μ_B [57]), which agrees well with Liu and Di Valentin's mean results (3.84 μ_B for PBE+U with U=3.5 eV, 4.03 μ_B for HSE06, and 3.98 μ_B for B3LYP). Furthermore, the adoption of DFT+U and hybrid functional approach, together with the release of

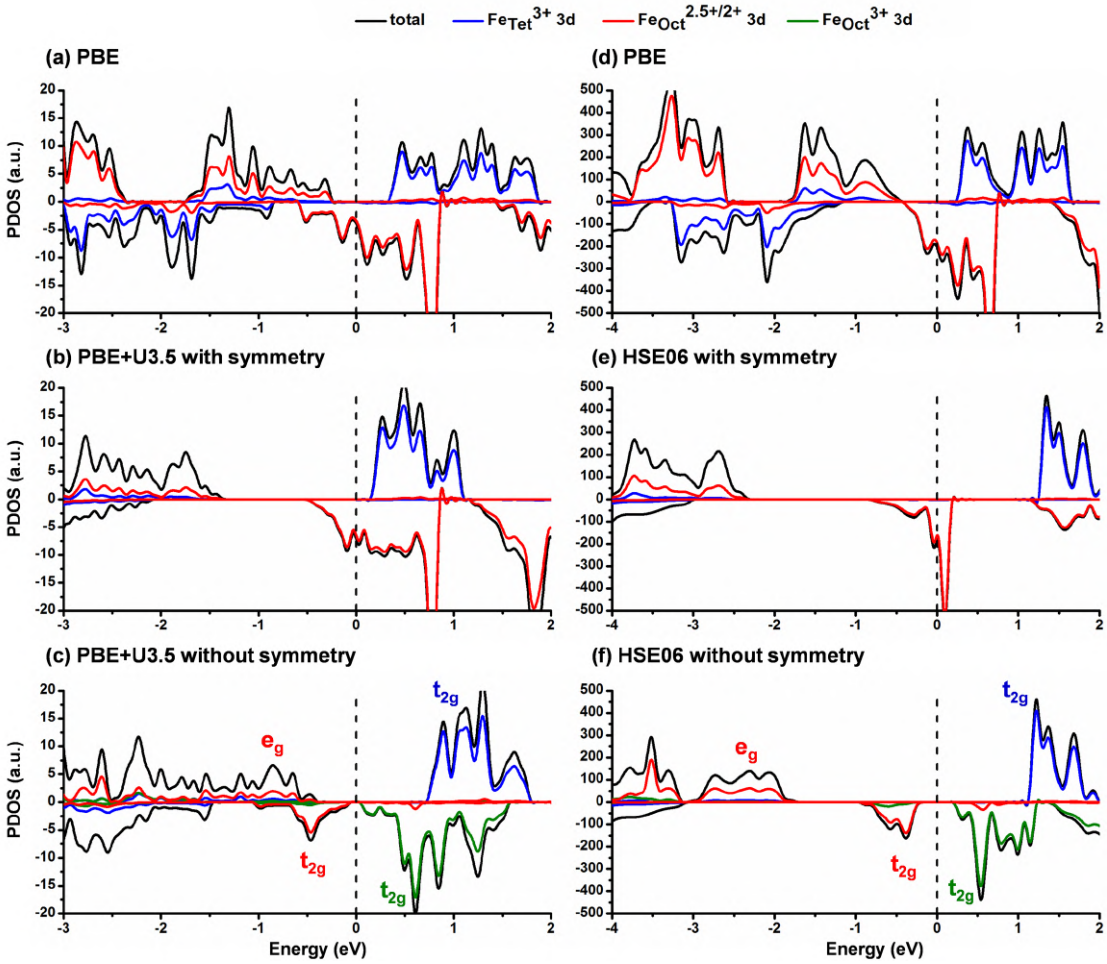

Figure 1.3: *Projected density of states* (PDOS) of bulk magnetite calculated at different levels of theory. The Fermi level is scaled to zero as indicated by the dashed black lines. The color coding is given in the legend on the top of the panels. Figure adapted from Reference [33].

the symmetry constraint on the electron density, allows the opening of a small band gap of 177 meV (in the spin down channel, as can be seen in Figure 1.3), in agreement with PES (100 meV) [39] and STS (75-200 meV) [40, 41] experiments. The original states from Fe_{Oct} (with an average valence state of +2.5) crossing E_F split into two parts, i.e., states from Fe^{II}_{Oct} below E_F and states from Fe^{III}_{Oct} above E_F, corresponding to the valence band maximum and conduction band minimum, respectively. These states are probably those involved in the electrons hopping between Fe^{II}_{Oct} and Fe^{III}_{Oct}, which is responsible for the Fe_3O_4 conductivity. In this sense, the energy barrier for electrons hopping from Fe^{II}_{Oct} to Fe^{III}_{Oct} is probably comparable with the band gap amplitude.

Based on these encouraging results, the computational setup proposed by Liu and Di Valentin in 2017 can be successfully adopted for studing Fe_3O_4-based nanostructures by means of DFT-based calculations.

1.1.2 Surfaces

Natural crystals of Fe_3O_4 (see Figure 1.1) are often octahedrally shaped and enclosed by (111) planes [6], although various different shapes can be grown by varying the synthesis conditions. Researchers focused in the past and still focus nowadays on the study and characterization of (110) and (001) planes, too, since they represent, together with the (111) one, the most stable low-index facets [58]. Several DFT-based calculations have been used several times to compare the surface energies and relative stability of (111), (110), and (001) Fe_3O_4 facets. For example, Yang et al. [59] found that (111) surface is less favorable thermodynamically than (110) and (001) ones, suggesting that the formation of (111) should be kinetically controlled. On the contrary, Yu et al. [60] found the (110) > (001) > (111) trend in terms of surface energies. More recently, Santos-Carballal et al. [61] calculated a Wulff construction (shown in Figure 1.4) enclosed by (001) and (111) planes, being the first surface more stable than the second. Experiments are in line with some of these results: Feld et al. [62] reported that NPs grows in [001] directions under thermodynamic control, whereas along [111] directions under kinetic control, as schematized in Figure 1.5.

From a structural point of view, the structure of the (110) facet is still under debate. In principle, there are two possibilities to truncate the bulk at the (110) plane, exposing either a layer of Fe_{Oct}, Fe_{Tet}, and O atoms, or a layer exposing only Fe_{Oct} and O. DFT calculations revealed that these structures, as well as various models including iron and oxygen vacancies, undergo significant relaxation with strong changes in the interlayer spacing [60, 63]. Scanning tunneling microscopy (STM), low-energy electron diffraction (LEED), and reflection high-energy electron diffraction (RHEED) experiments registered the exposure of (111) nanofacets onto the so-prepared (110) surface [64]. In other words, the Fe_3O_4(110) surface appears

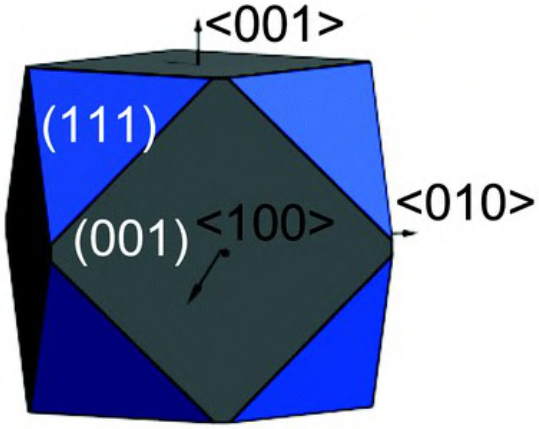

Figure 1.4: Wulff construction for Fe_3O_4 based on surface energies derived from DFT+U calculations. Figure adapted from Reference [61].

to be unstable against faceting to (111), in line with the DFT results mentioned in the previous paragraph [60, 61].

In the [111] direction the Fe_3O_4 structure is made up of six distinct planes of atoms, commonly denoted Fe_{Tet1}, O_1, Fe_{Oct1}, O_2, Fe_{Tet2}, and Fe_{Oct2} in the literature. The most commonly reported termination consists in a bulk termination at the Fe_{Tet1} plane, according to LEED and STM measurements and assignments [65–67]. Through DFT+U and hybrid functional calculations, a bulk termination at the Fe_{Oct2} plane is found to be competitive with the one just described at low oxygen chemical potentials, i.e., under reducing conditions [68]. This theoretical finding is in line with the major difficulty researchers encounter working with $Fe_3O_4(111)$: multiple termination can coexist in the same sample, depending on the preparation conditions [66, 67]. For example, Shimizu et al. [66] reported the coexistence of Fe_{Tet1} and Fe_{Oct2} planes, suggesting that could be due to the reduction of the sample surface through sputtering/anneal cycles. Furthermore, not only different terminations can coexist, but also different phases can do it. In particular, long-range superstructures made of $Fe_{1-x}O$ may appear between $Fe_3O_4(111)$ domains under reducing conditions [65, 69].

The structure and termination of the $Fe_3O_4(001)$ surface have also been discussed at length, too. The stacking sequence in the [001] direction consists of A layers that contain Fe_{Tet} and B layers that contain O and Fe_{Oct}. Different atomic structure models have been proposed for the (001) surface. An A layer termination, where half of the tetrahedral iron ions is missing, [71–73] and a B layer termination, with oxygen vacancies or hydroxyl groups, [74, 75] were proposed in the early stage. Later, based on DFT calculations, Pentcheva et al. [43] proposed a *clean* B layer termination called distorted bulk truncation (DBT) model, shown

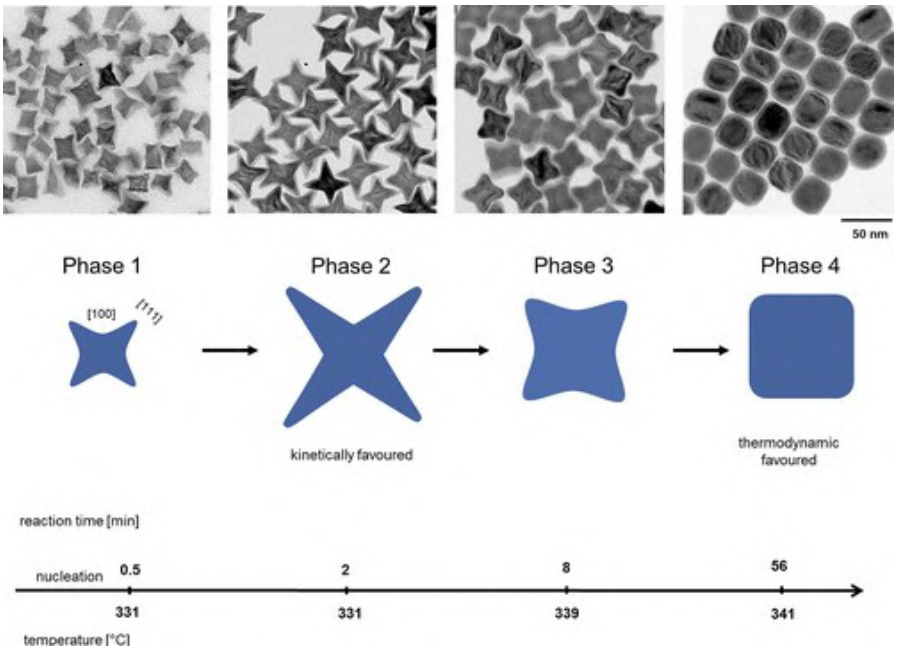

Figure 1.5: TEM images of Fe_3O_4 NPs size and shape formation during 1 h of reaction and a corresponding scheme of the different development stages. Figure adapted from Reference [62].

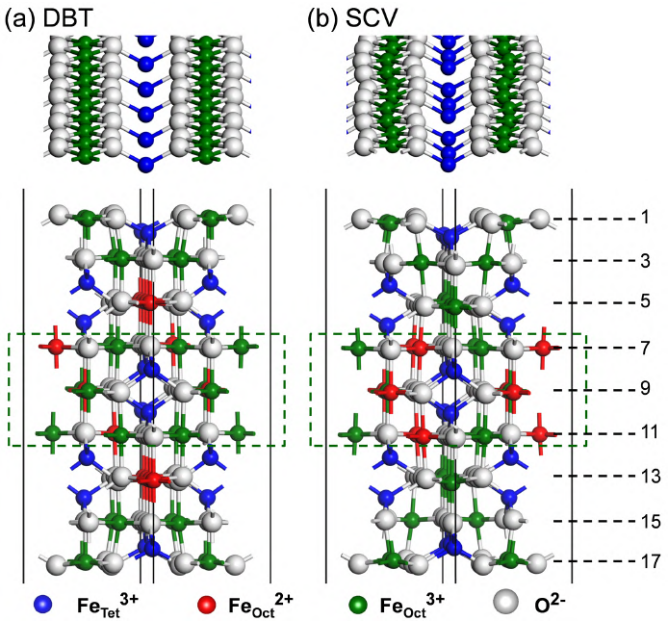

Figure 1.6: Top and side views of DBT and SCV $Fe_3O_4(001)$ surface models. Layers are numbered on the right and the color coding of the atoms is given in the legend on the bottom. Figure adapted from Reference [70].

in Figure 1.6a, thermodynamically more stable than the other configurations mentioned above [43, 76]. However, the Pendry reliability factor (R_P) for the LEED investigation was somewhat poor ($R_P = 0.34$) [77] and the DBT model could not explain the site preference of Au adatoms deposited on the Fe_3O_4 (001) surface [78]. In 2014, Bliem et al. [79] proposed a new reconstructed surface model called subsurface cation vacancy (SCV), shown in Figure 1.6b: a B layer-terminated Fe_3O_4(001) surface with an extra interstitial Fe_{Tet} in the second layer, replacing two Fe_{Oct} that are removed from the third layer, in each $(\sqrt{2} \times \sqrt{2})R45°$ unit cell. The SCV model shows a much better agreement with experimental LEED IV ($R_P = 0.125$ [79]) compared with the DBT model ($R_P = 0.34$ [77]) and agrees well with the surface X-ray diffraction (SXRD) [80]. In addition, the SCV model shows, at the DFT+U level of theory, a higher thermodynamic stability than DBT over the entire range of oxygen chemical potentials accessible under experimental conditions and can well explain the site preference of Au adatoms when deposited on the Fe_3O_4(001) surface [78, 79]. Recent SXRD, X-ray and ultraviolet photoelectron spectroscopy (XPS, UPS), low-energy electron diffraction and ion scattering (LEED, LEIS), infrared reflection absorption spectroscopy (IRRAS) and STM investigations found that under water exposure at elevated temperature, i.e., more than 700 K, the SCV surface is not anymore the most stable structure: at increasing water pressure the DBT surface becomes the most favored one [81–83]. The main features of the SCV reconstruction vanish irreversibly during the water exposure: tetrahedral interstitial sites in the second layer of the surface are fully depleted and the octahedral sites in the third layer get fully occupied. The lifting of the SCV reconstruction in the presence of water is consistent with the DFT-based surface phase diagram built at 900 K by Liu and Di Valentin [70]: at high water coverage, a stability inversion makes the hydrated DBT surface more stable than the SCV one. More recently, through a DFT+U study, Righi et al. [84] found that at room temperature the SCV is the most stable surface even under water-rich conditions. The lifting of the SCV reconstruction in favor of a bulk-like structure has been observed also after the exposure to formic acid [85].

The electronic properties of both SCV and DBT Fe_3O_4(001) surfaces were investigated through hybrid functional calculations by Liu and Di Valentin [70]. In agreement with experiments, outer layers contains only Fe^{III}, whereas a mixture of Fe^{II} and Fe^{III} is present in the inner layers. Being the SCV more oxidized than the DBT surface, i.e., the Fe:O ratio is lower in the former than in the latter, the amount of Fe^{II} is lower in the reconstructed structure than in the bulk-like one. In line with what found for the Fe_3O_4 bulk [33], both investigated models for the Fe_3O_4(001) surface show a semiconductor character, as shown in Figure 1.7, in agreement with previous DFT+U calculations performed on the DBT surfcace [46, 76, 78, 86].

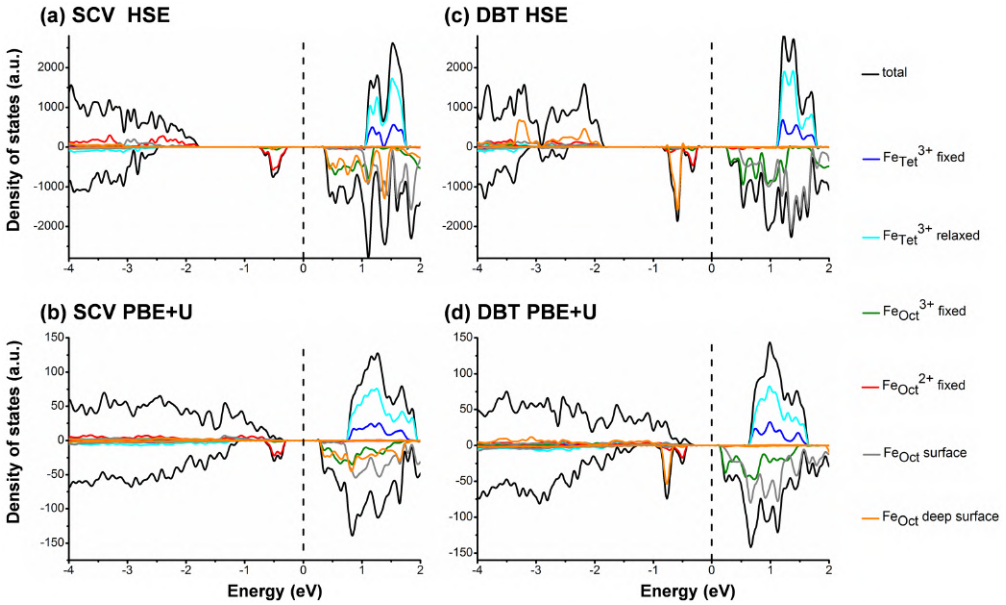

Figure 1.7: *Projected density of states* (PDOS) of DBT and SCV Fe_3O_4(001) surface models calculated at different levels of theory. The Fermi level is scaled to zero as indicated by the dashed black lines. The color coding is given in the legend on the right. Figure adapted from Reference [70].

1.1.3 Nanoparticles

Magnetite NPs with variable sizes have been successfully prepared with different shapes, including cubes, octahedra, rhombic dodecahedra, truncated octahedra, and spheres via various synthetic routes [17, 87–95]. However, cubic, octahedral, and truncated octahedral NPs enclosed by (001), (111), and a mixture of (111) and (001) facets, respectively, are the most commonly observed, being their shape compatible with the periodicity of the inverse spinel structure that characterizes Fe_3O_4 [87, 96]. Figure 1.8 shows Fe_3O_4 NPs of various shapes ranging from cubes enclosed in (001) planes to octahedra enclosed in (111) planes. The DFT+U-based calculation by Santos-Carballal et al. of the Wulff construction (see Figure 1.4) confirmed that a Fe_3O_4 nanostructure would be preferentially enclosed by (001) and (111) planes, with the former more stable than the latter plane [61]. In agreement with the theoretical calculation of the Wulff construction, Feld et al. found that the NPs growth in [111] directions is kinetically favored, whereas along [001] directions is thermodinamically favored [62], as schematized in Figure 1.5. Regarding the electronic properties, tunneling microscopy shows that below Verwey transition temperature Fe_3O_4 NPs are semiconductors with a small band gap from 0.14 to 0.30 eV [38, 41].

The resurgence of interest for Fe_3O_4-based nanosystems, especially with ap-

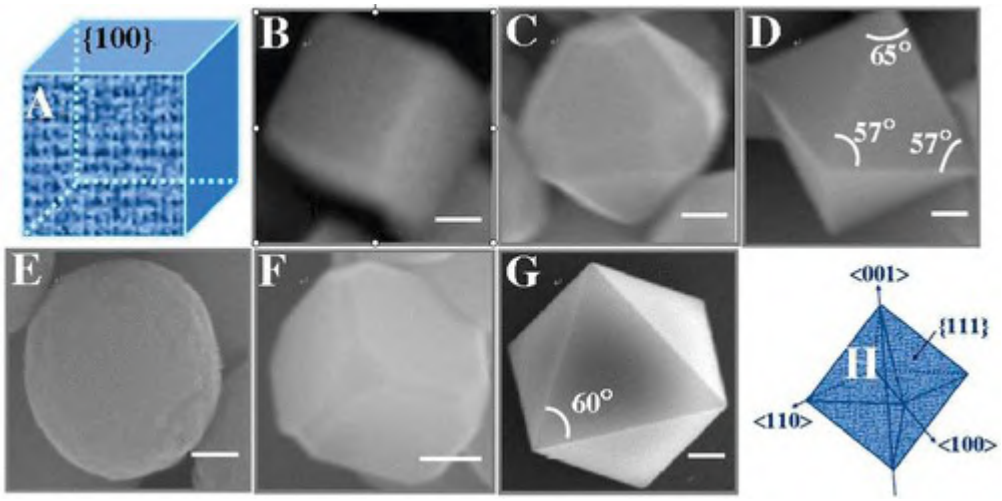

Figure 1.8: Fe_3O_4 NPs of various shapes ranging from cubes enclosed in (001) planes to octahedra enclosed in (111) planes, depending on the growth conditions. Figure adapted from Reference [87].

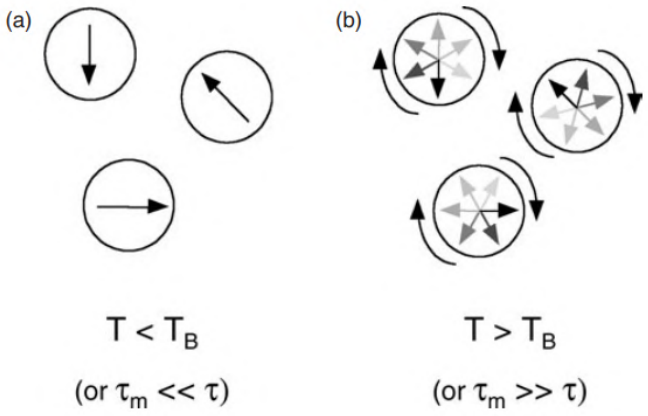

Figure 1.9: Illustration of the concept of superparamagnetism, where the circles depict NPs, and the arrows represent the net magnetization direction in those particles. In case (a), below T_B or for relaxation times τ much longer than the measurement time τ_m, the net moments are quasi-static and the overall magnetization is non-null. In case (b), above T_B, or for τ much shorter than τ_m, the moment reversals are so rapid that in zero external field the time-averaged overall magnetization is zero. Figure adapted from Reference [9].

plications in the fields of nanomedicine, is mainly due to the peculiar magnetic properties of such a material [9–16]. A single Fe_3O_4 NP is ferrimagnetic as well as bulk magnetite, as discussed in Section 1.1. However, a group of NPs is found to be superparamagnetic above the blocking temperature (T_B) and ferrimagnetic below it [9]. In other words, below T_B a group of NPs show a non-null overall magnetic moment; on the contrary, above such a temperature, the overall magnetic moment is almost zero. This is due to the fluctuations of the magnetic moments associated to each single NP, caused by the thermal energy, according to the equation

$$\tau = \tau_0 \exp\left(\frac{\Delta E}{k_B T}\right) \tag{1.1}$$

where τ is the magnetic moments relaxation time, ΔE the energy barrier to magnetic moment fluctuation, and $k_B T$ the thermal energy. Higher is the temperature, shorter is the relaxation time, i.e., faster is the fluctuation of the magnetic moments. As a consequence, if the time τ_m for measuring the overall magnetization of the NPs is longer than τ, a null overall magnetization is registered. This concept is schematized in Figure 1.9. The superparamagnetism appears only above T_B, once the overall magnetization of the NPs is null. In this regime, whose range also depends on the particles size (as schematized in Figure 1.10), measuring a non-null overall magnetization is possible only through the application of an external magnetic field. This phenomenon is not simply classified as paramagnetism because the saturation magnetization (i.e., the maximum magnetization value) of superparamagnetic systems is comparable to that of ferromagnetic systems, as shown by hysteresis curves in Figure 1.10, where H and M are the applied external magnetic field and the measured magnetization of the whole system. As already discussed, the magnetization M at zero external magnetic field H is null for superparamagnetic systems (SPM in Figure 1.10) and non-null for ferromagnets and ferrimagnets (FM in Figure 1.10), and the saturation magnetization shows similar values for such systems.

The high overall magnetic moment of Fe_3O_4 NPs is a key point for their applications in nanomedicine. Unfortunately, the saturation magnetization of magnetic NPs may be reduced by various factors. The main phenomena able to lower the magnetization of IONPs are (i) antiphase domain boundaries [97–99], (ii) spin canting (or disorder) [100–103], and (iii) variations in cristallinity. The first mechanism is due to structural defects, e.g., dislocations, which create inside a single NP different domains, whose magnetization vectors are not parallel [104, 105], as schematized in Figure 1.11. The second and the third mechanisms are related to finite dimensions and surface effects. Surface spin canting is understood as a consequence of broken exchange bonds and low symmetry near the particle surface, resulting in a non-ordered collection of spin magnetic moment [106], as schematized in Figure 1.12. Variations in cristallinity include surface reconstructions,

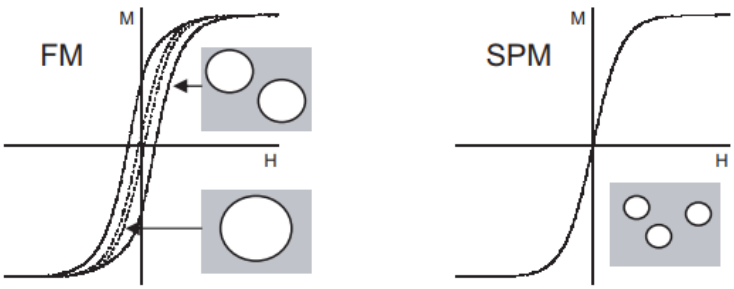

Figure 1.10: Schematic hysteresis (M - H) curve for ferromagnetic (FM) and superparamagnetic (SPM) materials. Figure adapted from Reference [9].

e.g., Fe ions occupying octahedral sites moving to tetrahedral ones, which imply the lowering of the overall magnetization according to the superexchange coupling described above [4, 5].

Very small IONPs (<25 nm), as those that are typically used in nanomedical applications, are usually magnetized homogeneously and stable single domain [107]. Only NPs with a diameter larger than 80 nm are sistematically multidomain nanostructures, affected extensively by antiphase domain boundaries [108–110]. On the contrary, NPs of every size are affected by surface reconstruction and spin disorder in a different extent depending on the synthesis route and preparation conditions [111–113]. Interestingly, surface functionalization with various anchoring groups is found to hamper spin and structural disorder: saturation magnetization values close to the bulk (96 emu/g) have been reported for coated magnetic NPs (∼80 vs. ∼40 emu/g for naked NPs) [114–120]. For example, Roca et al. [119] compared the NPs produced through two different synthetic routes: (i) by thermal decomposition of organic precursors in organic media and in the presence of oleic acid (which acts as surfactant), and (ii) by coprecipitation from iron salt solutions in aqueous media in the absence of ligands. NPs synthesized by thermal decomposition show higher saturation magnetization values at both low and room temperature (96 vs. 55 emu/g, and 84 vs. 46 emu/g, respectively). Donadel et al. [121] synthesized chitosan-coated Fe_3O_4 NPs through alkaline co-precipitation of ferric and ferrous chlorides in aqueous solution, with the low saturation magnetization value of 33 emu/g. Qu et al. [122] followed Donadel's procedure with a further addition of oleic acid in the mixture, obtaining a higher saturation magnetization value of 74 emu/g.

Being the capping molecules not magnetic, to understand the origin of the enhanced magnetization is not straightforward. In a combined experimental and theoretical work, Salafranca et al. [120] proposed an explanation comparing the electronic structure of bulk Fe_3O_4, bare $Fe_3O_4(001)$ surface and capped $Fe_3O_4(001)$

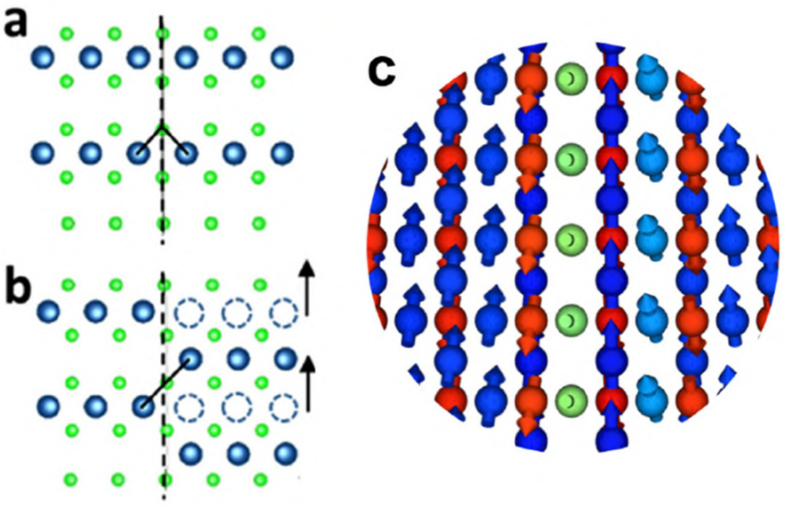

Figure 1.11: (a) Top view of a bulk magnetite (001) B layer that contains O (green beads) and Fe_{Oct} (blue beads). (b) Top view of a (001) B layer presenting an antiphase domain boundary with the shift vector along [-110] direction (indicated by the black arrows). The $Fe_{Oct}-O-Fe_{Oct}$ angle changes from 90° in (a) to 180° in (b). (c) Iron ions magnetic moments close to the magnetic domain wall formed as a consequence of the presence of an antiphase domain boundary. The net magnetizations of the left and right side of the magnetic domain wall are not parallel. Figure adapted from Reference [105].

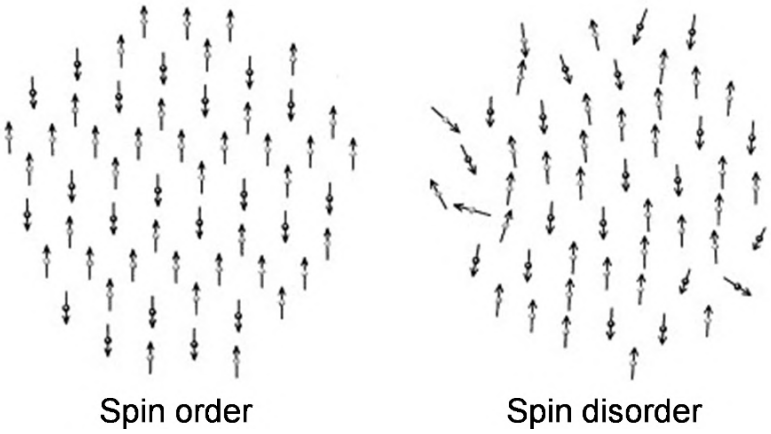

Figure 1.12: Schematic representation of spin magnetic moments in case of surface spin order (on the left) and spin disorder (on the right). Figure adapted from Reference [102].

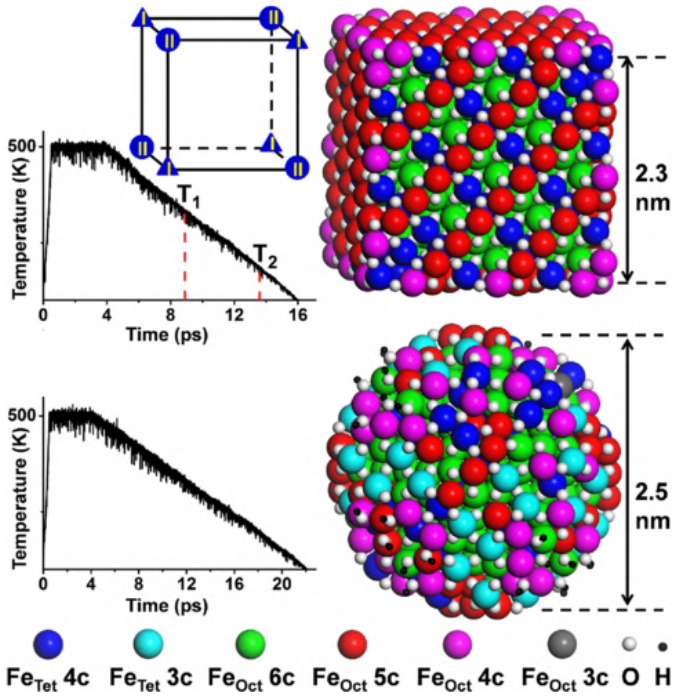

Figure 1.13: Simulated annealing temperature profiles and global minimum structures of the magnetite cubic (up) and spherical (down) NP. The color coding of atoms is given in the legend at the bottom. Labels 3c–6c indicate the actual coordination number of the corresponding ions. Figure adapted from Reference [125].

surface with organic acids. The authors explained the reduced magnetization at magnetite bare surface with its metallic behavior. The magnetization is then restored for the capped surface along with its semiconductor behavior. However, these results are not consistent with the existing literature. Indeed, several DFT+U and hybrid functionals calculations show a gap at Fermi level for the bare $Fe_3O_4(001)$ surface [46, 70, 76, 86, 123, 124] in analogy with what observed for bulk Fe_3O_4 [33, 45, 53] and in contrast with the metallic character observed by Salafranca and collaborators [120]. An improved crystallinity, a reduced surface anisotropy, and a restored bulk coordination around the surface Fe are often and vaguely invoked as possible causes, but the underlying mechanism for the enhanced saturation magnetization is still not clear.

Despite the relevance of Fe_3O_4 NPs in nanobiotechnology, it is possible to observe a severe lack of a theoretical framework, which could assist in the interpretation and comprehension of experimental findings at an atomic scale and guide further experiments. Unfortunately, magnetite is a complex material to be described accurately by theoretical methods. Up to now, Fe_3O_4 nanoparticles have mainly been addressed by force-field methods to study their interaction with sur-

factants and capping agents [126–133]. However, these types of simulations have some intrinsic limitations, since they cannot provide any information on the electronic and magnetic structure, cannot handle bond breaking and bond formation, and have limited transferability. As already discussed, Liu and Di Valentin [33, 70] showed that, to catch proper structural, electronic, and magnetic properties of even the most simple bulk and flat surface systems, high-level quantum mechanical techniques, beyond standard DFT, are required. Within the same theoretical framework and protocol, they gave a first insight into the quantum mechanical modelling of Fe_3O_4 NPs of quasi-realistic dimensions. In 2019, Liu and Di Valentin [125] investigated through hybrid functional calculations the structural, electronic, and magnetic properties of cubic and spherical Fe_3O_4 NPs (shown in Figure 1.13), all of them constituted by more than 1000 atoms. They caught and discussed the Fe^{II}/Fe^{III} disproportion, as well as the semiconducting behavior of the two models of Fe_3O_4 NP under investigation. Furthermore, they identified a surface reconstruction mechanism which lowers the overall magnetization of a cubic Fe_3O_4 NP, and provided a general empirical formula for the *a priori* evaluation of the overall magnetic moment of such Fe_3O_4 nanostructures.

1.2 Magnetite applications in emerging fields

1.2.1 Nanomedicine

Fe_3O_4 NPs are top-class materials for biomedical and nanomedicine applications because of their excellent soft magnetism [17] (high saturation magnetization and low coercive force, i.e., superparamagnetism), good biocompatibility and low citotixicity [134, 135], and availability to surface modification [136], as already mentioned at the beginning of this chapter. The room temperature superparamagnetism of IONPs allows the control of fluids containing nanostructures of such materials through the application of an external magnetic field [137], as schematized in Figure 1.14. This behavior opens up the way for a variety of both *in vivo* and *in vitro* applications in the emerging field of nanomedicine.

Up to now, several methods, such as co-precipitation [118, 138–140], solvothermal/hydrothermal synthesis [17, 141, 142], sol–gel reactions [143], micro-emulsion templated synthesis [114, 144], and thermal decomposition [88–90, 92, 93, 115–117, 119, 120], have been developed to synthesize IONPs. Among these methods, the thermal decomposition of organic precursors in organic media in the presence of surfactants is often preferred since it is capable of controlling the particle size, shape, crystallinity, and magnetism [88–90, 92, 93, 115–117, 119, 120]. The as-prepared NPs are usually coated with small hydrophobic molecules, e.g., oleic acid and oleylamine, which make them only soluble in non-polar solvents. Since most

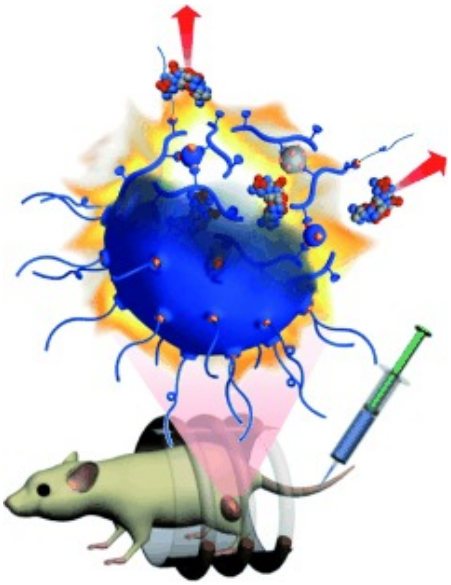

Figure 1.14: Schematic representation of a magnetic NP that can be controlled through an external magnetic field for in vivo applications, such as targeted drug delivery. Figure adapted from Reference [137].

applications of IONPs require high stability in aqueous environment, it is of great importance to perform surface modification with hydrophilic and biocompatible coatings, e.g. silica, gold, molecular surfactants, and polimers, to avoid agglomeration [10, 11, 14–16, 136, 145]. In general, two strategies, *grafting from* and *grafting to*, are employed to bind polymer chains onto IONPs [16]. The *grafting from* method involves surface initiation and subsequent polymerization on the NP surface, while in the *grafting to* system, end-functionalized polymers are connected to the NPs by the ligand exchange route. Moreover, the protecting shell should be accessible for further functionalization to optimize the system for specific applications [10, 14–16, 136], as schematized in Figure 1.15.

Nuclear magnetic resonance (NMR) is a powerful magnetic phenomenon mainly used in clinics for imaging. In contrast to surface-based sensors, NMR is capable of sampling an entire volume in a non-invasive way. Magnetic resonance imaging (MRI) can be combined with other diagnostic tools, like X-ray CT (computed tomography), PET (positron emission tomography) or US (ultrasound), to obtain more accurate diagnosis, for which multimodal superparamagnetic IONPs can be afforded either combining several agents into a single carrier or by engineering a material that can be active in several modalities [146]. It is a known fact that the magnetic core creates a local magnetic inhomogeneity, which alters the relaxation time of hydrogen protons in the surrounding water molecules [147]. This fact has motivated different studies based on the use of magnetic IONPs as versatile dual

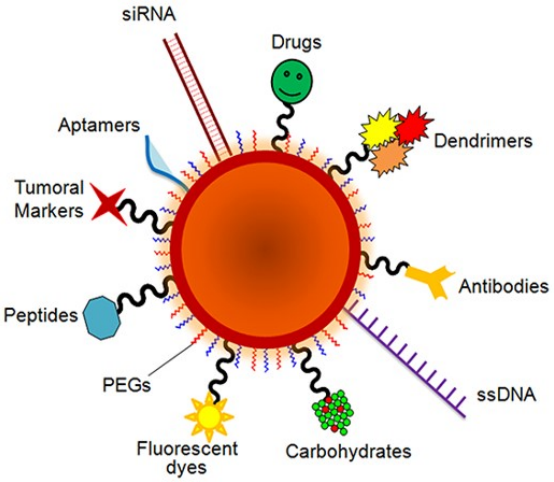

Figure 1.15: Schematic representation of a functionalized NP for various applications.

MRI contrast agents for T_1 and T_2 relaxation, in order to avoid the conventionally used gadolinium chelates [148] and their potential toxicity [149]. Gadolinium, a paramagnetic ion with the largest number of unpaired electrons, is the most effective T1 contrast agent, which has however the main drawback of being toxic, although it is always used in combination with chelating molecules with the aim of avoiding its potential risk [149].

Targeted drug delivery refers to predominant drug accumulation within a target zone that is independent of the method and route of drug administration. Effective targeted drug delivery systems have four key requirements: retain, evade, target, and release. This entails efficient drug loading into a type of delivery vehicle, sufficient residence in the circulation to reach the intended sites of the body, retention by specific characteristics within intended sites (i.e., targeting), and drug release at the intended site within a time that allows for the effective function of the drug [150, 151]. The basic purpose of magnetic IONPs-based targeted drug delivery is to physically direct a loaded magnetic drug carrier system to a specific organ or tissue with an externally applied magnetic field for drug accumulation. Compared with conventional drug administration, magnetic IONPs-based targeted drug delivery could reduce drug concentration in the body compartments overall, thus reducing systemic side effects. In addition, the concentration in the affected tissue is effectively increased, resulting in an enhanced therapeutic effect [152]. Surface engineering typically protects against iron oxide core agglomeration, and also provides chemical handles for the conjugation of drug molecules, targeting ligands, and reporter moieties, and limits non-specific cell interactions [10, 14–16, 136].

Cancer hyperthermal treatment using IONPs is of particular interest because they have much less side effects compared to traditional chemotherapy and radio-

therapy [153, 154]. Magnetic hyperthermia of IONPs is caused via dipole relaxation induced by an alternating magnetic field [155–158]. The heat generated by the locally injected IONPs can specifically destroy tumor cells, but show minimal damage to healthy tissues. The local temperature can also be easily controlled by the alternating magnetic field power and the concentration of IONPs in the tumor. Polymergrafted IONPs can serve as a hyperthermia agent due to the combination of magnetic heating of IONPs and the stability of polymers. Besides, the polymer brushes on the surface can help controlling the state of dispersion as well as the interparticle distance. More importantly, thermal-responsive polymers can also be integrated on IONPs to achieve heat-triggered drug release.

Aside the above-mentioned *in vivo* applications, IONPs have been attracting interest also for *in vitro* applications, such as bioseparation and biosensing. The ability to selectively trap and separate target molecules in biological samples is a critical component of biomedical applications. Target and probe molecules are typically mixed and then separated in batch processes that require multiple pipetting, tube washing, and extraction steps, which can affect accuracy. Therefore, the development of cost-effective separation techniques is a crucial factor in industrial biotechnology production and in routine procedures in molecular biology. Among the numerous methods used for bioseparation, IONPs-based separation techniques are becoming increasingly critical, with a wide range of potential applications in bioscience research. This is because IONPs can be separated easily and quickly by an external magnetic field (specifically, providing cost reduction and process integration), which can be used in combination with appropriate ligands and selectively separated biomaterials such as cells, proteins, genes, and pathogens extracted from a specimen for detection and characterization [159, 160]. Furthermore, IONPs have recently drawn considerable interest as immobilizing matrices for biosensor development. IONPs-based biosensors are usually produced using two main sensing mechanisms: electrochemical sensing and immunosensing. Electrochemical sensing methods are developed rapidly because such devices fulfill many demands for analytical detection and exhibit numerous advantages such as sensitivity, selectivity, rapid response, and low cost [161]. Immunosensing involves affinity ligand-based biosensing solid-state devices in which the immunochemical reaction is coupled to a transducer. The purpose of all immunosensors concerns the specificity of the molecular recognition of antigens by antibodies to form a stable complex [162].

1.2.2 Disposal of radioactive waste

The discovery of element 43, Tc, was officially confirmed by Carlo Perrier and Emilio Segrè in 1937 [163] in Italy. Technetium may form naturally, but the overwhelming majority is from anthropogenic sources. In nature, Tc can be produced

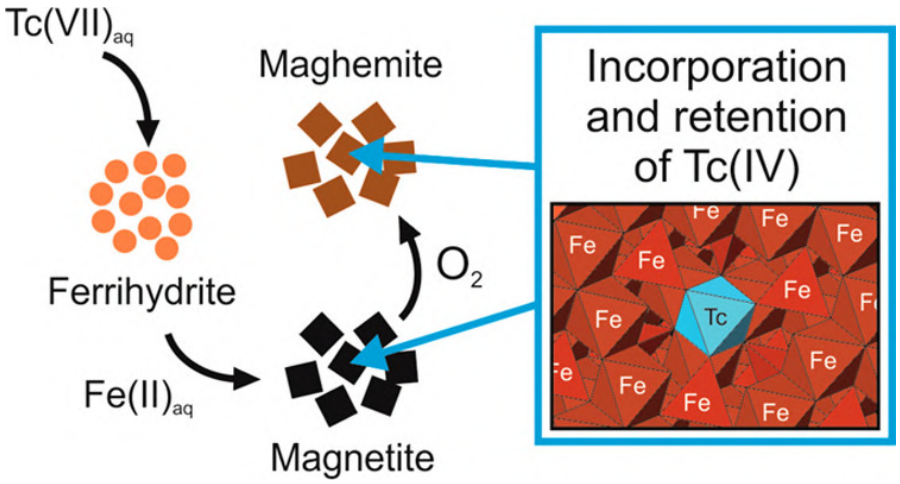

Figure 1.16: Schematic representation of the reduction and retention of Tc(VII) by Fe(II)-containing liquid and solid phases. Figure adapted from [20].

through the spontaneous fission of ^{238}U, neutron-induced fission of ^{235}U or cosmic ray reactions with Mo, Ru and Nb within the earth's crust [164, 165]. Anthropogenic sources are mainly from nuclear power plants activity [164, 165], and to a lesser extent from global weapons [166, 167] and medical applications [168]. Tc has been released to our environment intentionally or accidentally or through regulated discharges. Most of Tc isotopes like ^{97}Tc and ^{98}Tc are unstable in the environment, whereas ^{99}Tc, which is a weak β-emitting nuclear fission product, has a long half-life ($t_{1/2} \sim 2.1 \times 10^5$ year) [163–165]. Once Tc is released in the environment in the absence of any complexing ligand other than water, Tc^{VII} and Tc^{IV} are the prevailing redox states under non reducing and reducing conditions, respectively [169]. In oxidising environments, Tc^{VII} is found over the entire pH range as the highly mobile TcO_4^- anion, which shows very high solubility and weak adsorption properties [170]. People can be exposed to Tc through the consumption and ingestion of water and food contaminated by the highly soluble and mobile TcO_4^- anion. Beyond a certain threshold, Tc could concentrate in the thyroid gland and gastrointestinal tract, potentially causing cancer and other adverse health effects [171]. Under reducing conditions, Tc^{IV} forms sparingly soluble hydrous oxides [172], which could strongly adsorb to mineral surfaces [173].

As for other redox-sensitive radionuclides, Fe^{II} solid phases play a relevant role in the geochemistry of Tc, often involving a combination of reduction and uptake processes, as schematized in Figure 1.16. The anoxic corrosion of metallic iron/steel canisters, commonly used as deep underground repositories for the radioactive waste disposal [174], produces minerals containing Fe^{II} [175, 176]. Under the alkaline conditions of geological repositories, Fe_3O_4 is expected to be one of the

most abundant product of the canisters corrosion [175]. The role of Fe-containing minerals in the reduction and immobilization of Tc^{VII} has been intensively investigated over the last decades. Cui and Eriksen [177, 178] studied the reduction of Tc^{VII} by Fe^{II} and the uptake of Tc by Fe^{II}-containing phases in the presence of synthetic ground water. According to the authors' conclusions, the Tc uptake was found to be controlled by a exchange mechanism of ligands adsorbed onto the mineral surface. Burke and collaborators [179–183] conduced several studies dedicated to the interaction of Tc^{VII} with Fe-containing sediments. All these studies reported the formation and precipitation of $TcO_2{\cdot}xH_2O$(s) as the main mechanism for the reduction and immobilization of Tc. Kobayashi et al. [19] in 2013 investigated the reduction/adsorption of Tc^{VII} in the presence of Fe^{II} (magnetite, mackinawite, and siderite) and Fe^{III} (goethite and hematite) minerals. The reduction of Tc^{VII} and consequent decrease of aqueous Tc concentration were only observed in the presence of the Fe^{II}-containing minerals. The authors reported the complete incorporation of Tc^{IV} into the magnetite structure. Similar results regarding the Tc^{IV} immobilization were found by Marshall et al. in 2014 [20]. The Tc^{IV} incorporation in Fe_3O_4 was studied also through quantum mechanical calculations, in particular with the Unrestricted Hartree-Fock (UHF) method [184]. More recently, Yalçintaş et al. [185] conduced a X-ray adsorption spectroscopy (XANES and EXAFS) study considering various models for both incorporation and surface adsorption of Tc^{IV} by Fe_3O_4. Despite the huge number of studies on the reduction and uptake of Tc by Fe_3O_4, the mechanism of the reduction, as well as the final products of the immobilization, is still unclear.

1.2.3 Electrocatalysis of the oxygen evolution reaction

Electrochemical water splitting is an emerging technology for the production of sustainable hydrogen, as a mean to store energy from excess renewable energy sources in the form of a high-energy-density fuel [186, 187]. The process is composed of two half-reactions: the cathodic hydrogen evolution reaction (HER) and the anodic oxygen evolution reaction (OER). One of the key factors limiting the efficiency of the overall process is the sizeable energy loss caused by the high overpotentials of the OER, which is usually considered to be the bottleneck of the electrochemical production of hydrogen [188]. Among the various materials employed as electrocatalysts, only noble metals, such as Ru, Pt, or Ir, show promising OER activity and stability in acidic media. On the contrary, in alkaline solution many inexpensive and abundant metals (e.g., Fe, Co, and Ni) and their alloys (e.g., oxides) show comparable or even better catalytic performance than noble metals [189]. Nonetheless, alkaline water electrolysis has long been considered inefficient compared to acidic electrolysis, because of the worse performance of the hydroxide conducting polymer electrolyte membranes (PEM) compared to the proton

conducting ones. However, recent studies suggest that alkaline cells could present similar or even higher activity than acidic systems by optimizing the hydroxide conducting PEMs typically used in current systems [190, 191]. The search for the best OER catalyst in alkaline media is ongoing, and transition metal oxides containing Ni, Co and Fe have been proposed as suitable candidates.

Fe_3O_4 showed good stability and fair activity for the OER. Mullner et al. [24] did not observe any changes in the reconstructed $Fe_3O_4(001)$ surface under OER conditions, with a fair overpotential value of 0.48 V. Grumelli et al. [25] confirmed the stability of the SCV surface in an electrochemical environment for the OER with an overpotential of 0.44 V. They also measured the overportential for the unreconstructed DBT surface with the value of 0.49 V. Righi et al. [84] investigated the stability and the electrochemical performance toward OER for various model of $Fe_3O_4(001)$ surface by means of DFT+U calculations. Furthermore, the reconstructed $Fe_3O_4(001)$ surface was found to easily adsorb adatoms transition metal atoms [78, 79] leading to the formation of so-called single atom catalysts (SACs).

The noun "single-atom catalyst" was coined and used for the first time by Tao Zhang and collaborators [192] for indicating the extreme downsizing of metal particles involved in heterogeneous catalysis. Usually, catalysts are constituted by metal particles finely dispersed on a high-surface-area support, and only a small portion is actually involved as active center in the catalytic process. The metal particles usually show a broad size distribution and irregular morphology, and may possess multiple active sites with different performances. Such heterogeneity affects the efficient use of metal and reduces the selectivity toward a specific product. The size reduction of the metal clusters, from bulk- to nano- and subnano- dimensions, improves the efficiency of metal use and the selectivity of a specific reaction [193–195]. However, reducing the metal clusters size has a drawback: the surface free energy of metals increases significantly, as shown in Figure 1.17. One possibility to overcome this problem is the use of an appropriate supporting material that strongly interacts with the metal species [196]. Despite their small size, subnanoclusters still contain multiple active centers and some of them are not always the most desirable for a certain catalytic process. The most effective way to use each single metal atom and produce catalysts with well-defined unique active centers is to further downsize the metal nano- and subnano-particles to well-defined, atomically distributed metal active centers [192, 197, 198]. In 2011, Tao Zhang's research group [192] for the first time prepared a Pt SAC supported on iron oxides, named Pt_1/FeO_x, with excellent performances toward CO oxidation. From that moment, several SACs have been prepared with various metal atoms and supporting materials, such as transition metal oxides [199–201], monolayer two-dimensional (2D) materials [202, 203], metal organic frameworks (MOFs) [204], and so on.

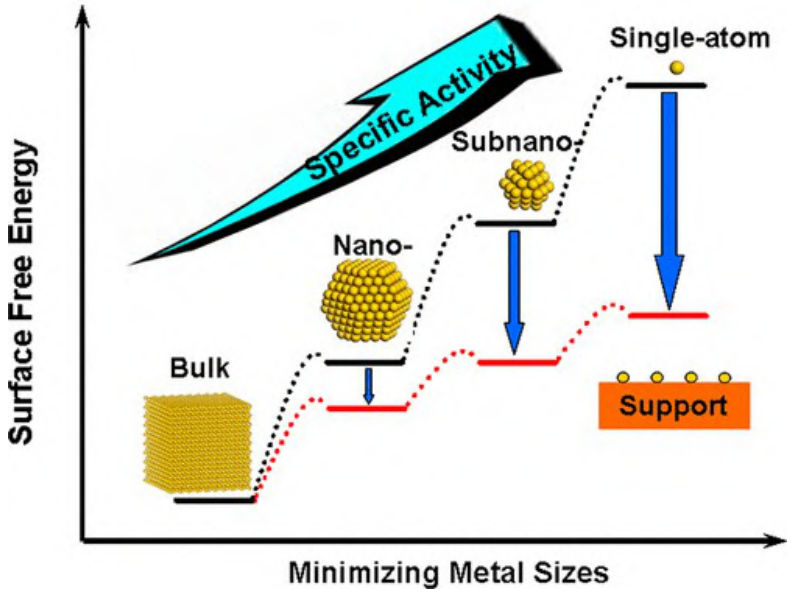

Figure 1.17: Surface free energy (and specific activity) as a function of the metal particle size. The stabilizing effect obtained by supporting the metal is displayed by the red profile. Figure adapted from Reference [196].

As just mentioned, but also discussed in previous paragraphs and sections, also Fe_3O_4 can be used as a support material for the preparation of SACs [23]. The $Fe_3O_4(001)$ SCV reconstruction essentially creates an array of strongly binding defect sites (periodicity 0.84 nm), on which metal adatoms of almost any variety bind with a two-fold coordination to lattice oxygen atoms [23, 58, 79]. Transition metals are found to be extremely stable against thermal sintering on Fe_3O_4, but some of them, such as Ti [205], Mn [205], Co [205, 206], Ni [205, 207], Zr [205], Rh [208], and Ir [209] at a certain temperature tend to diffuse and incorporate into the surface layer. On the contrary, other metals, such as Cu [210], Ag [210, 211], Au [78, 79], and Pt [212, 213] do not incorporate in the spinel lattice, and remain stable as adatoms until the reconstruction is thermally lifted up to 700 K. Mixed first row transition metal-Fe oxides being some of the most promising materials for OER electrocatalysts [214–219], it is reasonable to think that transition metals SACs may improve the catalytic performance of magnetite toward the OER. No systematic investigations have yet been conduced to elucidate the OER steps and performance of $Fe_3O_4(001)$-based SACs, except the experimental study of Ni-modified $Fe_3O_4(001)$ by Mirabella et al. [26]. In this work, the authors found that the presence of Ni adatoms is not enough to guarantee the decrease of the overpotential with respect that of the pure magnetite, but a higher Ni concentration that implies the formation of a mixed Ni-Fe oxide phase is required [26].

1.3 Outline of the thesis

The aim of the research work reported in this PhD thesis is the first-principles investigation of structural, electronic, and magnetic properties of magnetite (Fe_3O_4) nanostructures and their interaction with various chemical species for relevant technological applications. In particular, on one hand, we have considered a cubic Fe_3O_4 nanoparticle (NP) enclosed by six (001) facets to investigate the effects of surface functionalization for nanomedical applications. On the other hand, we have considered a $Fe_3O_4(001)$ surface model to study the interaction and immobilization of technetium, which is a nuclear fission product with high radiotoxicity and long half-life. Similarly, we used the $Fe_3O_4(001)$ surface also as a support material for single atom catalysts (SACs) of various transition metal elements for the oxygen evolution reaction (OER).

For this work, state-of-the-art computational methods and massively parallelized codes are employed in order to perform highly accurate calculations of such large systems in a reasonable time. Most of the calculations were based on density functional theory (DFT), using hybrid functionals (HSE06) and localized basis sets, which is a well-suited approach for the description of magnetite in terms of structural, electronic, and magnetic properties. An approximated DFT-based method, namely the Hubbard-corrected self-consistent charge density-functional tight-binding (SCC-DFTB+U, from now on DFTB+U), has been considered for the structural properties and dynamical behavior of the largest systems. An overview of the theoretical methodologies employed in this PhD thesis is provided in Chapter 2.

Chapter 3 is focused onto the structural, electronic, and magnetic properties of naked and functionalized cubic Fe_3O_4 NPs enclosed by six (001) facets. In experiments, surface functionalization of magnetite nanoparticles is found to prevent the reduction of the overall magnetic moment with respect to bulk, but the underlying mechanism is still to be clarified. Therefore, we explored the effects of the adsorption of various ligands (containing hydroxyl, carboxylic, phosphonic, catechol, and silanetriol groups), commonly used to anchor surfactants during synthesis or other species during chemical reactions, onto the spin and structural disorder, which are phenomena contributing to the lowering of the NP magnetization. Understanding the nature and behavior of such phenomena may guide the design and optimization of Fe_3O_4 nanosystems for a broad range of technological applications.

Chapter 4 is focused onto the interaction between the $Fe_3O_4(001)$ surface and the pertechnetate ion ($Tc^{VII}O_4^-$). Experimentally, it is clear that Fe_3O_4 can reduce $Tc^{VII}O_4^-$ to Tc^{IV} species and retain such products quickly and completely, but the exact nature of the process and redox products is not completely defined. Therefore, we studied a possible initiation step of the $Tc^{VII}O_4^-$ reduction to Tc^{IV} and explored various model structures for the immobilized products of the Tc^{VII}

reduction: Tc^{IV} incorporation and adsorption in the form of $Tc^{IV}O_2{\cdot}xH_2O$ chains.

Chapter 5 is focused on the use of the $Fe_3O_4(001)$ surface as support material for SACs for the oxygen evolution reaction (OER), which is usually considered to be the bottleneck of the electrochemical production of hydrogen. Inexpensive and abundant metals, such as Ti, Co, Ni, and Cu, are trapped in various configuration in the $Fe_3O_4(001)$ surface. Once the most stable structure for each metal was determined, we investigated the models as electrocatalysts in alkaline conditions towards the OER, by means of the computational hydrogen electrode (CHE) model [220]. Our results could give some hints in the search and design of a good OER catalyst in alkaline media.

Chapter 6 is focused on the development of a set of force field (FF) parameters for the description of iron oxides/water interphase. An existing set of CLASS2 FF parameters is optimized to describe the Fe–O_{water} cross-interaction through comparison, based on HSE06 calculations, of the potential energy function for a single water molecule adsorbed on the $Fe_3O_4(001)$ surface and with density functional tight binding DFTB+U molecular dynamics simulations for a water trilayer on the same surface. Their transferability is tested for water adsorption on the curved surface of a spherical Fe_3O_4 NP.

Chapter 2

Theoretical Background

In this chapter, a brief overview of some fundamental aspects of computational materials science is given. The density functional theory is presented with its main approximations and methods. The density functional tight-binding, i.e., an approximated method based on the density functional theory, is also introduced. The Bloch's theorem is discussed with its implications to the computational materials science. Finally, some of the most popular geometry optimization algorithms are briefly introduced. This chapter is based on the review article by Koskinen and Mäkinen [221] and the textbooks by Ashcroft and Mermin [222], Grosso and Parravicini [223], Pisani [224], and Jensen [225].

2.1 Density functional theory

In the past, methods devoted to the solution of the many-electron problem and consequent calculation of the electronic structure were based on the search for the best approximation of the exact ground-state many-electron wave function $\Psi_G = \Psi_G(\mathbf{r}_1\sigma_1, ..., \mathbf{r}_N\sigma_N)$, which depends on the spatial (and spin) coordinates of each electron belonging to the whole system. In the density functional theory (DFT) the focus shifts from the ground-state many-electron wave function to the much more manageable ground-state one-body electron density $n(\mathbf{r})$, which depends on the spatial coordinates of the point under exam only. The DFT shows that the ground-state energy of a many-particle system can be expressed as a functional of the one-body density. The minimization of such functional allows in principle the determination of the actual ground-state density and, consequently, ground-state properties. The strength of the DFT stands on the possibility to provide reasonably simple (but at the same time accurate) approximations of the functional to be minimized. The peculiarity of the density functional approach to the many-body problem is to compute a one-electron Schrödinger equation with a local

effective potential for the characterization of the ground-state electronic density of the many-electron systems.

2.1.1 The Hohenberg-Kohn theorem

Consider a system with N electrons, described by the many-electron Hamiltonian operator H. For convenience, H is decomposed into the sum of an "internal" part (kinetic energy of the electrons plus electron-electron Coulomb interactions) and "external" part (the electronic-nuclear interactions, in our specific case):

$$H = H_{int} + V_{ext}$$

$$H_{int} = T + V_{ee} = \sum_i \frac{p_i^2}{2m} + \frac{1}{2}\sum_{i \neq j} \frac{e^2}{|\mathbf{r}_i - \mathbf{r}_j|} \tag{2.1}$$

$$V_{ext} = \sum_i v_{ext}(\mathbf{r}_i) \text{ with } v_{ext}(\mathbf{r}_i) = -\sum_I \frac{z_I e^2}{|\mathbf{r} - \mathbf{R}_I|} \equiv V_{nucl}(\mathbf{r}).$$

For simplicity, we suppose that the ground-state $|\Psi_G\rangle$ is non-degenerate. The external potential $v_{ext}(\mathbf{r})$ is considered as the only variable of the many-electron problem, whereas the mass of the electrons, their charge, their number N, and the form of the internal interactions are supposed to be fixed. The Hohenberg-Kohn theorem states that *there is a one-to-one correspondence between the ground-state density of a N-electron system and the external potential acting on it.* In this sense, the ground-state electron density becomes the variable of interest.

Suppose to know $v_{ext}(\mathbf{r})$ and consequently the total Hamiltonian H of the system. In principle, by solving the Schrödinger equation it is possible to know the eigenfunctions and eigenvalues of the electronic system and in particular the actual ground-state wave function $\Psi_G(\mathbf{r}_1, \mathbf{r}_2, ..., \mathbf{r}_N)$, which does not include the spin component for simplicity. In other words, the ground state wave function $|\Psi_G\rangle$ depends on the external potential $v_{ext}(\mathbf{r})$; this can be indicated through the functional notation $\Psi_G = \Psi_G[v_{ext}(\mathbf{r})]$. From the knowledge of $|\Psi_G\rangle$, it is possible to compute the ground-state one-body density $n(\mathbf{r})$ defined as:

$$n(\mathbf{r}) = \langle \Psi_G(\mathbf{r}_1, \mathbf{r}_2), ..., \mathbf{r}_N | \sum_i \delta(\mathbf{r}_i - \mathbf{r}) \, | \Psi_G(\mathbf{r}_1, \mathbf{r}_2), ..., \mathbf{r}_N \rangle \, . \tag{2.2}$$

By multiplying both members of the Equation (2.2) by $v_{ext}(\mathbf{r})$ and integrating over the space variable, we obtain:

$$\langle \Psi_G | \, V_{ext} \, | \Psi_G \rangle = \int n(\mathbf{r}) v_{ext}(\mathbf{r}) d\mathbf{r}. \tag{2.3}$$

The present reasoning can be summarized with the scheme:

$$v_{ext}(\mathbf{r}) \longrightarrow \Psi[v_{ext}] \longrightarrow n(\mathbf{r})$$

which means that the knowledge of $v_{ext}(\mathbf{r})$ entails the knowledge of $\Psi_G[v_{ext}(\mathbf{r})]$ and consequently the knowledge of $n(\mathbf{r})$. In other words, there is a functional that relates $n(\mathbf{r})$ and $v_{ext}(\mathbf{r})$:

$$n(\mathbf{r}) = F[v_{ext}(\mathbf{r})]. \tag{2.4}$$

The novelty of the Hohenberg-Kohn theorem relies on the one-to-one correspondence between $n(\mathbf{r})$ and $v_{ext}(\mathbf{r})$, which allows to invert the relation expressed in Equation (2.4):

$$v_{ext}(\mathbf{r}) = G[n(\mathbf{r})] \tag{2.5}$$

which means that from the knowledge of the density $n(\mathbf{r})$ we can determine uniquely the external potential $v_{ext}(\mathbf{r})$ and thus the Hamiltonian H of the system and, in principle, any other property of the system.

To further elaborate the consequences of the Hohenberg-Kohn theorem, it is convenient to define other functional relations. In the following obvious functionals of the $v_{ext}(\mathbf{r})$ are schematized:

$$v_{ext}(\mathbf{r}) \longrightarrow \Psi_G[v_{ext}] \begin{cases} \longrightarrow E[v_{ext}] \\ \longrightarrow T[v_{ext}] \\ \longrightarrow V_{ee}[v_{ext}]. \end{cases} \tag{2.6}$$

These relations state that the expectation value of the total electronic energy, electron kinetic energy and electron-electron interaction on the ground-state wave function are functionals of the external potential $v_{ext}(\mathbf{r})$. Being $n(\mathbf{r})$ and $v_{ext}(\mathbf{r})$ in one-to-one correspondence, according to the Hohenberg-Kohn theorem, it is possible to rewrite the expectation values above as: $E[n(\mathbf{r})]$, $T[n(\mathbf{r})]$, and $V_{ee}[n(\mathbf{r})]$.

As a consequence of the Hohenberg-Kohn theorem, the formulation of a variational principle concerning the ground-state density of a system is possible. Considering a system of interacting electrons and fixing the external potential $v_{ext}(\mathbf{r})$, while varying the electron density $n(\mathbf{r})$, we can construct the functional:

$$E^{(HK)}[n(\mathbf{r}); v_{ext}(\mathbf{r})] \equiv \langle \Psi_G | \, T + V_{ee} + V_{ext} \, | \Psi_G \rangle \, . \tag{2.7}$$

Through the Hohenberg-Kohn theorem we can rewrite the Equation (2.7):

$$E^{(HK)}[n(\mathbf{r}); v_{ext}(\mathbf{r})] = T[n(\mathbf{r})] + V_{ext}[n(\mathbf{r})] + \int v_{ext}(\mathbf{r}) n(\mathbf{r}) d\mathbf{r}. \tag{2.8}$$

The energy functional $E^{(HK)}[n(\mathbf{r}); v_{ext}(\mathbf{r})]$, which exists and is unique, is minimal when $n(\mathbf{r})$ is the exact ground-state density, and its minimum gives the exact

ground-state energy of the many-body electron system. It is also worth to notice that the functionals $T[n]$ and $V_{ee}[n]$ are universal, i.e. they do not depend on vext. Anyway, these functionals, as well as those depending on $v_{ext}(\mathbf{r})$, are not known explicitly, and must be appropriately approximated.

2.1.2 The Kohn-Sham equations

The Kohn-Sham equations are obtained by minimizing the functional expressed in Equation 2.8 with respect to $n(\mathbf{r})$. In the framework of the DFT, the Kohn-Sham method relies on the assumption (valid at least for non-patological situations) that, for each non-uniform ground-state density $n(\mathbf{r})$ of an interacting electron system there exist a non-interacting electron system with the same non-uniform ground-state density. As a consequence, within the Kohn-Sham assumption the ground-state density $n(\mathbf{r})$ of any interacting electron system with N electrons can be decomposed exactly into the sum of N independent orbital contributions:

$$n(\mathbf{r}) = \sum_i \phi_i^*(\mathbf{r})\phi_i(\mathbf{r}) \tag{2.9}$$

where $\{\phi_i(\mathbf{r})\}$ are orthonormal molecular orbitals. Such a decomposition is valid for the ground-state density of any non-interacting system and is extended to any interacting one, thanks to the Kohn-Sham assumption.

To write down the energy functional $E^{(HK)}[n(\mathbf{r}); v_{ext}(\mathbf{r})]$ it is necessary to explicit various contributions in the functional form, within the Kohn-Sham approach. The electron-electron Coulomb interaction (called Hartree potential) can be extracted in the following form:

$$V_H[n] = \frac{1}{2}\sum_{i,j} \langle \phi_i\phi_j | \frac{e^2}{r_{12}} | \phi_i\phi_j \rangle . \tag{2.10}$$

Similarly, the electrons kinetic energy can be expressed as:

$$T_0[n] = \sum_i \langle \phi_i | -\frac{\hbar^2\nabla^2}{2m} | \phi_i \rangle . \tag{2.11}$$

Exploting also Equation (2.3), the energy functional $E^{(HK)}[n(\mathbf{r}); v_{ext}(\mathbf{r})]$ can be written as:

$$E^{(HK)}[n(\mathbf{r}); v_{ext}(\mathbf{r})] = T_0[n] + V_H[n] + \int v_{ext}(\mathbf{r})n(\mathbf{r})d\mathbf{r} + E_{xc}[n] \tag{2.12}$$

where the *exchange-correlation functional* $E_{xc}[n]$ is defined as:

$$E_{xc}[n] = T[n] - T_0[n] + V_{ee}[n] - V_H[n]. \tag{2.13}$$

The $E_{xc}[n]$ term has to be intended as the difference between the actual electron kinetic energy and electron-electron Coulomb interaction and their form within the Kohn-Sham approach. The energy functional $E^{(HK)}[n(\mathbf{r}); v_{ext}(\mathbf{r})]$ can be now recast as:

$$E^{(HK)}[n(\mathbf{r}); v_{ext}(\mathbf{r})] = \sum_i \langle \phi_i | -\frac{\hbar^2 \nabla^2}{2m} + v_{ext} | \phi_i \rangle + \frac{1}{2} \sum_{i,j} \langle \phi_i \phi_j | \frac{e^2}{r_{12}} | \phi_i \phi_j \rangle + E_{xc}[n]. \tag{2.14}$$

According to the standard variational procedure, the N contributing orbitals $\phi_1, \phi_2, ..., \phi_N$ are varied, under the constraint of normalization of the wavefunctions $\{\phi_i\}$. The variational calculation leads to the so-called Kohn-Sham equations:

$$[-\frac{\hbar^2 \nabla^2}{2m} + V_{nucl}(\mathbf{r}) + V_{coul}(\mathbf{r}) + V_{xc}(\mathbf{r})]\phi_i(\mathbf{r}) = \varepsilon_i \phi_i(\mathbf{r}) \tag{2.15}$$

where $V_{nucl}(\mathbf{r})$ denotes the external potential, $V_{coul}(\mathbf{r})$ the Hartree potential, and $V_{xc}(\mathbf{r})$ the functional derivative of $E_{xc}[n]$, defined as follows:

$$V_{xc}(\mathbf{r}) \equiv \frac{\delta E_{xc}[n]}{\delta n(\mathbf{r})}. \tag{2.16}$$

Solving these equations allow the determination of the so-called Kohn-Sham orbitals and their energies, which can be used for writing the total ground-state energy of the electronic system:

$$E_0 = \sum_i \varepsilon_i - \frac{1}{2} \sum_{i,j} \langle \phi_i \phi_j | \frac{e^2}{r_{12}} | \phi_i \phi_j \rangle + E_{xc}[n] - \int V_{xc}(\mathbf{r}) n(\mathbf{r}) d\mathbf{r}. \tag{2.17}$$

Conceptually, the orbital energies ε_i appearing in Equation (2.15) are formal Lagrange multipliers and can not be systematically interpreted as one-particle energies (according to any Koopmans'-like theorem) and the Kohn-Sham orbitals are not *real* orbitals. Any identification of ε_i and ϕ_i with (occupied or non-occupied) one-particle energies and orbitals is to be justified situation by situation.

Most of the difficulties (and consequently most of the efforts) in the procedure are confined to the search for a reasonable guess of the exchange-correlation functional $E_{xc}[n]$ (which is known only in principle).

2.1.3 Local density approximation

The simplest workable approximation for the exchange-correlation functional $E_{xc}[n]$ is the *local density approximation* (LDA). Within the LDA approach, the electron density $n(\mathbf{r})$ is approximated as the one of a uniform electron gas. This assumption is valid for systems with reasonably slowly varying spatial density n(r), such

as metals. On the contrary, the LDA does not work properly for molecular systems, where the electron density varies significantly even with small changes in the spatial variables.

In the LDA, the exchange functional $E_x[n]$ is approximated in the form:

$$E_x^{LDA}[n] = -C_x \int n^{\frac{4}{3}}(\mathbf{r}) d\mathbf{r} \tag{2.18}$$

with

$$\varepsilon_x^{LDA} = -C_x n^{\frac{1}{3}}. \tag{2.19}$$

In the case of spin-polarized systems, i.e., systems with different α and β spin density, the *local spin density approximation* is used to consider both spin contributions separately:

$$E_x^{LSDA}[n] = -2^{\frac{1}{3}} C_x \int (n_\alpha^{\frac{4}{3}} + n_\beta^{\frac{4}{3}}) d\mathbf{r}. \tag{2.20}$$

The analytical definition of the correlation functional $E_c[n]$ is obtained through the interpolation of data computed at a different level of theory.

2.1.4 Generalized gradient approximation

The *generalized gradient approximation* (GGA) includes in the functional definition not only the electron density $n(\mathbf{r})$, as the LDA does, but also its spatial derivative. The GGA functionals are still *local*, as the LDA ones, since they depends on the electron density and its spatial derivative in a precise and unique point $\mathbf{r}$ of the space.

One of the first GGA exchange functional was proposed by A. D. Becke [226] with the name B88 as a correction to the LDA exchange one:

$$\varepsilon_x^{B88} = \varepsilon_x^{LDA} + \Delta\varepsilon_x^{B88} \tag{2.21}$$

with

$$\Delta\varepsilon_x^{B88} = -\beta n^{\frac{1}{3}} \frac{x^2}{1 + 6\beta x \sinh^{-1} x}, \quad x = \frac{|\nabla n|}{n^{\frac{4}{3}}}. \tag{2.22}$$

The β parameter is determined by interpolation of data obtained at higher levels of theory. Regarding the correlation contribution, one of the first GGA correlation functional was proposed by Lee, Yang, and Parr [227] with the name LYP; for simplicity, we omit its analytical form, which contains parameters determined, as well as in the case of the exchange, by the fitting of data obtained at higher levels of theory. The combination of the GGA exchange functional B88 and the GGA correlation functional LYP leads to the so-called BLYP exchange-correlation functional [228].

Perdew, Burke, and Ernzerhof [229] proposed another exchange-correlation functional with the name PBE. The exchange part is obtained by multiplying the LDA term by a function:

$$\varepsilon_x^{PBE} = \varepsilon_x^{LDA} F(x), \quad F(x) = 1 + a - \frac{a}{1 + bx^2} \tag{2.23}$$

where x is defined as in Equation 2.22. Regarding the correlation part, the functional is obtained by summing a function to the LDA expression:

$$\varepsilon_c^{PBE} = \varepsilon_c^{LDA} H(t), \quad H(t) = c f_3^3 \ln\left[1 + dt^2 \left(\frac{1 + At^2}{1 + At^2 + A^2 t^4}\right)\right]. \tag{2.24}$$

Again, the parameters are determined by interpolation of data obtained at higher levels of theory.

2.1.5 Hybrid functionals

Hybrid functional are so called because they present a term calculated as defined in the Hartree-Fock approach. In particular, hybrid functionals present a contribution (tuned by an optimized coefficient) of exact exchange energy as computed at the Hartree-Fock level.

B3LYP [230] is an example of hybrid functional. The correlation functional is given by the sum of L(S)DA and GGA LYP correlation functional. The exchange functional is given by the L(S)DA exchange functional corrected by the GGA B88 exchange functional and the exact Hatree-Fock exchange. All the terms defining the B3LYP exchange-correlation functional are weighted by optimized parameters as shown in the following:

$$E_{xc}^{B3LYP} = (1 - a) E_x^{L(S)DA} + a E_x^{HF} + b \Delta E_x^{B88} + (1 - c) E_c^{L(S)DA} + c E_c^{LYP}. \tag{2.25}$$

PBE0 [231, 232] (also known as PBE1PBE) is another example of hybrid functional. It has been derived by introducing the exact Hartee-Fock exchange into the GGA PBE exchange-correlation functional. PBE0 has been improved by Heyd, Scuseria, and Ernzerhof [233]. The so-called HSE hybrid functional [233] presents the same correlation contribution of the GGA PBE (and the hybrid PBE0), whereas the exchange contribution is defined depending on the ranginess (short or long) of the interaction:

$$E_{xc}^{HSE} = a E_x^{HF,SR}(\omega) + (1 - a) E_x^{PBE,SR}(\omega) + E_x^{PBE,LR}(\omega) + E_c^{PBE}. \tag{2.26}$$

The first three terms are related to the exchange interaction. In particular, the first two terms are related to the short-range (SR) interaction, whereas the third

one to the long-range (LR) interaction. The GGA PBE exchange functional and the exact Hartree-Fock exchange (weighted by optimized parameters) contributes to the short-range exchange interaction. The adjustable ω parameter controls the short/long-ranginess of the interaction; once it is assumed to be 0, the HSE functional degenerates in the PBE0 one. The functional is usually called HSE06 with the standard values of 0.20 and 0.25 for ω and a, respectively.

2.2 Density functional tight-binding

The Kohn-Sham approach within the framework of the density functional theory (KS-DFT) paved the way to the extensive and intensive performance of simulations for investigating chemical and physical properties at atomistic level of molecules and condensed matter. Although researchers are still looking for a generally, if not universally, accurate exchange-correlation functional, by choosing the proper functional for the system under investigation, it is already possible to get an accuracy comparable with the one of more sophisticated methods. In the meanwhile, the increasing efficiency of both software and hardware has allowed to study systems characterized by bigger and bigger dimensions and complexity. However, there are still limits: the study of systems made by hundreds or thousands of atoms make the calculations extremely time and computationally demanding, if not unfeasible. To overcome these limitations, more approximated methods are required. In this context, in mid-1990s Seifert, Elstner, Frauenheim and collaborators [234] proposed the *density functional tight-binding* (DFTB) method, which turns the KS-DFT approach into a tight-binding scheme.

The DFTB equations are obtained from the DFT ones; more detailed information about the derivation can be found in References [221, 235–237]. As detailed in Section 2.1, the DFT total energy of an interacting electron system can be expressed with the formula:

$$E = T + V_{ext} + V_{ee} + V_{II} \tag{2.27}$$

where T is the electrons kinetic energy, V_{ext} the external potential (electron-ion Coulomb interaction), V_{ee} the electron-electron interactions energy, and V_{II} ion-ion interactions energy. Through the Kohn-Sham approach, Equation (2.27) can be rearranged as:

$$E[n(\mathbf{r})] = T_0 + V_{ext} + V_H + E_{xc} + E_{II} \tag{2.28}$$

where the exchange-correlation functional E_{xc} is defined in Equation (2.13). The total energy can be rewritten as previously done in Equation (2.14) and adding a term for the ion-ion interaction. So far everything is exact, but now approximations are needed. Consider a system with density $n_0(\mathbf{r})$ that is composed of atomic

densities, as if atoms in the system were free and neutral. Consequently, $n_0(\mathbf{r})$ contains (by definition) no charge transfer. The density $n_0(\mathbf{r})$ does not minimize the functional $E[n(\mathbf{r})]$, but neighbors the true minimizing density $n_0(\mathbf{r}) + \delta n_0(\mathbf{r})$, where $\delta n_0(\mathbf{r})$ is supposed to be small. Expanding the total energy $E[n(\mathbf{r})]$ at $n_0(\mathbf{r})$ to second order with the fluctuation $\delta n(\mathbf{r})$ we get:

$$\begin{aligned} E[\delta n] \approx \sum_a f_a \left\langle \phi_a \right| -\frac{1}{2}\nabla^2 + V_{ext} + V_H[n_0] + V_{xc}[n_0] \left| \phi_a \right\rangle] \\ + \frac{1}{2}\iint{}' \left(\frac{\delta^2 E_{xc}[n_0]}{\delta n \delta n'} + \frac{1}{|\mathbf{r}-\mathbf{r}'|}\right)\delta n \delta n' \\ -\frac{1}{2}\int V_H[n_0](\mathbf{r}) n_0(\mathbf{r}) + E_{xc}[n_0] + E_{II} - \int V_{xc}[n_0](\mathbf{r}) n_0(\mathbf{r}) \end{aligned} \tag{2.29}$$

where f_a is Fermi-Dirac distribution and the linear terms in $\delta n(\mathbf{r})$ vanish. The first term is the so-called *band-structure energy* and depends only on $n_0(\mathbf{r})$ with the Hamiltonian $H^0 = H[n_0]$, and hence it contains no charge transfer contribution:

$$E_{BS}[\delta n] = \sum_a f_a \left\langle \phi_a \right| H[n_0] \left| \phi_a \right\rangle . \tag{2.30}$$

The second term represent (through the Coulomb and exchange-correlation interactions) the charge fluctuations contribution:

$$E_{coul}[\delta n] = \frac{1}{2}\iint{}' \left(\frac{\delta^2 E_{xc}[n_0]}{\delta n \delta n'} + \frac{1}{|\mathbf{r}-\mathbf{r}'|}\right)\delta n \delta n'. \tag{2.31}$$

The last four terms are collectively called the repulsive energy E_{rep}:

$$E_{rep} = -\frac{1}{2}\int V_H[n_0](\mathbf{r}) n_0(\mathbf{r}) + E_{xc}[n_0] + E_{II} - \int V_{xc}[n_0](\mathbf{r}) n_0(\mathbf{r}). \tag{2.32}$$

The band-structure energy E_{BS} term can be written with the tight-binding approach, which assumes *tightly bound* electrons, using minimal local basis to expand single-electron orbitals ϕ_a:

$$\phi_a(\mathbf{r}) = \sum_\mu c_\mu^a \varphi_\mu(\mathbf{r}). \tag{2.33}$$

Minimality means having only one radial function for each angular momentum state: one for s-states, three for p-states, five for d-states, and so on. With this expansion the band-structure energy becomes:

$$E_{BS} = \sum_a f_a \sum_{\mu\nu} c_\mu^{a*} c_\nu^a H^0_{\mu\nu} \tag{2.34}$$

where

$$H^0_{\mu\nu} = \langle \varphi_\mu | \, H^0 \, | \varphi_\nu \rangle \, . \tag{2.35}$$

In the tight-binding spirit, the matrix elements $H^0_{\mu\nu}$ are just numbers. These matrix elements (i.e., integrals) and the ones of the overlap matrix $S_{\mu\nu}$ (which arises and is defined during the variational procedure, see below) can be computed easily and fast, but still accurately, thanks to the spherical harmonics properties and the *Slater-Koster transformation rules*. These rules govern the dependence of the integrals on the distance $\mathbf{R}_{IJ}$ between the two atoms I and J and the two basis functions belonging to them. The procedure is hence the following: the required Slater–Koster integrals are integrated numerically for a set of $\mathbf{R}_{IJ}$ and stored in a table. This is done once for all orbital pairs. Then, for a given orbital pair, the table is interpolated for the $\mathbf{R}_{IJ}$ given by the geometry of the system under investigation and the integrals are computed fast and accurately. Some approximations are needed to exploit such approach for the matrix elements $H^0_{\mu\nu}$, which are three-center integrals and in principle can not depend only on the two-center variable R_{IJ}. In particular, the integrand is a product of factors with three centers (two basis functions and one potential), which are non-null in small spatial regions only. First, for diagonal elements $H_{\mu\mu}$ a one-center approximation can be made: the potential is centered on the atom I where the basis function φ_μ is centered. As a consequence, this integral is approximately equal to the energy ε_μ of free atom orbital. Second, for off-diagonal elements $H_{\mu\nu}$ a two-center approximation can be made: with μ localized around atom I and ν around atom J, the potential is given by the sum of the two free atom potentials centered on I and J. This approximation is reasonable because the integrand is large when the potential is localized either around I or J as well and the crystal field contribution from other atoms can be neglected.

The repulsive energy E_{rep} term contains the ion–ion interaction so it is repulsive (at least at small atomic distances), but it contains also exchange-correlation interactions. It can be considered as a practical equivalent to an exchange-correlation functional in DFT because it hides the cumbersome physics, while it is approximated with simple functions. In particular, E_{rep} is approximated as a sum of terms over atom pairs, where each term depends only on elements and their distance:

$$E_{rep} = \sum_{I<J} V^{IJ}_{rep}(R_{IJ}) \tag{2.36}$$

where IJ indicates the pair of atoms and $V^{IJ}_{rep}(R_{IJ})$ represents the IJ pair-wise repulsive function, which depends only on the atomic numbers and distance of the IJ pair. The pair-wise repulsive functions $V^{IJ}_{rep}(R_{IJ})$ are obtained by fitting to high-level theoretical calculations.

The E_{coul} term contains the charge fluctuations $\delta n(\mathbf{r})$, that can be used to calculate the extra electron population Δq_I on an atom I:

$$\Delta q_I = \int_I \delta n(\mathbf{r}) d^3 r. \tag{2.37}$$

By using the atomic populations, $\delta n(\mathbf{r})$ can be decomposed into atomic contributions:

$$\delta n(\mathbf{r}) = \sum_I \Delta q_I \delta n_I(\mathbf{r}). \tag{2.38}$$

Further elaborations allow to write E_{coul} as:

$$E_{coul} = \frac{1}{2} \sum_{IJ} \gamma_{IJ} \Delta q_I \Delta q_J. \tag{2.39}$$

Now, the total energy can be written as:

$$E = \sum_a f_a \sum_{\mu\nu} c_\mu^{a*} c_\nu^a H_{\mu\nu}^0 + \frac{1}{2} \sum_{IJ} \gamma_{IJ} \Delta q_I \Delta q_J + \sum_{I<J} V_{rep}^{IJ}(R_{IJ}). \tag{2.40}$$

If the charge fluctuations contribution to the total energy is neglected, the electronic problem can be solved without any self-consistent method, because E_{BS} and E_{rep} depend only on free atom orbitals and fitted pair-wise repulsive functions. In this case, the method is called DFTB-0, or simply DFTB. When considering the charge fluctuations contribution to the total energy, self-consistent algorithms are required to find the atomic charge fluctuations Δq_I that minimize the total energy functional. The variational procedure leads to the Kohn-Sham equations-equivalent in DFTB:

$$\sum_\nu c_\nu^a (H_{\mu\nu} - \varepsilon_a S_{\mu\nu}) = 0 \tag{2.41}$$

where

$$H_{\mu\nu} = H_{\mu\nu}^0 + \frac{1}{2} S_{\mu\nu} \sum_K (\gamma_{IK} + \gamma_{JK}) \Delta q_K, \quad \mu \in I \quad \nu \in J. \tag{2.42}$$

The variational and iterative process involves not only the coefficients $\{c_\mu\}$, but also the atomic charge fluctuations $\{\Delta q_I\}$. This method is known as DFTB-2 or SCC-DFTB, where SCC stands for *self-consistent redistribution of charges*.

2.3 Bloch's theorem and periodic boundaries conditions

In molecular computational chemistry, the unknown single-electron *molecular orbitals* (MOs) are expanded in a finite set of basis functions that can be identified *atomic orbitals* (AOs), following the familiar LCAO (Linear Combination of

Atomic Orbitals) approach. The linear combinations coefficients are then determined variationally by solving the corresponding set of matrix equations. When working with solids, things become a little bit more complicated because of the infinite dimensions involved. However, taking into account the translational symmetry and using a set of Bloch functions as basis functions to build the single electron *crystalline orbitals* (COs, the equivalent of MOs in solids), the problem can be factorized and hence solved as in the molecular case.

A function that satisfies the Bloch's theorem is called Bloch function. The Bloch theorem relies only on the assumption that the potential is periodic as the crystal lattice is:

$$V(\mathbf{r}) = V(\mathbf{r} + \mathbf{R}),\ \mathbf{R} = l_1\mathbf{a}_1 + l_2\mathbf{a}_2 + l_3\mathbf{a}_3 \tag{2.43}$$

where $\mathbf{r}$ is the position vector, $\mathbf{R}$ is a direct lattice vector, $\mathbf{a}_i$ are the basis of the direct lattice and l_i are integers. The Bloch's theorem states that solutions to the Schrödinger equation in a periodic potential take the form of a plane wave modulated by a periodic function:

$$\psi^{\mathbf{k}}(\mathbf{r}) = u^{\mathbf{k}}(\mathbf{r})e^{i\mathbf{k}\cdot\mathbf{r}} \tag{2.44}$$

where $\mathbf{k}$ is the position vector in the reciprocal space (i.e., the space where the Schrödinger equations are solved and the electronic structures are investigated) and the modulation function $u^{\mathbf{k}}(\mathbf{r})$ has the periodicity of the direct lattice:

$$u^{\mathbf{k}}(\mathbf{r}) = u^{\mathbf{k}}(\mathbf{r} + \mathbf{R}). \tag{2.45}$$

The Bloch's theorem can be cast also in a different way:

$$\psi^{\mathbf{k}}(\mathbf{r} + \mathbf{R}) = e^{i\mathbf{k}\cdot\mathbf{R}}\psi^{\mathbf{k}}(\mathbf{r}). \tag{2.46}$$

The second formulation of the Bloch's theorem here reported (Equation (2.46)) suggests that a generic solution of the Schrödinger equation modulated by a plane wave has the periodicity of the crystal lattice. In the reciprocal space the eigenvectors and the eigenvalues of the Schrödinger equation have the same identical periodicity of the reciprocal lattice:

$$\psi_n^{\mathbf{k}+\mathbf{K}} = \psi_n^{\mathbf{k}} \tag{2.47}$$

$$\varepsilon_n^{\mathbf{k}+\mathbf{K}} = \varepsilon_n^{\mathbf{k}} \tag{2.48}$$

where $\mathbf{K}$ represents a reciprocal lattice vector, $\psi_n^{\mathbf{k}}(\mathbf{r})$ and $\varepsilon_n^{\mathbf{k}}$ the eigenvectors and eigenvalues, respectively, of a generic Schrödinger problem. Since both $\psi_n^{\mathbf{k}}(\mathbf{r})$ and $\varepsilon_n^{\mathbf{k}}$ are periodic in the reciprocal space, we only need to know these functions for

k-values in the first Brillouin zone, i.e., the Wigner-Seitz (primitive) cell of the reciprocal lattice.

When mentioning a solid, we refer to a finite macroscopic system constituted by $M = M_1 \cdot M_2 \cdot M_3$ unit cells, whose sides are $M_i \cdot \mathbf{a}_i$. Under normal conditions, due to the macroscopic dimensions, we can expect the bulk properties to be insensitive to the surface and to the boundary conditions. So, it is reasonable assume that our finite macroscopic solid is part of an infinite crystal. It is then assumed that the single-electron wave function obeys the following *Born-Von Karman* or *periodic boundary conditions*:

$$\psi^{\mathbf{k}}(\mathbf{r} + M_i\mathbf{a}_i) = \psi^{\mathbf{k}}(\mathbf{r}) \quad \text{for} \quad i = 1, 2, 3. \tag{2.49}$$

Applying this condition to a Bloch function, one gets:

$$\psi^{\mathbf{k}}(\mathbf{r} + M_i\mathbf{a}_i) = e^{iM_i\mathbf{k}\cdot\mathbf{a}_i}\psi_k(\mathbf{r}) = \psi_k(\mathbf{r}) \tag{2.50}$$

which implies

$$e^{iM_i\mathbf{k}\cdot\mathbf{a}_i} = 1 \tag{2.51}$$

which leads to

$$M_i\mathbf{k}_i\mathbf{a}_i = 2\pi m_i \tag{2.52}$$

where m_i are integer. Equation (2.52) defines the allowed **k** vectors inside the unit reciprocal cell:

$$\mathbf{k} = \frac{m_1}{M_1}\frac{2\pi}{\mathbf{a}_1} + \frac{m_2}{M_2}\frac{2\pi}{\mathbf{a}_2} + \frac{m_3}{M_3}\frac{2\pi}{\mathbf{a}_3} \quad \text{for} \quad m_i = 0, 1, 2, ..., N_i \tag{2.53}$$

where $\mathbf{b}_i = \frac{2\pi}{\mathbf{a}_i}$ are the basis of the reciprocal lattice. From Equation (2.53), each **k** point can be attributed a small parallelepiped with edges $2\pi/M_i a_i$ and volume $(2\pi)^3/VM$, where V is the volume of the direct lattice cell. These equations show that the number of **k** points in the reciprocal primitive cell, i.e., the first Brillouin zone, is equal to M. If the number of unit cells in the crystal M increases, the **k** points get closer and closer; at the limit of an infinite crystal, **k** becomes a continuous variable.

As a consequence, both $\psi_n^{\mathbf{k}}(\mathbf{r})$ and $\varepsilon_n^{\mathbf{k}}$ are continuous functions of **k**, while remaining discrete with respect to n. The continuous nature of $\varepsilon_n^{\mathbf{k}}$ leads to the so-called band structure of solids and entails the problem of counting the number of states in a given energy interval. To solve this problem, the concept of *Density of States* (DOS) has been introduced. We often have to calculate weighted sums WS over functions f of the electronic single-electron levels:

$$WS = 2\sum_{n,\mathbf{k}} f(\varepsilon_n^{\mathbf{k}}) \tag{2.54}$$

where the factor 2 accounts for electrons having opposite spin. By the definition of Dirac *delta* function (δ), it is possible to write:

$$WS = 2\sum_{n,\mathbf{k}} f(\varepsilon_n^{\mathbf{k}}) = 2\sum_{n,\mathbf{k}} \int f(\varepsilon)\delta(\varepsilon - \varepsilon_n^{\mathbf{k}})d\varepsilon = \int f(\varepsilon)n(\varepsilon)d\varepsilon \tag{2.55}$$

where

$$n(\varepsilon) = 2\sum_{n,\mathbf{k}} \delta(\varepsilon - \varepsilon_n^{\mathbf{k}}) = \frac{2}{V_{BZ}} \sum_n {\int}' \delta(\varepsilon - \varepsilon_n^{\mathbf{k}})d\mathbf{k} \tag{2.56}$$

is the DOS. The prime indicates that the integral (or eventually the sum) extends only to the points in the selected portion of the Brillouin zone. The number of electrons in the unit cell is given by:

$$\int_{-\infty}^{\varepsilon_F} n(\varepsilon)d\varepsilon \tag{2.57}$$

where ε_F is the Fermi energy.

From a computational point of view, grids with various finite densities of **k**-points are often used to explore the reciprocal space and solve the Schrödinger equations. Hence, when calculating weighted sums over functions of the electronic single-electron levels, e.g., DOS, integrals are not computed analytically but as sums of a finite number of terms.

In solid state computational chemistry and physics, a finite set of Bloch functions $\chi_\mu^{\mathbf{k}}(\mathbf{r})$ are used to expand the unknown single-electron COs $\phi_n^{\mathbf{k}}(\mathbf{r})$, that have to be Bloch functions, too:

$$\phi_n^{\mathbf{k}}(\mathbf{r}) = \sum_\mu c_{\mu n}^{\mathbf{k}} \chi_\mu^{\mathbf{k}}(\mathbf{r}). \tag{2.58}$$

As already mentioned, the coefficients $c_{\mu n}^{\mathbf{k}}$ are determined variationally by solving the corresponding set of matrix equations. Two main types of Bloch functions can be used for the expansion in Equation (2.58):
a) plane waves:

$$\chi_{\mathbf{K}}^{\mathbf{k}}(\mathbf{r}) = e^{i\mathbf{r}\cdot(\mathbf{k}+\mathbf{K})} \tag{2.59}$$

as immediate consequence of the form of Equation 2.46.
b) Bloch functions based on localized functions (sometimes called AOs):

$$\chi_{\mathbf{K}}^{\mathbf{k}}(\mathbf{r}) = \sum_{\mathbf{R}} e^{i\mathbf{k}\cdot\mathbf{R}} \varphi_\mu(\mathbf{r} - \mathbf{A}_\varphi - \mathbf{R}) \tag{2.60}$$

where μ labels the AOs in the unit cell, and $\mathbf{A}_\mu$ is the position of the atom on which the AO μ is centered. The AOs φ are usually linear combinations of the products of Gaussian functions by real, solid harmonics. The calculations reported in the present PhD thesis were performed through software that adopt this approach.

2.4 Geometry optimization

The geometry optimization is the process of finding a structural configuration, i.e., an arrangement in space of a collection of atoms, that has the net inter-atomic forces on each atom acceptably close to zero and corresponds to a minimum in the *potential energy surface* (PES). Such a process aims to minimize the energy of the system exploring the PES by modifying gradually the atomic positions. Nowadays, several geometry optimization algorithm are available.

When using the CRYSTAL17 software, the geometry optimization calculations were performed through the BFGS method, which is a Quasi-Newton method. Quasi-Newton methods, as the name suggests, are approximated Newton methods that are exploited when the Hessian is unavailable or is too expensive to compute at every iteration. For simplicity, let us consider the *full* Newton method in the monodimensional case $E = E(x)$. To find the points on the PES where $dE/dx = 0$, i.e., stationary points, dE/dx is expanded in power series with respect to a tentative point x^0:

$$(\frac{dE}{dx})_x = (\frac{dE}{dx})_{x^0} + (\frac{d^2E}{dx^2})_{x^0}(x - x^0) + ... = 0. \tag{2.61}$$

Truncating the expansion to the second order, the increment so that the tentative point x^0 reaches the minimum x is:

$$(x - x^0) = -(\frac{dE}{dx})_{x^0}/(\frac{d^2E}{dx^2})_{x^0}. \tag{2.62}$$

If energy were a function of x^2, i.e., if the truncation at the second order of the expansion in Equation (2.61) were not an approximation, the displacement $(x-x^0)$ would lead directly to the minimum. Practically, energy presents often a more complicated x-dependence, and hence an iterative process is necessary. Then, generalizing to the n-dimensional case $E = E(x_1, x_2, ..., x_n)$, our aim is to find the point $\mathbf{x} = (x_1, x_2, ..., x_n)$ on the PES where all the n first derivatives dE/dx_i are equal to zero. Given the tentative point $\mathbf{x}^0 = (x_1^0, x_2^0, ..., x_n^0)$ and proceeding as done for the monodimensional case, we get:

$$\mathbf{g}_\mathbf{x} = \mathbf{g}_{\mathbf{x}^0} + H_{\mathbf{x}^0}(\mathbf{x} - \mathbf{x}^0) + ... = 0 \tag{2.63}$$

where $\mathbf{g}$ is the gradient vector, and H the Hessian matrix. From Equation (2.63) it is straightforward to derive:

$$(\mathbf{x} - \mathbf{x}^0) = -(H_{\mathbf{x}^0})^{-1}\mathbf{g}_{\mathbf{x}^0}. \tag{2.64}$$

Quasi-Newton methods, such as BFGS, approximate the Hessian since it is to expensive to compute at every iteration.

When using the DFTB+ software, the geometry optimization calculations were performed through the *Conjugate Gradient* (CG) method, which is an improvement of the *Steepest Descent* (SD) method. For simplicity, let us consider initially the latter one. To determine minima points $\mathbf{x} = (x_1, x_2, ..., x_n)$ of the function $E = E(x_1, x_2, ..., x_n)$, the SD imposes a tentative point $\mathbf{x}^0 = (x_1^0, x_2^0, ..., x_n^0)$ to *descend* in the opposite direction of the gradient $\mathbf{g}$ calculated in the tentative point $\mathbf{x}^0$ it self. The descent is given by an iterative procedure which updates the starting point according the equation:

$$\mathbf{x}_{k+1} = \mathbf{x}_k + \alpha_k \mathbf{p}_k \tag{2.65}$$

where α_k is a real number that defines the *steepness* of the descent, i.e., the convergence rate, and $\mathbf{p}_k$ is the descent direction defined as:

$$\mathbf{p}_k = -\nabla E(\mathbf{x}_k) = -\mathbf{g}_k. \tag{2.66}$$

The CG method defines the direction of the displacement along the PES not only calculating the gradient in $\mathbf{x}_k$, but considering also the direction of the previous movement, i.e., the gradient in $\mathbf{x}_{k-1}$, according to the equation:

$$\mathbf{p}_k = -\mathbf{g}_k + \beta_k \mathbf{p}_{k-1} \tag{2.67}$$

where the β_k parameter can be tuned in different ways. The CG definition of the *descent* direction makes the convergence faster and more robust with respect the case of the SD one.

Chapter 3

Effect of Surface Functionalization on the Magnetization of Fe_3O_4 Nanoparticles

In this chapter, we studied the effect of surface functionalization on the magnetization of magnetite (Fe_3O_4) nanoparticles. Saturation magnetization values close to the bulk have been reported for coated Fe_3O_4 nanoparticles with organic acids, but the underlying mechanism is still to be clarified. Through a wide set of hybrid density functional theory (HSE06) calculations on Fe_3O_4 nanocubes of more than 400 atoms, we explored the effects of the adsorption of various ligands (containing hydroxyl, carboxylic, phosphonic, catechol, and silanetriol groups), commonly used to anchor surfactants during synthesis or other species during chemical reactions, onto the spin and structural disorder, which contribute to the lowering of the nanoparticle magnetization. We simulated the spin canting (i.e., the spin disorder) through a spin-flip process at octahedral Fe ions and correlated with the energy separation between O^{-II} $2p$ and Fe^{III}_{Oct} $3d$ states. We found that only multidentate bridging ligands hamper the spin canting process by establishing additional electronic channels between octahedral Fe ions for an enhanced ferromagnetic superexchange interaction. We also observed that the presence of anchoring organic acids interferes with structural disorder, by disfavoring surface reconstruction.

The results reported in this chapter have been published in: Bianchetti, E.; Di Valentin, C. *Materials Today Nano* **2022**, *17*, 100169, and Bianchetti, E.; Di Valentin, C. *Journal of Physical Chemistry Letters* **2022**, *13*, 9348-9354.

3.1 Introduction

Magnetic nanoparticles (NPs) have attracted much attention for diagnostic and theragnostic medical applications, due to their small size, which is comparable to cell length scales and allows the interaction and interference with biological processes, however minimizing adverse effects and, thus, paving the way to novel approaches. Among them, iron oxides nanoparticles (IONPs) have been playing a predominant role in nanomedicine, as contrast agents for magnetic resonance imaging (MRI), magnetic hyperthermia sources or drug delivery vehicles [9–14, 147], due to their biocompatibility [134, 135], low cost, high saturation magnetization [17] and versatile surface chemistry for easy functionalization [136]. Magnetite (Fe_3O_4) NPs are the first inorganic materials that have been clinically tested and approved for commercialization [238].

Magnetite NPs of different and controlled sizes and shapes have been prepared through a variety of synthetic routes [17, 87–95]; however, cubic NPs enclosed by six (001) facets are ones of the most commonly observed and their shape is compatible with the cubic unit cell of the inverse spinel crystal structure of Fe_3O_4 [96]. The O anions are organized in a face-centered cubic arrangement. The iron cations are either Fe^{II} or Fe^{III} in a 1:2 ratio. All Fe^{II} ions occupy octahedral sites (Fe_{Oct}) in a random distribution with half of the Fe^{III} ions, whereas the other half of Fe^{III} ions occupy tetrahedral sites (Fe_{Tet}).

The magnetic ordering in bulk magnetite derives from this structure organization of the Fe cations [4, 5]. Since the Fe−Fe distances are too large for direct exchange, the superexchange through the O anions (Fe−O−Fe) is dominant and controls the magnetic interaction: being the Fe_{Oct}−O−Fe_{Tet} angle close to 125°, an antiferromagnetic (AFM) alignment is expected between the Fe_{Oct} and the Fe_{Tet} sublattices, which leads to a net ferrimagnetic order since the Fe_{Oct} ions are twice the Fe_{Tet} ions. The superexchange interaction in the case of Fe_{Oct}−O−Fe_{Oct} is ferromagnetic (FM) because the angle is 90°. The magnetic moment per formula unit is around 4 μ_B [239].

However, the magnetic properties of NPs are not as excellent as those of bulk magnetite, with a saturation magnetization that is largely reduced due to a combination of several contributing factors. The three, generally recognized, main causes of reduced magnetization are: the presence of antiphase domains [97–99], a low degree of crystallinity and surface spin canting (or disorder) effects [100–103].

Although NPs larger than 80 nm size are usually multidomain [108–110], there is still controversy on the minimum size of NPs where multidomains can coexist, depending on the synthetic route or preparation conditions [105]. In the present work we did not address this aspect for two reasons: first, because there is reasonable expectation that very small NPs (<25 nm), such as those that are typically used in nanomedical applications, are homogeneously magnetized and are stable

single domain [107]; second, because it has been already theoretically investigated in terms of Heisenberg spin Hamiltonian or through density functional theory with the Hubbard U correction (DFT+U) calculations [104, 105].

A loss in crystallinity at the surface layers has been often invoked as a cause of reduced saturation magnetization in NPs. It is well known that even the Fe_3O_4(001) surface, which constitutes one of the most stable type of magnetite surface [58, 59, 61, 62, 87], spontaneously reconstruct through an atomic reorganization where a loss in Fe:O stoichiometry is accompanied by the transfer of some subsurface octahedral Fe ions from the third layer into tetrahedral sites in the second layer [79]. Indeed, a previous work by my research group showed that a similar reconstruction takes place at the corners of cubic magnetite NPs enclosed by six (001) facets [125]. There, octahedral Fe ions around the corner were found to move into tetrahedral sites causing structural disorder. However, these surface reconstructions could be hampered using capping agents during NPs crystal growth, such as oleic acid, which is often used during NPs preparation.

Coated magnetic NPs were indeed found to present much higher saturation magnetization, almost close to the bulk value (96 emu/g), than naked ones [114–120], e.g., 84 vs 46 emu/g [119]. Another possible explanation, besides the reduced reconstruction, is that surface coating interferes with spin canting phenomena, but why and how it could improve the alignment of surface atom spins with the overall magnetization direction of the NP is still a big open question, especially because the covering organic acids are not magnetic.

Certainly, quantum mechanics is the only viable way to unveil the fundamental mechanisms governing the behavior of magnetic materials. However, no theoretical simulations have yet effectively proven the ability of coating molecules to enhance surface crystallinity and spin alignment of Fe_3O_4 NPs. For example, in a combined experimental and theoretical work, Salafranca et al. [120] proposed an explanation based on a set of density functional theory (DFT) calculations comparing electronic structure of bulk magnetite, bare (001) surface and capped surface with organic acids. However, the level of calculations and the results presented are not consistent with the existing literature. First, it was proven that the Fe_3O_4(001) surface undergoes a large reconstruction that was not considered in this work [79]. Second, several density functional theory calculations in other studies, using DFT+U or hybrid functionals [46, 70, 76, 86, 123, 124], clearly show a gap at Fermi level in the density of majority spin states for the unreconstructed bare (001) surface in total analogy with what observed for bulk [33, 45, 53], but in contrast with the metallic character observed by Salafranca et al. [120], on which fact they explain the reduced magnetization at magnetite surfaces.

In the present study accurate models and methods were used. In particular, we investigated *real* cubic NPs (not just flat surfaces) and we went beyond standard

DFT using a higher level theory method, i.e., the hybrid functional HSE06 [233, 240], which in the past was proved to be reliable to catch the proper structural, electronic, and magnetic properties of magnetite [33]. We explored the effects of the adsorption of various ligands (containing hydroxyl, carboxylic, phosphonic, catechol, and silanetriol groups), commonly used to anchor surfactants during synthesis or other species during chemical reactions [16, 136], onto the spin and structural disorder. The results strongly support the hypothesis that the high magnetism registered for coated NPs, close to the bulk value, should not simply be accounted for by a higher crystallinity of the samples at the surface but, it is also the result of a deeper involvement of the ligands in the mechanism of magnetization. The atomic level understanding achieved in this study indicates that the adsorbed bidentate ligands became involved in a ferromagnetic superexchange interaction with pairs of Fe_{Oct} ions, which works against spin canting and is the reason for the enhanced overall resulting magnetization.

3.2 Methods and models

For the initial structural screening of acetic acid adsorption modes at different coverages in terms of simulated annealing and geometry optimization, self-consistent charge density-functional tight-binding (SCC-DFTB) calculations were carried out using the software DFTB+ [241]. The SCC-DFTB is an approximated DFT-based method, as detailed in Section 2.2. Here, DFTB will be used as a shorthand for SCC-DFTB. For the Fe-Fe, Fe-H and Fe-C interactions, we used the "trans3d-0-1" set of parameters [242]. For the O-O, H-O, H-H, O-C, H-C and C-C interactions we used the "mio-1-1" set of parameters [234]. For the Fe-O interactions, we used the Slater-Koster files fitted by my group previously [243], which can well reproduce the results for magnetite bulk and surfaces from HSE06 and PBE+U calculations. To properly deal with the strong correlation effects among Fe $3d$ electrons [244], Hubbard-corrected DFTB (DFTB+U) with an effective U-J value of 3.5 eV was adopted according to previous work on magnetite by my group [125, 243, 245, 246]. The convergence criterion of 10^{-4} a.u. for forces and the convergence threshold on the SCC procedure of 10^{-5} a.u. were used during geometry optimization together with conjugate gradient optimization algorithm. DFTB+U molecular dynamics (MD) simulations were performed within the canonical ensemble (NVT) using an Andersen thermostat that simulates a temperature annealing process up to 500 K. The total simulation time is 30 ps with a time step of 1 fs. The convergence threshold on the SCC procedure was set to be $5{\cdot}10^{-3}$ a.u..

Hybrid DFT calculations (HSE06 [233, 240], see Section 2.1 for further details about the method) were carried out using the CRYSTAL17 package [247, 248] to investigate electronic and magnetic properties of both naked and coated

(with various ligands at different coverages) NPs. For the validation against experimental data of the standard hybrid functional HSE06 as a robust theoretical approach to describe structural, electronic and magnetic properties of magnetite system, please refer to ref. [33] and corresponding Supporting Information, where the effect of reducing the fraction of the exact exchange was analyzed, in comparison with B3LYP calculations and PBE+U calculations with different U values. The Kohn-Sham orbitals were expanded in Gaussian-type orbitals: the all-electron basis sets are H−511G(p1), C−6311G(d11), O−8411G(d1) (for NP oxygen atoms), O−8411G(d11) (for surfactant oxygen atoms), Si−86311(d1), P−8521G(d1), and Fe−86411G(d41). The convergence criterion of 10^{-6} hartree and $4.5{\cdot}10^{-4}$ hartree/bohr for total energy and forces, respectively, ere used during self-consistent field calculations and geometry optimization, according to the scheme previously used for Fe_3O_4 [33, 70, 125]. The same computational set-up is used for the toy model Fe(III) metoxide dimer, a simplified system of Fe(III) tert-butoxide dimer (CAS No. 620945-21-1).

The cubic nanoparticle model used for this investigation (429 atoms with edge length of 1.5 nm) was obtained from a larger one (1466 atoms with edge length of 2.3 nm), recently proposed by Liu and Di Valentin [125], by simply reducing the total number of atoms. Both these models are enclosed by six (001) facets, as observed in experiments [92, 93], and present the same type of corners, edges, and surface reconstruction, which consists of the transfer of three six-coordinated iron ions from octahedral to tetrahedral sites at four of the eight corners of the cube, i.e., those exposing tetrahedral Fe ions (from here on referred to as Fe-corner). The other four corners expose O ions (from here on referred to as O-corner). For more details regarding this reconstruction process, please refer to ref. [125]. Ligands coating is modeled at various different coverages: local low, local high, low, half, and full. The local low coverage is characterized by one single adsorbed ligand, whereas the local high coverage by two or three adsorbed ligands, in the proximity of the Fe_{Oct} ion under investigation. The low coverage is characterized by one adsorbed ligand per each single equivalent Fe_{Oct} ion under investigation. The half coverage presents half of the superficial under-coordinated Fe_{Oct} ions saturated by adsorbing 24 bidentate molecules, whereas at full coverage all of them are saturated by a total amount of 48 bidetate molecules. The total magnetization is computed according to the formula [125]:

$$m_{tot} = 5 \cdot [N(Fe^{\mathrm{III}}_{Oct}) - N(Fe^{\mathrm{III}}_{Tet})] + 4 \cdot [N(Fe^{\mathrm{II}}_{Oct}) - N(Fe^{\mathrm{II}}_{Tet})] \qquad (3.1)$$

where Fe^{III}_{Oct} and Fe^{II}_{Oct} are Fe^{III} and Fe^{II} ions at octahedral sites, Fe^{III}_{Tet} and Fe^{II}_{Tet} are Fe^{III} and Fe^{II} ions at tetrahedral sites and N is the number of the corresponding ions. Similarly to what happens in bulk magnetite, for Fe^{III}_{Oct} and Fe^{III}_{Tet} the high-spin $3d^5$ configuration gives an atomic magnetic moment of +5 and -5 μ_B,

respectively; for Fe^{II}_{Oct} and Fe^{II}_{Tet} the high-spin $3d^6$ electron configuration gives +4 and -4 μ_B, respectively. The total magnetic moment m_{tot} was found to be 288 μ_B for the cubic NP under investigation.

To mimic spin disorder phenomena, we have forced some Fe^{III}_{Oct} to give an atomic magnetic moment of -5 μ_B instead of +5 μ_B [249], lowering the total magnetic moment. We named the energy difference between spin-up and spin-down solutions as $\Delta E_{Spin-Flip}$. After the spin-flip we allowed for a full atomic relaxation of the NP and we named the energetic gain associated to the relaxation $\Delta E_{Relaxation}$. We called the sum of these two contributions ΔE_{SF+Rel}:

$$\Delta E_{SF+Rel} = \Delta E_{Spin-Flip} + \Delta E_{Relaxation}. \tag{3.2}$$

We note that the spin-flip of one Fe^{III}_{Oct} ion and four of them reduces the overall total magnetic moment of the NP from 288 to 278 and 248 μ_B, respectively.

In order to verify the agreement with the Equation (3.1) at different acetic acid coverage, we performed a series of HSE06 calculations, where we fully relaxed the NP atomic positions while varying the m_{tot}. The minimum total energy is registered for m_{tot} 248 (or 278) and 288 μ_B for the spin-flipped and for the non-spin-flipped system, respectively, in perfect agreement with the output by Equation (3.1).

For the toy model Fe^{III} metoxide dimer we have computed both the ferromagnetic (FM) and antiferromagnetic (AFM) configurations. In the first configuration, both high-spin $3d^5$ Fe^{III} ions give an atomic magnetic moment of +5 μ_b for an overall magnetic moment of +10 μ_B. In the second one, the high-spin $3d^5$ Fe^{III} ions give an atomic magnetic moment of +5 and -5 μ_B for a null overall magnetic moment. The ΔE_{AFM-FM} for this toy model is a quantity that corresponds to the ΔE_{SF+Rel} for the magnetite nanoparticles and is defined as:

$$\Delta E_{AFM-FM} = E_{AFM} - E_{FM} \tag{3.3}$$

where E_{AFM} and E_{FM} are the total energies of the antiferromagnetic and ferromagnetic configurations, respectively.

The adsorption energy per acetic acid molecule (E_{Ads}) was calculated as follows:

$$E_{Ads} = (E_{Total} - E_{NP} - N_{Molecule} \cdot E_{Molecule})/N_{Molecule} \tag{3.4}$$

where E_{Total} is the total energy of the whole system (NP and adsorbed molecules), E_{NP} is the energy of the Fe_3O_4 NP, $N_{Molecule}$ is the number of molecules adsorbed, and $E_{Molecule}$ is the energy of one isolated molecule. This formula provides a value for the adsorption energy that is normalized by the total number of acetic acids.

The band center of mass (COM) was computed using the formula [250–252]:

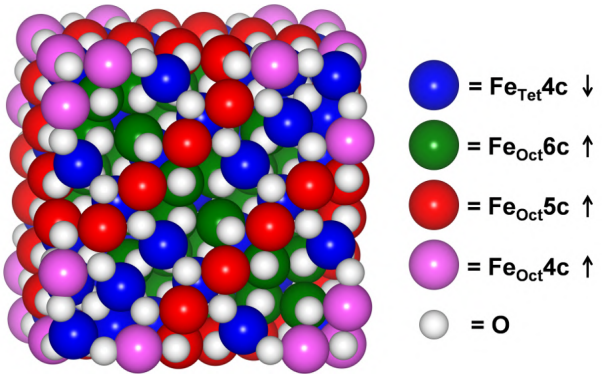

Figure 3.1: Schematic representation of the Fe_3O_4 cubic NP model used in this study. The color coding of the atoms is given in the legend on the right. Labels 4c–6c indicate the actual coordination number of the corresponding ions.

$$band\ COM = \frac{\int_{-\infty}^{E_F} E\rho(E)dE}{\int_{-\infty}^{E_F} \rho(E)dE} \tag{3.5}$$

where E is the energy, E_F the Fermi energy (which is set to 0), and $\rho(E)$ the electronic density of states.

3.3 Results and discussion

The cubic model used in this study (shown in Figure 3.1) is enclosed by six (001) facets, as observed in many experiments [92, 93], it is made of 57.7 $Fe_3O_{4.4}$ units (173 Fe and 256 O, with a slight excess of O), and, in agreement with a previous simulated annealing molecular dynamics study by my group [125], it presents four reconstructed vertexes and is characterized by an outer-shell layer containing only Fe^{III} ions and a core where Fe^{II}/Fe^{III} ions alternate. In the ground state of the NP, in perfect agreement with what happens in bulk magnetite, the unpaired d electrons at the Fe_{Oct} sites are antiferromagnetically coupled with the ones at the Fe_{Tet} sites. Accordingly, the total magnetic moment can be obtained from the general formula in Equation (3.1), as derived previously by my group [125]. Analogously to bulk magnetite, for Fe^{III}_{Oct} and Fe^{III}_{Tet} the high-spin $3d^5$ configuration gives an atomic magnetic moment of +5 and -5 μ_B, respectively; for Fe^{II}_{Oct} and Fe^{II}_{Tet} the high-spin $3d^6$ electron configuration gives +4 and -4 μ_B, respectively. The total magnetic moment m_{tot} for the cubic NP under investigation is 288 μ_B.

Spin-disorder phenomena may reduce this optimal magnetic moment and can be simulated by forcing the spin-flipping of the $3d$ electrons (see Figure 3.2) at some chosen iron centers in the NP [249]. In particular, we modeled the spin-flip at

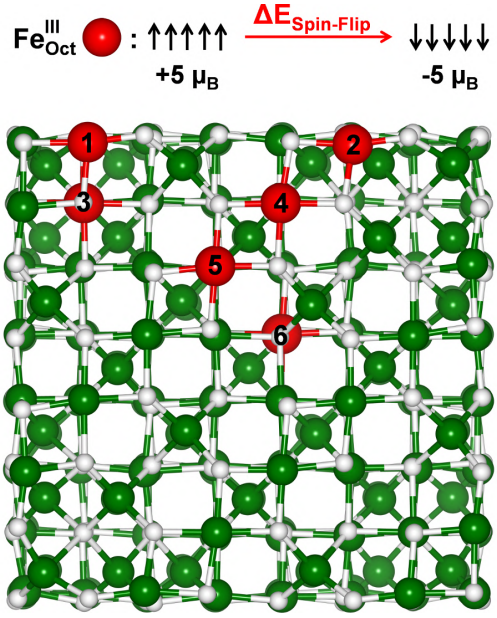

Figure 3.2: Schematic representation of the spin-flip mechanism (top) and global minimum structure of the Fe_3O_4 cubic NP (bottom). The white, green, and red beads represent O, Fe, and Fe^{III}_{Oct} on which the spin-flip cost is evaluated, respectively.

various octahedral Fe sites inverting the magnetic order of the $3d^5$ electrons from spin up to spin down (see Figure 3.2 and Table 3.1). These electrons are no more spin-aligned with those of the other Fe_{Oct} sites in the NP, but they are aligned with the $3d$ electrons at the Fe_{Tet} sites. The spin-flip of all the d electrons of one Fe^{III}_{Oct} ion is certainly expected to be unfavorable in bulk magnetite, and indeed we computed an energy cost of +0.42/+0.67 eV ($\Delta E_{Spin-Flip}$ values at the bottom of Table 3.1) when the electrons of one Fe^{III}_{Oct} ion are flipped in a Fe_3O_4 bulk cell of increasing size (2, 8 or 16 Fe_3O_4 units). The increasing energy cost associated to a lower density of the *spin-defect* suggests that the larger the number of Fe_{Oct} and Fe_{Tet} ions involved in the ferromagnetic and antiferromagnetic interactions, respectively, the larger the overall stabilization. We expect that a positive trend for increasing supercell sizes, which, however, are computationally too costly. Now, the question is: what happens if we evaluate the same spin-flip on Fe^{III}_{Oct} sites at the NP surface? Considering that surface spin canting is often observed in experiments, one would expect that the energy cost for spin-flipping might drop.

Indeed, we observe a reduction of the computed energy cost to spin-flip $3d^5$ electrons at some specific Fe^{III}_{Oct} ions in the surface layers, especially when we allowed for a full atomic relaxation of the NP. In particular, this is true for those Fe_{Oct} ions that are characterized by a larger deficiency of Fe_{Tet} ions in the next coordination sphere of the spin-flipped ion, such as $Fe^{III}_{Oct}4c-$(**1**), $Fe^{III}_{Oct}6c-$(**3**)

Table 3.1: Selected Fe^{III}_{Oct} sites in the cubic NP (site numbering in bold from Figure 3.2) and in bulk magnetite considered for the spin-flip mechanism investigation. Relevant information of the surrounding coordination, stoichiometry, and energetics (in meV) are reported.

Fe label	Nearby Fe ions (Fe_{Oct};Fe_{Tet})	Fe_3O_{4+x} units	ΔE_{SF+Rel} ($\Delta E_{Spin-Flip}$)
$Fe^{III}_{Oct}4c-$(**1**)	3;1	57.7	+174 (+252)
$Fe^{III}_{Oct}4c-$(**2**)	2;3	57.7	+438 (+623)
$Fe^{III}_{Oct}6c-$(**3**)	6;3	57.7	+13 (+270)
$Fe^{III}_{Oct}5c-$(**4**)	3;4	57.7	+337 (+425)
$Fe^{III}_{Oct}5c-$(**5**)	4;3	57.7	+137 (+208)
$Fe^{III}_{Oct}6c-$(**6**)	6;6	57.7	+334 (+406)
$Fe^{III}_{Oct}6c-bulk$	6;6	2	+420 (+420)
$Fe^{III}_{Oct}6c-bulk$	6;6	8	+420 (+420)
$Fe^{III}_{Oct}6c-bulk$	6;6	16	+420 (+420)

Table 3.2: Selected Fe^{III}_{Oct} sites in the cubic NP (site numbering in bold from Figure 3.2) considered for the spin-flip mechanism investigation at different acetic acid (AA) coverage. ΔE_{SF+Rel} and $\Delta E_{Spin-Flip}$ are reported in meV.

No. AA	NP coverage	No. spin-flipped $Fe^{III}_{Oct}6c-$(**3**)	ΔE_{SF+Rel} ($\Delta E_{Spin-Flip}$)
0	Naked	1	+13 (+270)
0	Naked	4	+45 (+228)
1	Local low	1	-49 (+80)
4	Low	4	-188 (-42)
3	Local high	1	+141 (+165)
48	Full	1	+97 (+111)
48	Full	4	+405 (+448)
No. AA	NP coverage	No. spin-flipped $Fe^{III}_{Oct}5c-$(**5**)	ΔE_{SF+Rel} ($\Delta E_{Spin-Flip}$)
0	Naked	1	+137 (+208)
48	Full	1	+280 (+310)

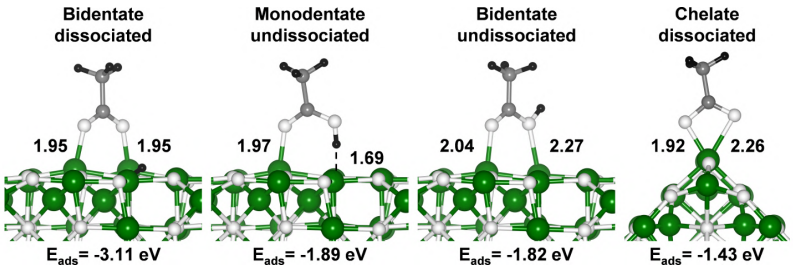

Figure 3.3: Ball and stick representation of the Fe_3O_4 cubic NP with an AA molecule adsorbed on it in different configurations: dissociated bidentate, undissociated monodentate and H-bonded, undissociated bidentate, and dissociated chelate. The black, grey, white, and green beads represent H, C, O, and Fe, respectively. H-bonds are indicated by dashed black lines. The Fe-O_{AA} bond length (in Å) and the adsorption energy E_{Ads} (in eV) calculated at DFTB+U level are given for each configuration.

and $Fe^{III}_{Oct}5c-(\mathbf{5})$ sites. The energy cost at $Fe^{III}_{Oct}6c-(\mathbf{3})$ sites drops down to +13 meV, which means that the spin up and the spin down configurations for these Fe^{III}_{Oct} ions are almost isoenergetic, which indicates an easiness to spin-disorder. For $Fe^{III}_{Oct}4c-(\mathbf{1})$ and $Fe^{III}_{Oct}5c-(\mathbf{5})$ sites the energy drops to +174 and +137 meV, respectively. On the contrary, more bulk like sites or sites whose coordination spheres involve a larger number of Fe_{Tet} than of Fe_{Oct}, the energy cost for spin-flip at Fe^{III}_{Oct} ions remains high, as much as +438, +337 and +334 meV for $Fe^{III}_{Oct}4c-(\mathbf{2})$, $Fe^{III}_{Oct}5c-(\mathbf{4})$ and $Fe^{III}_{Oct}6c-(\mathbf{6})$ sites, respectively. We rationalize this with a stronger superexchange antiferromagnetic interaction with the surrounding Fe_{Tet}. Moreover, when forcing all $Fe^{III}_{Oct}5c-(\mathbf{5})$ ions in the NP (four) to spin-flip, we calculated an energy cost ΔE_{SF+Rel} of +45 meV, which means that the overall cost of each spin-flip is almost exactly additive (+13 meV · 4), see Table 3.2.

The next step in the study is to investigate the effect of organic acids adsorption on the surface to find an atomistic-level explanation of the reduced spin disorder observed in coated magnetite nanoparticles, with saturation magnetization values close to those of bulk samples. To this aim, acetic acid (AA) was adsorbed on the NP surface, starting with one isolated molecule and considering different adsorption modes [253], as shown in the ball-and-stick representations in Figure 3.3. We considered dissociated bidentate, undissociated monodentate and H-bonded, undissociated bidentate acetic acid on two five-fold coordinated Fe_{Oct} sites on one (001) facet of the NP model and dissociated chelate acetic acid at a four-fold coordinated Fe_{Oct} site on one edge of the NP model. The largest adsorption energy, according to the DFTB+U calculations, is obtained for the dissociated bidentate mode (−3.11 eV), which is more than 1 eV larger than that for the other adsorption modes considered. In the cases where acetic acid molecules dissociate, the released protons are adsorbed on superficial O ions that are not directly bound to

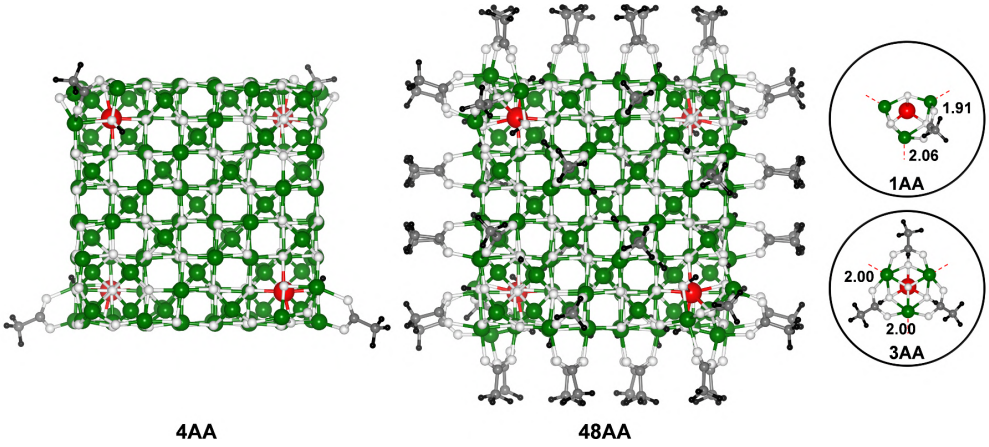

Figure 3.4: Ball and stick representation of the Fe_3O_4 cubic NP at different AA coverage: low coverage (4AA), full coverage (48AA), local low coverage (1AA), and local high coverage (3AA). For the local coverages (1AA and 3AA), only the ligands and NP O-corner are shown for clarity. The red dashed lines indicate the edges of the hidden NP. The Fe-O_{AA} bond length (in Å) for the asymmetric unit are shown. The black, grey, white, green, and red beads represent H, C, O, Fe, and Fe^{III}_{Oct} on which the spin-flip cost is evaluated, respectively.

a Fe_{Tet} ion, since these O sites have been previously determined to be more reactive as proton acceptor or basic sites [254–256]. Because the dissociated bidentate mode is energetically favoured, it was considered for the whole study as the unique binding mode of the coating acetic acid molecules.

Because the cost for spin-flipping one $Fe^{III}_{Oct}6c-$(**3**) ion was found to be very low (only +13 meV), this site was chosen for the investigation of the effect of acetic acid adsorption (see Figure 3.4) on the spin-flip process to understand the mechanism of how the coating molecules can actually affect the energetic of spin canting. To this aim, one isolated acetic acid molecule is adsorbed at one corner of the NP, in particular on two Fe_{Oct} sites directly bound the O ion at the corner. Because there are four corners of this type in the NP, acetic acid molecules were put also on the other three corners. Both situations (1AA and 4AA) are considered as a low coverage regimes (local low and low, respectively). The adsorption energy is -2.98 eV in 1AA and -3.23 eV per acetic acid molecule in 4AA. It is important to notice that the corner site underwent a reconstruction with the O site moving away from the corner, breaking one of its bonds with one of the three Fe_{Oct} ions and resulting to be a bridging O at one side of the corner. At local low coverage (1AA), the spin-flip process costs +80 meV, but allowing for atomic relaxation in the new spin configuration, there is an energy gain of -129 meV, which reverses the sign of the overall energy release leading to an energy gain (ΔE_{SF+Rel}) of -49 meV. Considering the low coverage (4AA) model, the overall effect of spin-

flipping the four equivalent $Fe^{III}_{Oct}6c-$(**3**) ions is almost exactly additive since the ΔE_{SF+Rel} is now -188 meV, which is almost exactly four times what computed for 1AA (-49 meV), indicating that the spin-flip process involves a single Fe ion and is independent from other Fe ions. These results suggest that spin disorder phenomena, which are already strongly favored at the surface of NPs, can be actually further promoted in the presence of low density of coating molecules at defects sites.

A further point related to the acetic acid adsorption is whether or not there is a coverage effect. To answer this, we investigated a fully decorated NP (full coverage regime), where all the under-coordinated Fe_{Oct} ions on the facets, edges and corners are saturated by adsorbing forty-eight bidentate dissociated acetic acid molecules (48AA, as shown in Figure 3.4). The average adsorption energy per acetic acid molecule is -1.96 eV. It is noteworthy that at a full coverage, we observe a reduction of the atomic reconstruction only at corner sites, where the exposed O ion keeps its three bonds with the nearby Fe_{Oct} ions. Besides that, the atomic rearrangements are rather limited as we can infer from the comparison of the simulated EXAFS spectra for naked and fully decorated Fe_3O_4 NP in Figure 3.5. A simulated annealing calculation was also performed at the DFTB+U level of theory (up to 500 K; see Section 3.2 for more information) and then cooled down the system again to allow for atomic rearrangement that might have some activation barrier, however no such events were observed. Then, we investigated the spin-flip processes for this fully decorated NP model. We considered two types of octahedral Fe sites, $Fe^{III}_{Oct}6c-$(**3**) and $Fe^{III}_{Oct}5c-$(**5**), because the first is near a corner site and is the one with a negligible energy cost for spin-flipping (+13 meV per site) in the naked NP, whereas the second is on the flat facet, far from the corner, but still is characterized by a quite low energy cost for spin-flipping (+137 meV) in the naked NP. As opposed to the naked and local low coverage (1AA) situations, in the presence of a full monolayer of acetic acid molecules, we observe that the spin-flip of both the octahedral Fe sites considered becomes unfavourable. In the case of $Fe^{III}_{Oct}5c-$(**5**) site, the energy change for the full process (ΔE_{SF+Rel}) in the naked NP is +137 meV, whereas at full coverage (48AA) it becomes +280 meV. In the case of $Fe^{III}_{Oct}6c-$(**3**) site, the ΔE_{SF+Rel} in the naked NP is +13 meV, at local low coverage (1AA) is -49 meV, whereas at full coverage (48AA) it becomes +97 meV. Considering this process at full coverage for all the four structurally equivalent $Fe^{III}_{Oct}6c-$(**3**), we observe that the overall effect is additive since the ΔE_{SF+Rel} became +405 meV, which is four times what computed for one Fe ion (+97 meV). This result, as well as that at low coverage, indicates that the spin-flip process involves a single Fe ion and is independent from other Fe ions, with no long-range effects. In order to verify that the coverage effect is local, three acetic acid molecules were adsorbed at one NP corner close to the $Fe^{III}_{Oct}6c-$(**3**) site,

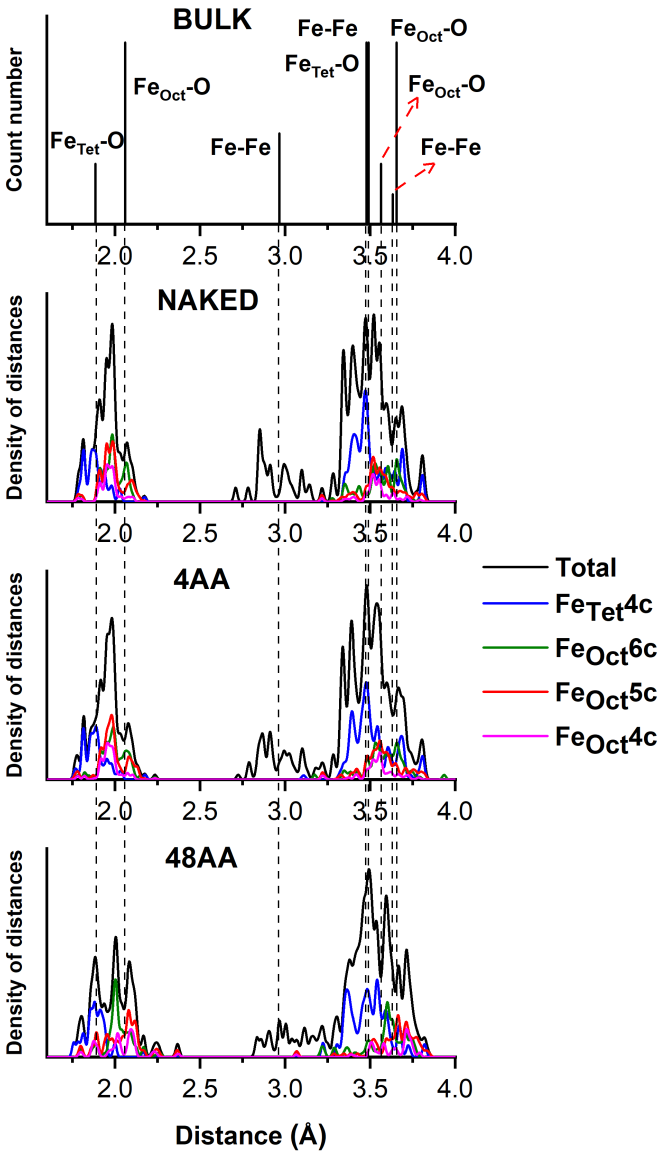

Figure 3.5: Simulated extended X-ray adsorption fine structure (EXAFS) spectra for Fe_3O_4 bulk (top panel) and Fe_3O_4 NP at different AA coverage (bottom panels): in vacuum (NAKED), at low coverage (4AA), and at full coverage (48AA).

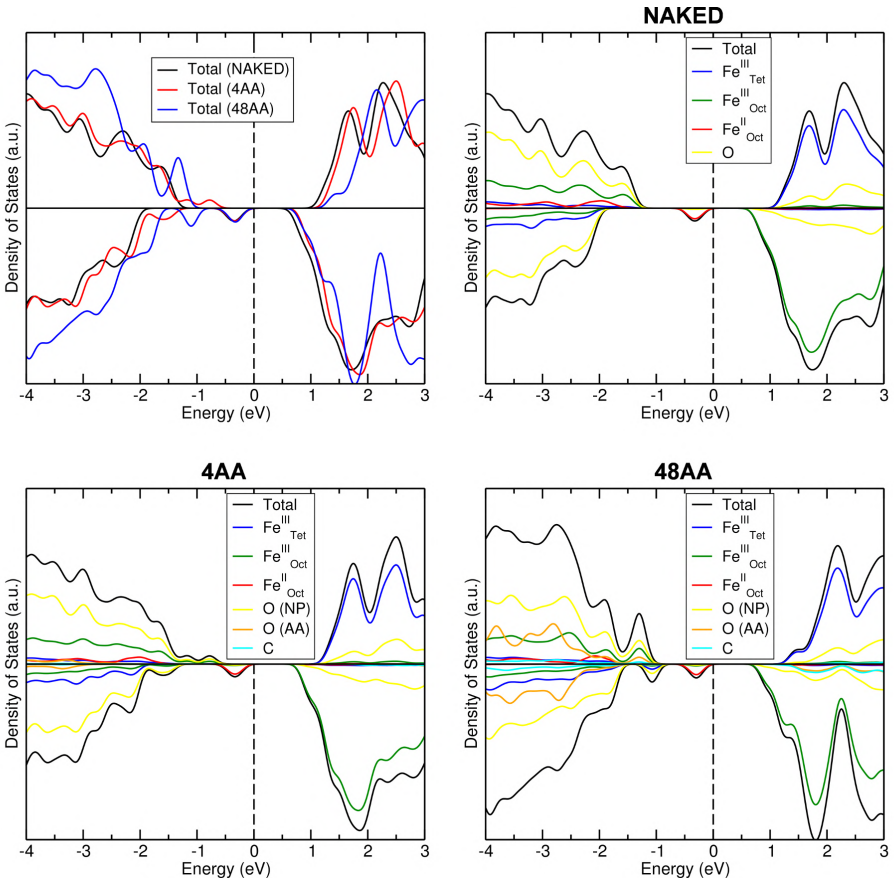

Figure 3.6: Total and projected DOS of the Fe_3O_4 NP at different AA coverage: in vacuum (NAKED), at low coverage (4AA), and at full coverage (48AA). In the top-left panel the total DOS of all these systems are direclty compared. The Fermi level is scaled to zero as indicated by the dashed black lines.

leading to the so-called local high coverage regime (Figure 3.4, 3AA). Similarly to what was observed at full coverage, an enhancement of the ΔE_{SF+Rel} value (+141 meV) was observed for the spin-flip of the $Fe^{III}_{Oct}6c-$(**3**) site with respect to the small one for the naked NP (+13 meV), confirming that the effect of the coverage is rather local.

Now, we must provide an explanation why a full coverage adsorption of organic acids affects the spin-flip processes at $Fe^{III}_{Oct}6c-$(**3**) sites in the surface layers and why it makes them unfavorable, similarly to what happens in bulk-like sites. The rationalization by Salafranca et al. [120] is based on different electronic structure properties of bare and functionalized magnetite surfaces, as already discussed in Section 3.1. However, their findings are in contrast with the other existing studies in the literature: the unreconstructed bare (001) surface shows a semiconductor

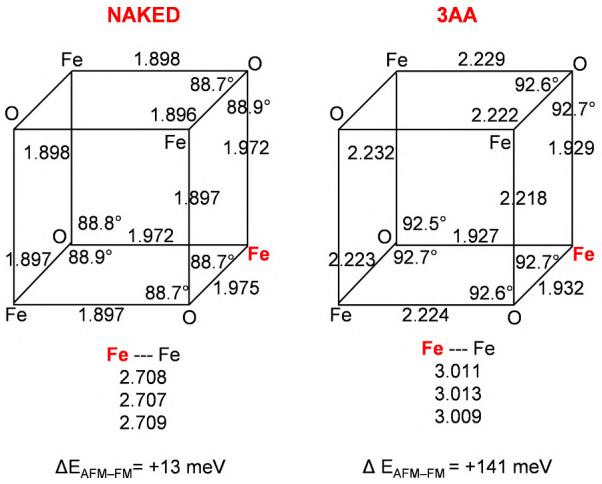

Figure 3.7: Structural (distances in Å and angles in degrees) and energetical (ΔE_{AFM-FM} in meV) parameter for the corner of the naked NP (NAKED) and NP at local high coverage (3AA). The Fe ion in red is the one called $Fe^{III}_{Oct}6c$ – (**3**)) in the text, while the black Fe ions are superficial Fe_{Oct} that interact with the capping molecules.

[46, 70, 76, 86, 123, 124] and not metallic [120] behavior. Here, the total and projected *density of states* (DOS) were computed and reported in Figure 3.6 for the naked and the functionalized NP. In all cases the NP presents a gap at Fermi level. Another simple reason, which is often invoked, is that the presence of a full coating layer during the synthesis enhances the crystallinity of the NPs. To give ground to this statement, the EXAFS spectra (see Figure 3.5) of the naked and fully coated NP were simulated by calculating the density of distances for each Fe ions with other (Fe or O) ions and projecting them on octahedral and tetrahedral Fe ions with O. In general, the range of Fe_{Tet}-O and Fe_{Oct}-O bond lengths is broadened in the case of NPs with respect to bulk magnetite because of the structural distortions and low coordination near the surface. The broader the peaks, the worse the crystallinity of the nanoparticles. From these spectra, no evidence of improved crystallinity for the coated cubic NP model proposed in the present study can be highlighted. Indeed, only small deformations are present both in the naked and in the fully coated NPs. Moreover, these deformations in the Fe−O and Fe—Fe distances or Fe−O−Fe angles do not correlate with the observation of superexchange in the models (see Figure 3.7). The Fe−O−Fe angles are in all cases close to 90°. In particular, for the system capped with acetic acid the angles are slightly larger than for the naked, which is an opposite trend with respect to the ΔE_{AFM-FM} (i.e., ΔE_{SF+Rel}), because larger angles are expected to stabilize the AFM configuration, not the FM one [4, 5, 257]. Regarding the Fe−O and Fe—Fe distances, they are longer in the NP capped with acetic acid than in

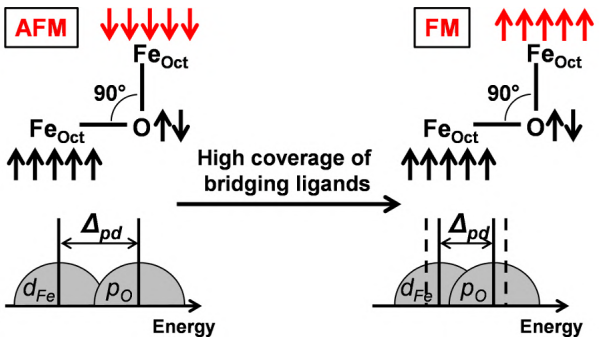

Figure 3.8: Schematic representation of the extra FM superexchange interaction between octahedral Fe ions induce by adsorbed bridging ligands.

the naked, again in opposite trend with what expected for a more efficient hopping which could favour the FM superexchange.

Therefore, we must find another reason why the presence of high density of adsorbed acetic acid affects the magnetic properties of the NPs. We propose that the reason is related to an induced extra superexchange FM effect among Fe_{Oct} sites in the surface layers, which counteracts the surface spin canting processes. Indeed, it is well recognized in the literature that carboxylate ligands bridging dinuclear transition metal ions mediate superexchange coupling [258–260]. Similarly, bridging carboxylate groups from the acetic acid molecules on the NP surface could create additional paths for the FM superexchange between Fe_{Oct} ions. In order to understand the origin of this extra ferromagnetic superexchange, the variation of the O p energy levels with respect to the Fe d ones was analyzed since this difference (Δ_{pd}) is inversely proportional to the magnetic exchange coupling constant (J), according to Equation (3.6):

$$J \propto \frac{2t_{pd}^4}{(U_d + \Delta_{pd})^2} \tag{3.6}$$

where t_{pd} is hopping integral between p and d orbitals, U_d is the Coulomb repulsion between two electrons in a d orbital, and the charge transfer energy Δ_{pd} is the energy difference between O^{-II} p states eigenvalues and Fe^{III}_{Oct} d states eigenvalues, respectively. In this work, the Δ_{pd} for the NP systems is estimated with the energy difference between the center of mass (COM) of the O^{-II} p-band and of the Fe^{III}_{Oct} d-band, as detailed in the Section 3.2. A Δ_{pd} value of 2.18 eV for the naked NP and of 1.98 eV for the fully coated NP was obtained. According to the Equation (3.6), a reduction of Δ_{pd} (by 0.2 eV) is expected to enhance the magnetic exchange coupling constant (as schematized in Figure 3.8), in perfect agreement with the stronger FM superexchange interaction correlated to the higher spin-flip energy cost observed in our calculations for the fully coated NP.

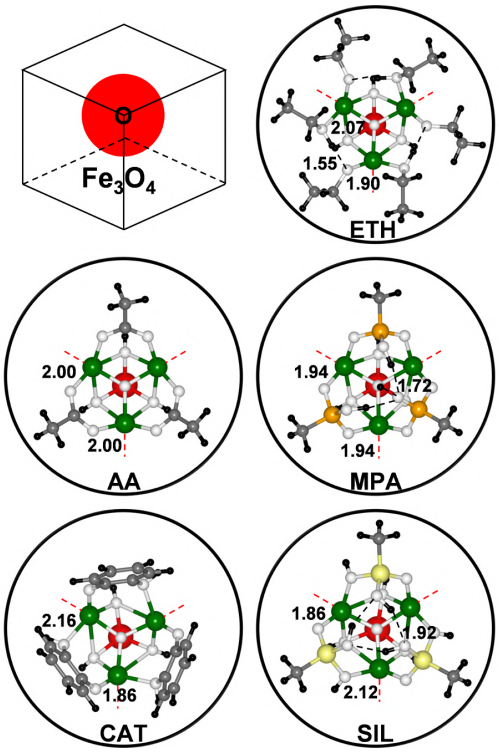

Figure 3.9: Ball-and-stick representations for the adsorption of different ligands at local high coverage onto the NP corner. Only the ligands and the NP O-corner are shown for clarity, as schematized in top left corner of the figure. The red dashed lines indicate the edges of the hidden NP. The black dashed lines indicate the formation of hydrogen bonds. The H-bond and the Fe-O_{Ligand} bond lengths (in Å) for the asymmetric unit are shown. The black, grey, orange, yellow, white, green, and red beads represent H, C, P, Si, O, Fe, and Fe^{III}_{Oct} on which the spin-flip process is investigated, respectively.

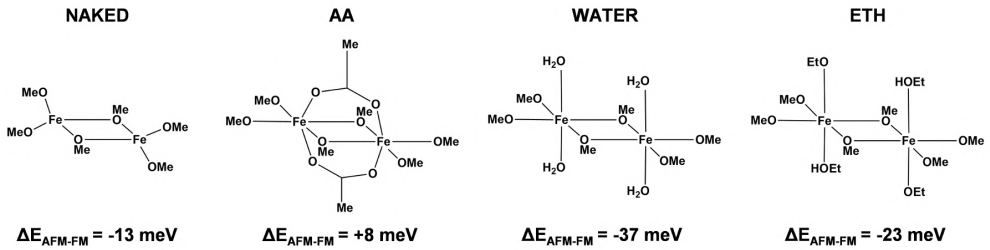

Figure 3.10: Schematic representation of the Fe(III) metoxide dimer in vacuum (NAKED), with two adsorbed acetic acid molecules (AA), with four adsorbed water molecules (WATER), and with four adsorbed ethanol molecules (ETH). The calculated ΔE_{AFM-FM} is given for each model.

To investigate the different behaviour of a monodentate ligand (i.e., ethanol) with respect to what obtained for a bidentate bridging ligand (i.e., acetic acid) on the NP, six ethanol molecules were adsorbed on the NP corner (Figure 3.9, ETH), leading to the so-called local high coverage, in perfect analogy to what done for acetic acid. Three of these ethanol molecules were found to spontaneously dissociate forming H-bonded dimers (similarly to what observed for water on $Fe_3O_4(001)$ surface [70, 84, 245, 261]) with dissociated protons adsorbing on the same superficial O sites as those involved in the acetic acid dissociation. In the case of ethanol, a small negative ΔE_{SF+Rel} value of -15 meV was computed, which confirms that the spin-flip process is slightly favoured. This result is in contrast with what observed for acetic acid with a ΔE_{SF+Rel} value of +141 meV. Therefore, these calculations prove that an induced extra superexchange FM effect among Fe_{Oct} sites in the surface layers is only triggered by adsorption of bridging molecules that electronically connect different Fe_{Oct} sites, such as acetate, but not of monocoordinating molecules, such as ethanol.

The effect of bridging ligands on the magnetic properties of Fe ions was also tested on a toy model, i.e. the Fe^{III} metoxide dimer, which is a simplified system of the Fe^{III} tert-butoxide dimer (Figure 3.10, NAKED). For this dinuclear Fe^{III} complex the FM and the AFM configurations were computed (see Section 3.2 for additional details). Then, we have evaluated how the presence of two additional carboxylate bridges (Figure 3.10, AA) or of four additional water/ethanol molecules (Figure 3.10, WATER and ETH, respectively) affects the relative stability AFM-FM. In line with our prediction, the presence of additional bridging carboxylate stabilizes the FM solution, whereas the water and the ethanol molecules favour the AFM one.

As a further step, the effect of other bridging anchoring ligands was investigated, to strengthen the conclusion that only bidentate molecules are able to create chemical bridges between Fe_{Oct} sites for an additional ferromagnetic superexchange

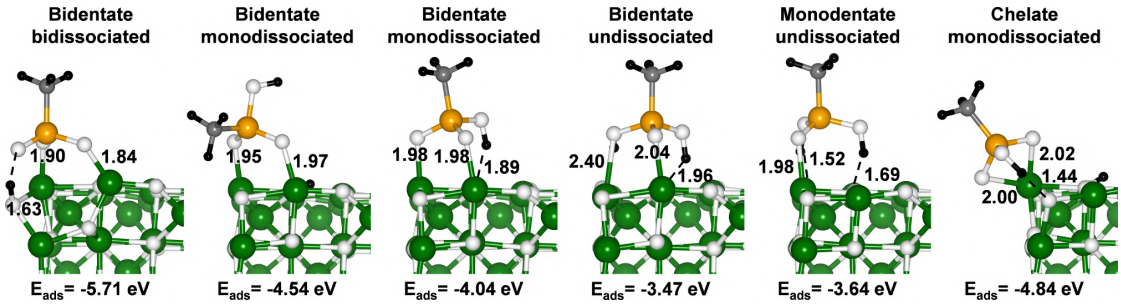

Figure 3.11: Ball-and-stick representations of the Fe_3O_4 cubic NP with a methylphosphonic acid (MPA) molecule adsorbed on its corner in different (stable) configurations. The black, gray, orange, white, and green beads represent H, C, P, O, and Fe, respectively. H-bonds are indicated by dashed black lines. The H-bonds and Fe-O_{MPA} bonds length (in Å) and the adsorption energy E_{Ads} (in eV) are shown.

Table 3.3: Adsorption energy E_{Ads} (in eV per molecule) for different ligands at different coverages onto the Fe_3O_4 NP.

Coverage	AA	MPA	CAT	SIL	ETH
Local low ($Fe^{III}_{Oct}6c-$(**3**))	−2.98	−5.71	−3.91	−4.62	−2.32
Local high ($Fe^{III}_{Oct}6c-$(**3**))	−3.00	−3.85	−2.66	−3.00	−1.60
Local high ($Fe^{III}_{Oct}5c-$(**5**))	−2.44	−3.66	−2.55	−2.92	−1.57

interaction, which is an effective mechanism hampering the reduction (due to spin canting) of the NP magnetization. To this aim, only local (low and high) coverages were considered for simplicity, since it has been already demonstrated above that the coverage effect is rather local.

The screening of various bridging anchoring ligands started from phosphonic acid. In particular, methylphosphonic acid (MPA) was considered, as the simplest prototypical molecule, in several adsorption modes (see Figure 3.11): undissociated monodentate, dissociated chelate, undissociated bidentate, dissociated bidentate and bidissociated bidentate. The most stable configuration at the O-corner, in the low coverage regime, is the bidissociated bidentate, with an adsorption energy of −5.71 eV (see Figure 3.11, Figure 3.12, and Table 3.3), which is at least 1 eV larger than those computed for the other modes. Note that one of the two dissociated protons goes on the extremely reactive O atom at the O-corner, causing some Fe−O bond breaking and corner reconstruction, whereas the other is adsorbed on an O atom of the flat surface that is generally recognized in the literature as the most ease to be protonated [254–256]. If the local density of MPA molecules at the O-corner is increased, in the proximity of the $Fe^{III}_{Oct}6c-$(**3**) site (Figure 3.9, MPA), using the three undercoordinated octahedral Fe ions around the O at

Table 3.4: Selected Fe^{III}_{Oct} sites considered for the spin-flip mechanism investigation. The ΔE_{SF+Rel} and $\Delta E_{Spin-Flip}$ (inside the parenthesis) values are reported in meV for different ligands at different coverages onto the Fe_3O_4 NP.

Site	Coverage	AA	MPA	CAT	SIL	ETH
$Fe^{III}_{Oct}6c-$(**3**)	Naked			+13 (+270)		
	Local low	−49 (+80)	−10 (+16)	−27 (+4)	−33 (−1)	−39 (−8)
	Local high	+141 (+165)	+120 (+130)	+118 (+131)	+134 (+143)	−15 (+15)
$Fe^{III}_{Oct}5c-$(**5**)	Naked			+137 (+208)		
	Local high	+280 (+310)	+241 (+275)	+219 (+257)	+209 (+248)	+114 (+210)

the vertex, the additional two MPA molecule are found to preferentially adsorb as monodissociated bidentate, which is one of the most common adsorption modes on metal oxide surfaces [262]. The presence of the other two MPA molecules prevents the Fe-O bond breaking at the O-corner upon OH formation. MPA adsorption on flat 001 facets around the $Fe^{III}_{Oct}5c-$(**5**) site was considered with two MPA molecules (Figure 3.13, MPA) in the dissociated bidentate mode (-3.66 eV per molecule). The spin-flipping accompanied by atomic relaxation at $Fe^{III}_{Oct}6c-$(**3**) and $Fe^{III}_{Oct}5c-$(**5**) sites, when local high coverage of MPA is reached, is clearly much less favourable than for the naked NP, similarly to what observed in the presence of high density of AA: +120 and +241 meV for the two sites, respectively, vs +141 and +280 meV for AA (see Table 3.4). Therefore, the bridging ligand MPA [O−P−O], similarly to AA [O−C−O], is perfectly capable of activating additional superexchange interaction among Fe_{Oct} ions.

Next, catechol-based ligands, which are well-known to stably anchor metal oxide surfaces, were considered. Catechol (CAT) is a bridging ligand [O−C−C−O] that can bidentate two surface cations. Indeed, the monodissociated bidentate adsorption mode is found to be that with the largest adsorption energy (-3.91 eV) at the O-corner site (see Table 3.3, Figure 3.12, and Figure 3.14), if compared to undissociated bidentate, bidissociated bidentate, undissociated chelate, dissociated chelate and bidissociated chelate, which are at least 1 eV higher in energy if not unstable. When three CAT molecules are anchored to the O-corner by using the three octahedral Fe ions around the O at the vertex, a highly symmetric structure is observed, as shown in Figure 3.9. On the flat 001 facets, catechol molecules are similarly monodissociated and bidentate as on the corner sites (Figure 3.13). It is not so easily predictable whether the [O-C-C-O] bridge will be effective in inducing magnetic communication between Fe ions. The results confirm that in the presence of high coverage of CAT ligands, spin flipping, even accompanied by atomic relaxation, is a hampered process by +118 meV at the $Fe^{III}_{Oct}6c-$(**3**) site and by 219 meV at the $Fe^{III}_{Oct}5c-$(**5**) site. These numbers are slightly smaller than for AA and MPA but are still very close (see Table 3.4).

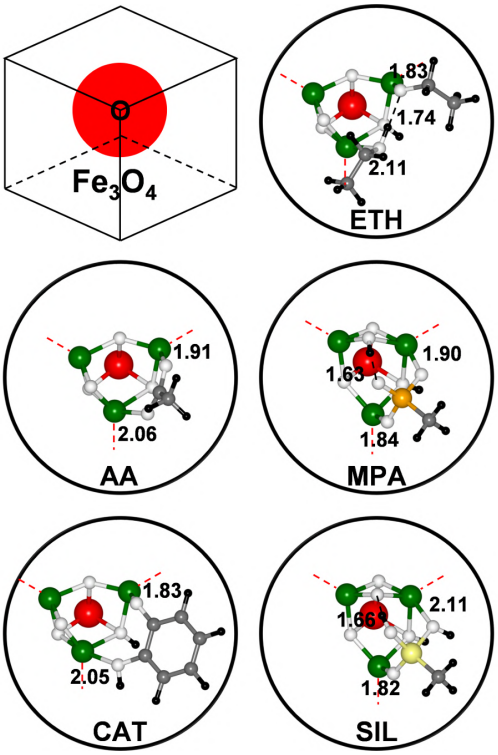

Figure 3.12: Ball-and-stick representations for the most stable adsorption mode of different ligands at local low coverage onto the NP corner. Only the ligands and the NP O-corner are shown for clarity, as schematized in top left corner of the figure. The red dashed lines indicate the edges of the hidden NP. The black dashed lines indicate the formation of hydrogen bonds. The H-bonds and Fe-O_{Ligand} bonds length (in Å) are shown. The black, gray, orange, yellow, white, green, and red beads represent H, C, P, Si, O, Fe, and Fe^{III}_{Oct} on which the spin-flip process is investigated, respectively.

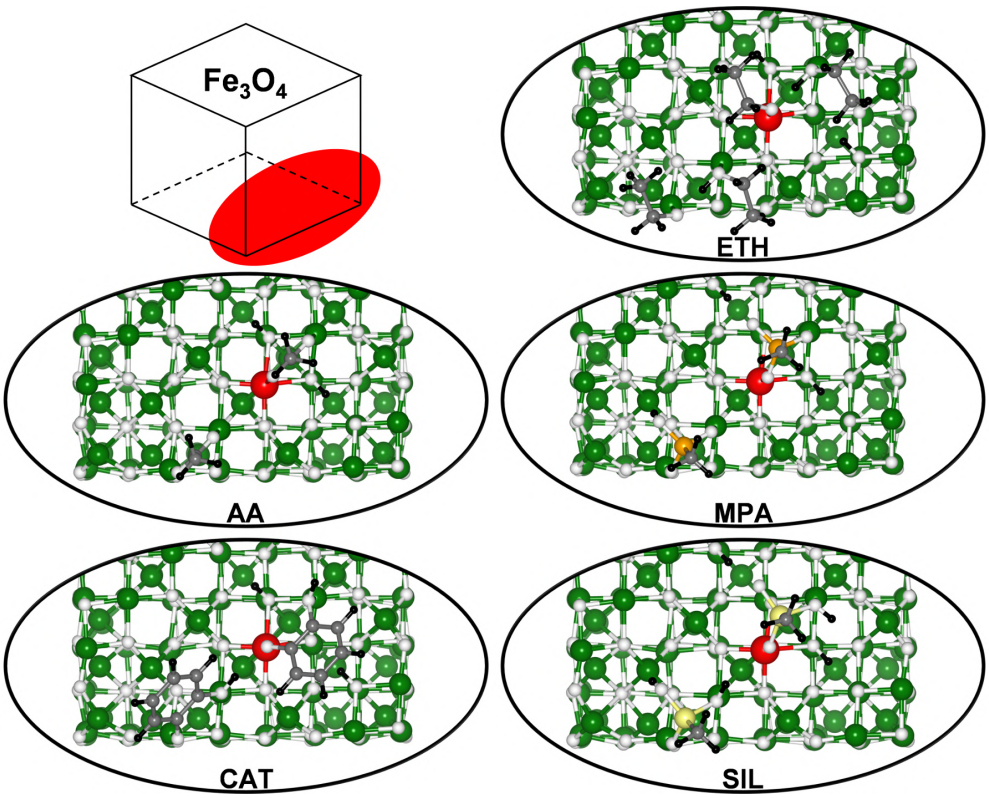

Figure 3.13: Ball-and-stick representations for the adsorption of different ligands at local high coverage onto the nanoparticle surface. Only the ligands and the NP surface portion around $Fe^{III}_{Oct}5c-$(**5**) are shown for clarity, as schematized in top left corner of the figure. The black, gray, orange, yellow, white, green, and red beads represent H, C, P, Si, O, Fe, and Fe^{III}_{Oct} on which the spin-flip process is investigated, respectively.

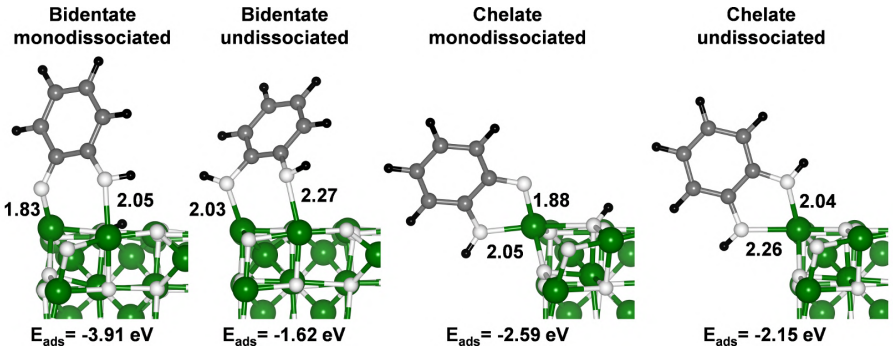

Figure 3.14: Ball and stick representations of the Fe_3O_4 cubic NP with a catechol (CAT) molecule adsorbed on its corner in different (stable) configurations. The black, gray, white, and green beads represent H, C, O, and Fe, respectively. The Fe-O_{CAT} bonds length (in Å) and the adsorption energy E_{Ads} (in eV) are shown.

The last class of anchoring ligand which was investigated is based on a silanetriol group. In particular, methylsilanetriol (SIL), consisting of three [O−Si−O] bridges, was considered. Similarly to MPA, this ligand could potentially tridentate, however it is found to bidentate because the (001) magnetite surface presents superficial Fe rows that are too distant to allow the tridentation. Here, it can be observed that at the O-corner SIL is preferentially monodissociated and bidentate on two undercoodinated octahedral Fe ions next to the O at the vertex (see Figure 3.15), both at low (-4.62 eV) and high (-3.00 eV) coverage densities (Figure 3.12 and Figure 3.9, respectively). We considered other absorption modes, which are at least half an eV higher in energy: undissociated bidentate, bidissociated bidentate and dissociated chelate. Are the [O−Si−O] bridges effective for superexchange interaction among octahedral Fe ions? The answer is again positive with an energy cost for spin-flipping, even allowing atomic relaxation, of +134 meV at the $Fe^{III}_{Oct}6c-$(**3**) site and by 209 meV at the $Fe^{III}_{Oct}5c-$(**5**) site, in line with the other bridging anchoring ligands considered in this study (see Table 3.4 for direct comparison).

These calculations clearly suggest that all bidentate bridging ligands induce an extra FM superexchange interaction between octahedral Fe ions, which reinforces the overall magnetization of the NPs and supresses spin disorder phenomena. This effect has been evaluated in terms of energy cost (ΔE_{SF+Rel}) to induce spin-flip and corresponding atomic relaxation on an octahedral Fe ion in the proximity of the O-corner, where spin and structural reorganization can more easily take place, and on the flat 001 facet. Larger values of ΔE_{SF+Rel} reflect larger magnetic exchange coupling constants J between octahedral Fe ions. Again, the dependency of J with the difference between the O^{-II} p-band and the Fe^{III}_{Oct} d-band energy levels (i.e., the Δ_{pd}) was analyzed, according to Equation (3.6). Since a local high coverage of

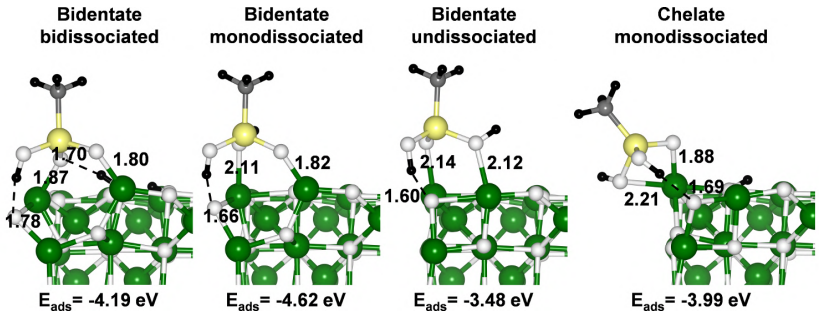

Figure 3.15: Ball and stick representations of the Fe_3O_4 cubic NP with a methylsilanetriol (SIL) molecule adsorbed on its corner in different (stable) configurations. The black, gray, yellow, white, and green beads represent H, C, Si, O, and Fe, respectively. H-bonds are indicated by dashed black lines. The H-bonds and Fe-O_{SIL} bonds length (in Å) and the adsorption energy E_{Ads} (in eV) are shown.

ligands was simulated at the O-corner, only the spin-flipping Fe site, $Fe^{III}_{Oct}6c-$(**3**), and the O and Fe ions in its first and second coordination sphere are considered in the calculation of the O^{-II} p-band and Fe^{III}_{Oct} d-band COM. A Δ_{pd} of 2.05 eV was computed for the naked NP and of 1.55 eV, 1.49 eV, 1.54 eV, and 1.60 eV for the NP at high coverage of AA, MPA, CAT, and SIL, respectively. According to the Equation (3.6), a reduction of Δ_{pd} (here of about 0.5 eV) is expected to enhance the magnetic exchange coupling constant, in perfect agreement with the increase in spin-flip energy cost observed in our calculations, as schematized in Figure 3.8. This analysis is corroborated also by the opposite case of a local high coverage of ETH, for which a Δ_{pd} value very close to that for the naked NP (1.98 eV vs 2.05 eV, respectively) was computed, confirming no additional FM exchange, as suggested by the ΔE_{SF+Rel} value (-15 meV) in favor of spin-flipping.

Based on these results and analysis, we can state that an induced extra FM superexchange effect among Fe_{Oct} sites in the surface layers is only triggered by adsorption of bridging ligand that electronically connect different Fe_{Oct} sites, such as acetate, phosphonate, catechol, and silanetriol derivates but not of monocoordinated molecules, such as ethanol. We further proved this concept by calculating the monodentate AA at local high coverage, as shown in Figure 3.16. Indeed, a tiny energy cost of 47 meV was obtained for ΔE_{SF+Rel}, confirming a cheap spin-flip process, in contrast with what observed for the bidentate (bridging) mode whose ΔE_{SF+Rel} is three times larger.

In this last paragraph, the role played by ligands on the NP surface reconstruction is investigated, since this is one of the major factors affecting the saturation magnetization of NPs, together with spin-canting and the presence of antiphase domain boundaries. In a previous work by my group [125], it was proved that bulk-like cubic NPs are stabilized by surface reconstruction, which consists in the

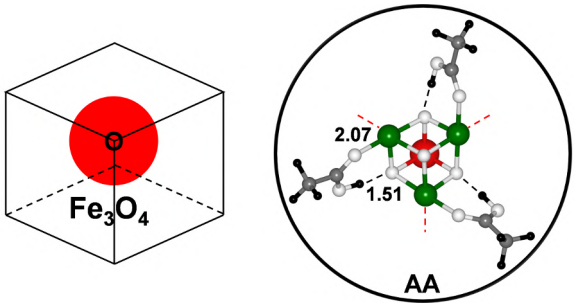

Figure 3.16: Ball-and-stick representation for the adsorption of AA in the monodentate mode at local high coverage onto the NP corner. Only the ligands and the NP O-corner are shown for clarity, as schematized on the left. The red dashed lines indicate the edges of the hidden NP. The black dashed lines indicate the formation of hydrogen bonds. The H-bond and the Fe-O_{AA} bond lengths (in Å) for the asymmetric unit are shown. The black, gray, white, green, and red beads represent H, C, O, Fe, and Fe^{III}_{Oct} on which the spin-flip process is investigated, respectively.

transfer of six-coordinated iron ions nearby a Fe-corner from octahedral to tetrahedral sites (see Figure 3.17). Such atomic reconstruction was found to reduce the total magnetization of the NP by 9.7% (from 1232 to 1112 μ_B). In the present study, it was found out that this type of reconstruction stabilizes the cubic NP model under investigation by -10.6 eV. At the top of Figure 3.17, the NAKED NP is shown before (bulk-like, left) and after the atomic reconstruction (reconstructed, right), which involves three octahedral iron ions (blue beads in the image) for each Fe-corner (four out of a total of eight corners per cube). However, if the NP is fully decorated by the organic ligands (48AA), the reconstructed model is less stable than the bulk-like one by 7.4 eV (Figure 3.17, the bottom). The half coverage (24AA) was also considered: the reconstruction stabilizes the NP by -1.2 eV. Even if the energetic stabilization given by the reconstruction is largely reduced with respect the naked case, this is not sufficient to lift the reconstruction. Thus, only high coverage organic acid coating can reverse the energetics with respect to what observed for the naked NPs, largely stabilizing the bulk-like structure whose total magnetic moment is by far higher than that of the reconstructed NP (408 versus 288 μ_B, respectively). This finding is in line with what found by means of surface X-ray diffraction, infrared spectroscopy, and DFT+U calculations by Arndt and collaborators [85] for the (001) surface, i.e. that the adsorption of organic acid reverses the reconstruction process of the (001) surface, through the stabilization of the bulk-like structure and formation of deep bulk Fe vacancies. Furthermore, this result suggests that using coating agents during the synthesis of the nanostructures is a successful strategy to prepare NPs with high saturation magnetization, close to the bulk value.

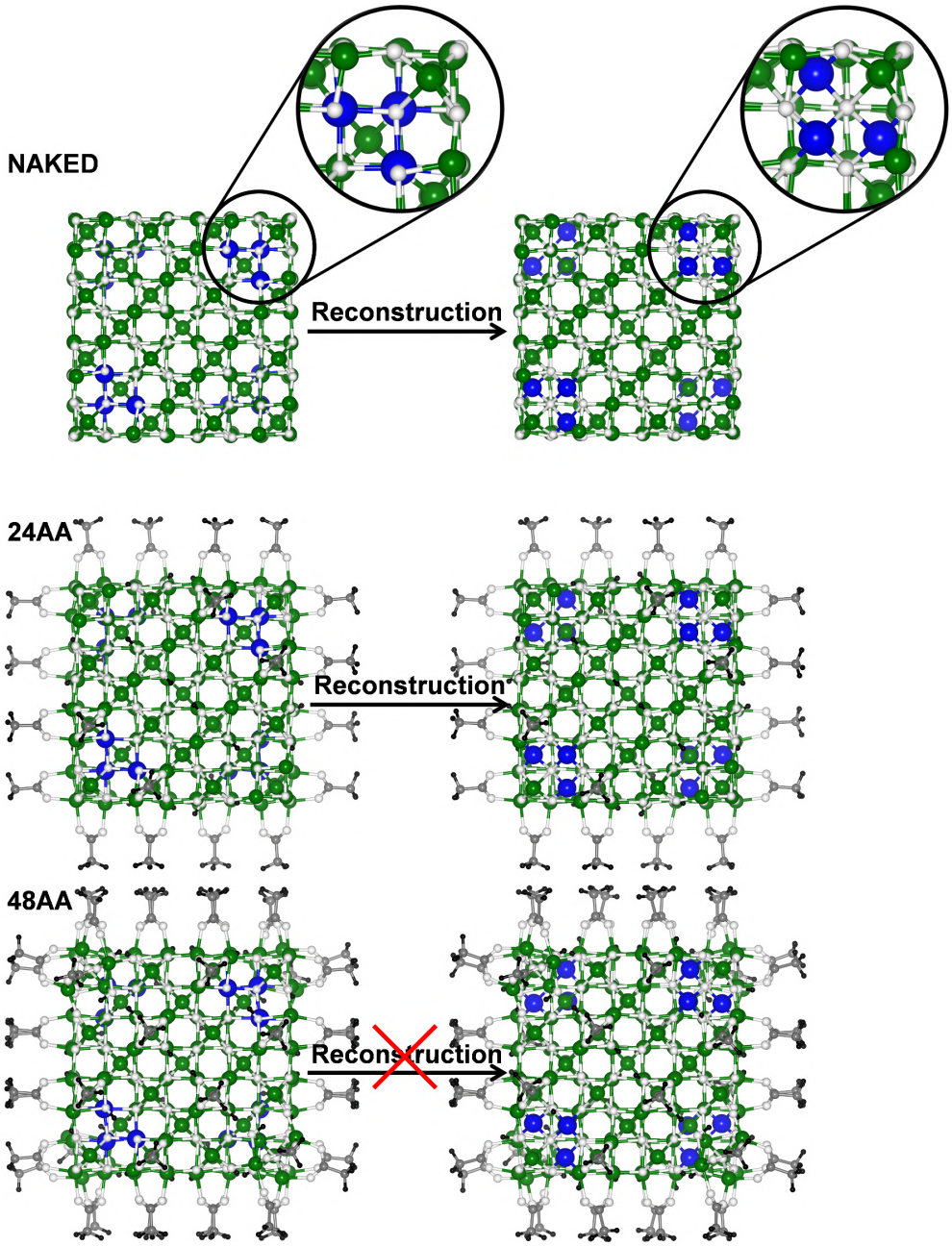

Figure 3.17: Ball-and-stick representations of the minimum energy structures of the unreconstructed (left) and reconstructed (right) NP in absence (NAKED), at half coverage (24AA) and at full coverage (48AA) of AA molecules. The black, grey, white, green, and blue beads represent H, C, O, Fe, and Fe_{Oct} which are involved in the reconstruction process, respectively. The insets show the details of the surroundings of the Fe_{Oct} ions that are involved in the reconstruction process.

3.4 Conclusions

It has been demonstrated that previously proposed explanations for the high magnetization (close to bulk one) of coated magnetite NPs with organic acids are not always robust or satisfactory. For example, the rationalization by Salafranca et al. [120] is based on different electronic structure properties of bare and functionalized magnetite surfaces from DFT calculations, which however are in contrast with all the other existing studies in the literature and with the results here reported. Another explanation, which is commonly mentioned in the experimental papers, attributes the enhanced magnetization to a higher crystallinity of coated NPs. However, no mechanism has yet been proposed with solid evidence.

From our results, a fundamental factor emerges: surface functionalization with carboxylic acids creates chemical bridges between Fe_{Oct} sites for an additional ferromagnetic superexchange interaction, which is an effective mechanism enhancing the overall NP magnetization by hampering spin-canting. We provided proof of this mechanism using a toy model of Fe^{III} tert-butoxide dimer. Moreover, in order to shed light on the origin of this extra FM superexchange, we investigated its relation with the charge transfer energy, i.e., the energy difference between O^{-II} p and Fe^{III}_{Oct} d states, that is expected to be of inverse proportionality [257]. Indeed, the charge transfer energy is lower for the fully coated NP than for the naked one, leading to a higher FM exchange coupling constant, in perfect agreement with the higher spin-flip energy cost observed in our calculations.

The present finding has been generalized to the family of multidentate bridging molecules. Indeed, not only carboxylic groups, commonly used to anchor surfactants (e.g. oleic acid) during NPs synthesis, but also other kinds of multidentate bridging anchoring groups, which can exchange with surfactants after the synthesis, are found to create electronic channels through chemical bridges between Fe_{Oct} sites that induce an extra ferromagnetic superexchange interaction, work against spin-flipping processes and, consequently, also against the reduction of the total magnetic moments observed for non-coated NPs. Our conclusion is corroborated by the fact that coating with monodentate ligands do not lead to such behavior.

Furthermore, we also show that surface functionalization by organic acids prevents crystallinity loss in NPs, which again improves their total magnetic moment. This is because the surface reconstruction, consisting of octahedral Fe ions that move into tetrahedral sites, is found not to be energetically favorable in the presence of the coating molecules.

To conclude, the results of this computational study provide a first-principles description, at the electronic and atomistic level, of the mechanisms how surface functionalization alters the spin and structural disorder (spin canting and atomic reconstruction) in magnetite NPs and, consequently, affects their saturation magnetization. Since this specific physical property is crucial for an efficacious

nanomedical application, the concepts developed here can be useful to guide the design and preparation of optimal magnetite-based nanostructures.

Chapter 4

Chemistry of the Interaction and Retention of Tc^{VII} and Tc^{IV} Species at the $Fe_3O_4(001)$ Surface

In this chapter, we studied the interaction between the $Fe_3O_4(001)$ surface and the pertechnetate ion ($Tc^{VII}O_4^-$), that is a nuclear fission product whose major issue is the high mobility in the environment. Experimentally, it is well-known that Fe_3O_4 can reduce $Tc^{VII}O_4^-$ to Tc^{IV} species and retain such products quickly and completely, but the exact nature of the redox process and products is not completely understood. Therefore, we investigated the chemistry of $Tc^{VII}O_4^-$ and Tc^{IV} species at the $Fe_3O_4(001)$ surface through a hybrid DFT functional (HSE06) method. We studied a possible initiation step of the Tc^{VII} reduction process. The interaction of the $Tc^{VII}O_4^-$ ion with magnetite surface leads to the formation of a reduced Tc^{VI} species without any change in the Tc coordination sphere, through an electron transfer that is favored by the magnetite surfaces with a higher Fe^{II} content. Furthermore, we explored various model structures for the immobilized Tc_{IV} final products. Tc^{IV} can be incorporated into a subsurface octahedral site or adsorbed on the surface in the form of $Tc^{IV}O_2{\cdot}xH_2O$ chains. We propose and discuss three model structures for the adsorbed $Tc^{IV}O_2{\cdot}2H_2O$ chains in terms of relative energies and simulated EXAFS spectra. Our results suggest that the periodicity of the $Fe_3O_4(001)$ surface matches that of the $TcO_2{\cdot}2H_2O$ chains. The EXAFS analysis suggests that in experiments $TcO_2{\cdot}xH_2O$ chains were probably not formed as an inner-shell adsorption complex with the $Fe_3O_4(001)$ surface.

The results reported in this chapter have been submitted as a full article to a peer-reviewed journal.

4.1 Introduction

Technetium is a major concern due to its radiotoxicity, high fission yield in nuclear reactors, long half-life, and long mobility in the environment. The β-emitting ^{99}Tc isotope is especially concerning. With a formation yield of ca 6% in both ^{235}U and ^{239}Pu nuclear reactors and a half-life of ca 2.1×10^5 years [164, 165, 171], ^{99}Tc will be the main radiation emitter 10^4 to 10^6 years after the production of the nuclear fuel waste.

In the absence of complexing agents besides oxygen and water, technetium assumes VII and IV oxidation states [169]. In oxidizing conditions, Tc^{VII} is preferred and forms the pertechnetate ion ($Tc^{VII}O_4^-$), which is highly soluble and mobile in the environment due to its weak interaction with mineral surfaces [170]. On the other hand, in non-oxidizing conditions, technetium is reduced to Tc^{IV}, precipitating as $Tc^{IV}O_2{\cdot}xH_2O$ or forming adsorption complexes with mineral phases containing Fe^{II}, which participate in the Tc^{VII} reduction [19, 20, 172, 177–183].

Magnetite ($Fe^{II}Fe_2^{III}O_4$) plays an important role in the immobilization of technetium in nuclear waste. In a typical geological nuclear waste repository, the spent nuclear fuel is enclosed in steel containers, which are then deposited in stable geological sites hundreds of meters below the surface; once full, the repository is sealed with bentonite clay and cement [174]. In such environment, magnetite forms as one of the main products of the anoxic corrosion of the steel containers [175]. It has been demonstrated that Fe^{II} in solid phases can quickly reduce $Tc^{VII}O_4^-$ to Tc^{IV} species [19, 20, 172, 177–183], whereas Fe^{III} solid phases can adsorb and incorporate Tc^{IV} [19, 20], hence the importance of magnetite in preventing the diffusion of Tc into the environment. It has been shown that Tc^{IV} remains adsorbed on or incorporated in the oxidized magnetite [19, 20]. However, the exact structure of the redox products has not been completely elucidated and is affected by several factors such as pH, initial Tc concentration, and redox conditions of the aqueous phase, among others.

In 2016 Yalçintaş et al. [185], based on *X-ray absorption near edge spectroscopy* (XANES) and *extended X-ray absorption fine structure* (EXAFS) measurements, found that the end product of $Tc^{VII}O_4^-$ reduction by magnetite is related to the initial Tc content in solution, with higher concentrations (2×10^{-4} M) favoring adsorption of dimeric Tc^{IV} oxides onto the magnetite surface and lower concentrations (2×10^{-5} M) favoring incorporation of Tc^{IV} into the magnetite lattice. A gradual transition from exclusively adsorbed to exclusively incorporated Tc was also observed with decreasing Tc concentration. On the other hand, when using mackinawite (FeS) instead of magnetite, Yalçintaş et al. [185] obtained non-crystalline $Tc^{IV}O_2{\cdot}xH_2O$ precipitates, for which two distinct linear chains of edge-sharing TcO_6 octahedra with the H_2O groups at the trans positions could be fitted to the EXAFS spectra; in the first structure, the Tc atoms are equally spaced along

the chains (as proposed by Lukens et al. [263]), whereas in the second the Tc-Tc distances alternate between shorter and longer values, as in the TcO_2 crystal structure [259]. In 2022, Oliveira et al. [264] used *density functional theory* (DFT) calculations and EXAFS data to show the precipitates are more likely formed by zigzag chains with terminal H_2O at cis positions. Thus, it is clear that the interpretation of EXAFS spectra for these Tc systems is rather complex and can benefit from the aid of quantum mechanics.

In this hybrid DFT study, we use a hybrid DFT functional method to explore the interaction of various Tc species with magnetite, starting from the adsorption of $Tc^{VII}O_4^-$ onto the $Fe_3O_4(001)$ surface and proceeding with possible products of the full $Tc^{VII}O_4^-$ reduction, namely Tc^{IV} incorporated into the magnetite lattice and adsorbed $Tc^{IV}O_2{\cdot}2H_2O$ chains. The $Tc^{VII}O_4^-$ adsorption is analyzed in terms of Mulliken spin densities and charges, and electronic density of states, whereas the structures of the Tc^{IV} species are discussed in terms of relative energies and simulated EXAFS spectra.

4.2 Methods and models

4.2.1 Computational methods

All DFT calculations were carried out with the HSE06 hybrid exchange-correlation functional [233, 240] (see Section 2.1 for further details about the method) using the CRYSTAL17 package [247, 248]. This method has been shown to give good description of structural, electronic, and magnetic properties of magnetite systems [33]. The Kohn-Sham orbitals were expanded in Gaussian-type orbitals: the all-electron basis sets are H−511G(p1), O−8411G(d1), Fe−86411G(d41), and Tc−976311(d631f1) according to the scheme previously used for Fe_3O_4 [33, 70, 265, 266]. The convergence criterion of $4.5{\times}10^{-4}$ hartree/bohr for atomic forces was used during geometry optimization and the convergence criterion for total energy was set to 10^{-6} hartree for all the calculations. The irreducible Brillouin zone was sampled with a $3 \times 3 \times 1$ k-point grid generated with the Monkhorst-Pack scheme [267]. For the calculation of the *projected density of states* (PDOS), a denser k-points mesh of $6 \times 6 \times 1$ was used. All structures (see details below) were constructed in such way as to keep inversion symmetry (e.g., by adding adsorbate molecules in specific locations above and below the slab models) in order to minimize the development of artificial dipole moments.

The EXAFS spectra were simulated for optimized structures with FEFF9.6.4 [268–270] using the self-consistent field mode with a global Debye-Waller factor of 0.003 Å, amplitude reduction factor of 0.9, and $\Delta E_0 = 0$.

4.2.2 Models of the $Fe_3O_4(001)$ surface

The (001) termination is one of the most stable magnetite surfaces [58, 59]. Under the alkaline conditions of geological repositories [20], it is expected to be one of the most exposed surfaces in nanostructures [62, 87], according to the Wulff construction [61]. For these reasons, we have used this surface in our model. In the [001] direction, the Fe_3O_4 consists of alternating planes containing tetrahedral iron (Fe_{Tet}) atoms and octahedral iron (Fe_{Oct}) coordinated to oxygen atoms. The most recent and reliable models for the (001) termination are based on a bulk truncation at the Fe_{Oct} and O plane. The distorted bulk truncation (DBT) model consists in a simple bulk truncation [43], whereas the subsurface cation vacancy (SCV) model shows a reconstruction that consists of an extra interstitial Fe_{Tet} atom in the second layer replacing two Fe_{Oct} atoms from the third layer (per the $(\sqrt{2} \times \sqrt{2}\ )$R45° unit cell) [79]. Their relative stability is highly dependent on the concentration of adsorbing molecules in the environment: an increasing amount of carboxylic acid or water molecules adsorbed onto the surface is found to favor the DBT structure [70, 81, 82, 85]. For more detailed information about the $Fe_{34}(001)$ surface, see Section 1.1.2. In this work, both models were constructed as a (1×1) 17-layer slab with inversion symmetry, as previously done by our group [70, 245]. The five layers in the middle of the slab were kept fixed at the bulk positions, whereas the other layers were free to relax.

4.2.3 Models for the adsorption of TcO_4^{n-} on the $Fe_3O_4(001)$ surface

Different complexes were constructed by adsorbing or embedding TcO_4^{n-} into different sites of the DBT and SCV surface models. The SCV surface being more oxidized (fewer Fe^{II} centers) than the DBT one, it is interesting to compare the reducing power of both surface models. Since the DBT and SCV surfaces have identical terminating layers, exposing four penta-coordinated Fe_{Oct} atoms per unit cell, the models were built with the same criteria. The coordination shell of the superficial undercoordinated Fe_{Oct} atoms was saturated with either H_2O molecules or OH species, based on experimental and computational results [70, 245, 261]. To balance the total charge, the most reactive superficial oxygen atoms were decorated with a proper number of hydrogen atoms [254–256]. All structures were optimized, and, for each surface, the two lowest energy structures were selected for further analysis. Here, only the models associated to the two lowest energy structures are described in detail. The first model was built by adsorbing a TcO_4 species on two superficial undercoordinated Fe_{Oct} atoms and a H_2O molecule and a OH species on the two remaining superficial undercoordinated Fe_{Oct} atoms. Two superficial oxygen atoms were decorated with two hydrogen atoms. The second model was

built by attaching a TcO_2 fragment to two superficial oxygen atoms, forming a TcO_4^{n-} species embedded into the surface. The four superficial undercoordinated Fe_{Oct} atoms were saturated by one H_2O molecule and three OH groups. No superficial oxygen atoms were decorated with hydrogen atoms. These two models have the same number of atoms for each element.

4.2.4 Models for the incorporation of Tc^{IV} in the $Fe_3O_4(001)$ surface

Two models of Tc^{IV} incorporation were considered for the DBT (001) surface. In the first one, a Fe_{Oct} atom from the third layer was simply replaced with a Tc atom, whereas in the second model a Fe vacancy was created in addition to the Tc substitution (i.e., two Fe_{Oct} atoms were replaced with one Tc). In the latter case, several models were created with the vacancy at different positions with respect to the Tc atom and the structure with the lowest energy was selected for further analysis. We only considered the DBT (001) surface model because recent experimental and theoretical findings show that the diffusion of other transition metal atoms could reverse the SCV reconstruction, restoring a DBT surface, which presents the diffusing transition metal atom (Tc in this case) instead of Fe occupying an octahedral site in the third layer [205–207].

4.2.5 Models for the adsorption of $Tc^{IV}O_2{\cdot}2H_2O$ chains on the $Fe_3O_4(001)$ surface

Three models were considered for the $Tc^{IV}O_2{\cdot}2H_2O$ infinite chains, based on the work by Oliveira et al. [264]. Each chain consists of edge-sharing TcO_6 octahedra with terminal H_2O groups occupying two corner positions. In α-$Tc^{IV}O_2{\cdot}2H_2O$, the TcO_6 octahedra form a linear chain with the terminal H_2O in *trans* configuration and Tc-Tc nearest neighbors alternating longer and shorter distances along the chain as in the TcO_2 ($P2_1/c$) crystal structure [259]. In β-$Tc^{IV}O_2{\cdot}2H_2O$, the TcO_6 octahedra form a zigzag chain, similar to ReO_2 ($Pbcn$) [271] — note that Re is regarded as a Tc analogue — with the H_2O groups at *cis* positions and identical distances for the Tc-Tc nearest neighbors. The last model, γ-$Tc^{IV}O_2{\cdot}2H_2O$, differs from α-$Tc^{IV}O_2{\cdot}2H_2O$ for having identical Tc-Tc nearest distances along the chain, as in ReO_2 ($P4_2/mnm$) [272]. Oliveira et al. [264] found β-$Tc^{IV}O_2{\cdot}2H_2O$ to be the most energetically favored structure, with γ-$Tc^{IV}O_2{\cdot}2H_2O$ being the least favored.

The adsorption complexes were constructed by removing the H_2O groups from one side of the $Tc^{IV}O_2{\cdot}2H_2O$ chains and placing the resulting structures on the $Fe_3O_4(001)$ bare surface at bonding distance. Different models were constructed for each chain to explore different orientations on the surface. All structures were

optimized and the lowest energy structure of adsorbed α, β, and γ chains were used for further analysis. The investigation was restricted to the SCV surface because (i) the SCV differs from the DBT only in the structure of the second and third layers and in the Fe^{II}/Fe^{III} ratio and it is reasonable to suppose that these differences do not influence the adsorption properties, especially when no redox reactions involve the Fe^{II}/Fe^{III} pair, as in this case, and (ii) the SCV, being more oxidized than the DBT and characterized by iron vacancies, bears stronger resemblance to maghemite, which is expected to be one of the main products of the magnetite oxidation by TcO_4^-.

4.3 Results and discussion

4.3.1 Adsorption of TcO_4^{n-} on the $Fe_3O_4(001)$ surface

In the first part of the study, we simulated the interaction of TcO_4^{n-} species with the $Fe_3O_4(001)$ surface by considering that the ions may either just adsorb by binding to undercoordinated surface Fe ions or become involved in surface reactivity leading to their surface embedding. The details of the models are described in Methods and Models section. For both DBT and SCV surfaces, we have selected the two lowest energy adsorption complexes, shown in Figure 4.1. In the models reported in the left panels of Figure 4.1 (referred to as $(Tc^{VII}O_4)^-$/DBT and $Tc^{VII}O_4)^-$/SCV, as discussed below), TcO_4^{n-} is adsorbed on two penta-coordinated Fe_{Oct} of the surface through two μ-O (i.e., two-fold coordinated oxygen) bridging atoms. In the models reported in the right panels of Figure 4.1 (referred to as $(Tc^{VI}O_4)^{2-}$/DBT and $(Tc^{VI}O_4)^{2-}$/SCV, as discussed below), TcO_4^{n-} becomes embedded in the surface forming two μ_4-O (i.e., four-fold coordinated oxygen) bridging atoms. This second adsorption site is the same that is generally preferred by single metal atoms adsorbed on the $Fe_3O_4(001)$ surface, according to several recent studies [205, 252, 273].

$(Tc^{VII}O_4)^-$/DBT and $(Tc^{VII}O_4)^-$/SCV models are characterized by the presence of Tc in its VII oxidation state. As we can see in the PDOS in Figure 4.2, there are no Tc 4d states (Figure 4.2, cyan curve) in the valence band. All technetium 4d orbitals are located in the conduction band. Furthermore, Tc is characterized by no spin polarization. These findings are compatible with a Tc^{VII} species, corresponding to the electronic configuration [Kr]. On the other hand, in $(Tc^{VI}O_4)^{2-}$/DBT and $(Tc^{VI}O_4)^{2-}$/SCV models, we observe that Tc^{VII} is reduced to Tc^{VI} while one Fe^{II} of magnetite is oxidized to Fe^{III}. The reduction of Tc^{VII} to Tc^{VI} is in line with the Mulliken charge decrease of 5%, and with a Tc 4d contribution to the valence band in the spin-down channel of the PDOS (Figure 4.2, cyan curve). Indeed, the Mulliken spin density value of -0.7 μ_B for Tc in both

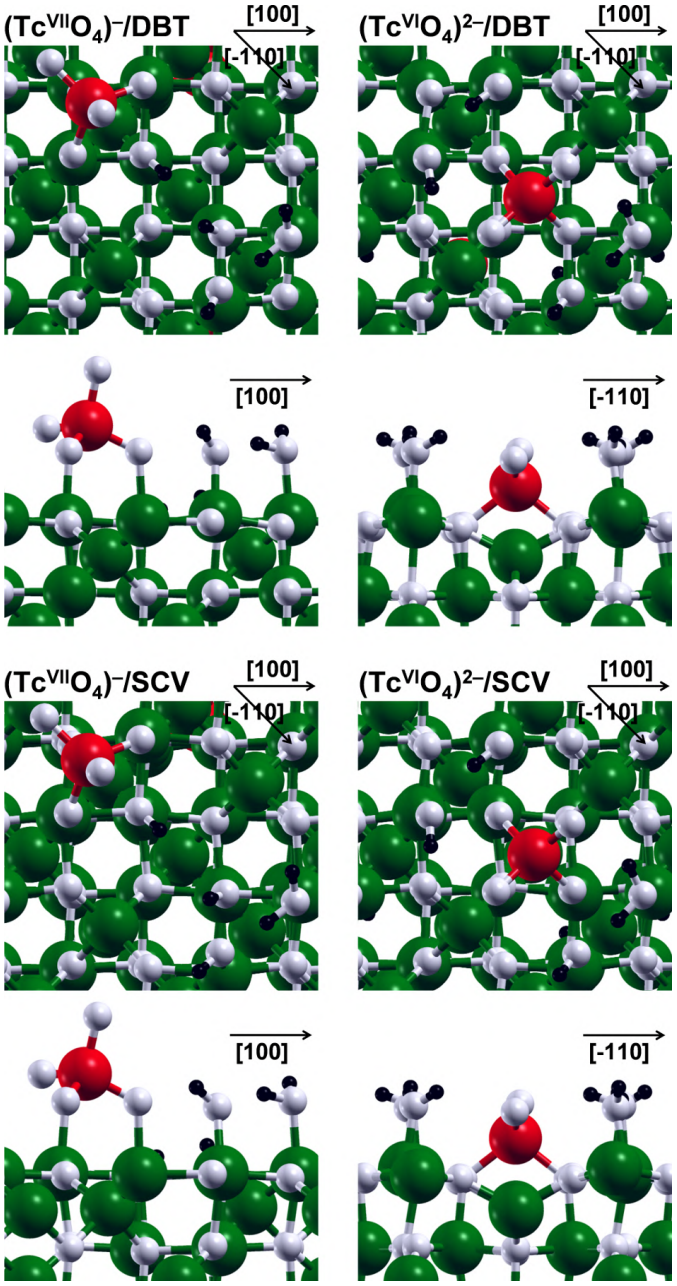

Figure 4.1: Top and side views of the optimized structures for the lowest-energy TcO_4^{n-} complexes adsorbed onto the DBT (on the top) and SCV (on the bottom) $Fe_3O_4(001)$ surfaces. Black, white, green, and red beads represent H, O, Fe, and Tc, respectively. Black arrows indicate the crystallographic directions.

$(Tc^{VI}O_4)^{2-}$/DBT and $(Tc^{VI}O_4)^{2-}$/SCV is consistent with a Tc^{VI} species with electronic configuration [Kr]$4d^1$, i.e., with one unpaired electron. The Fe^{II} (high spin [Ar]d^6 configuration) oxidation to Fe^{III} (high spin [Ar]d^5 configuration) is confirmed by the Mulliken charge and spin density increase of 15% and from 3.7 to 4.2 μ_B, respectively. Despite the similar structural and electronic properties of the DBT and SCV adsorption complexes, the redox energies differ considerably: the reaction energy per Tc atom is 1.06 eV for $(Tc^{VII}O_4)^{-}$/SCV $\longrightarrow$ $(Tc^{VI}O_4)^{2-}$/SCV and 0.14 eV for $(Tc^{VII}O_4)^{-}$/DBT $\longrightarrow$ $(Tc^{VI}O_4)^{2-}$/DBT. This is consistent with the higher Fe^{II} content in the DBT surface, which would make the Tc^{VII} reduction to Tc^{VI} more favorable in comparison to the more oxidized SCV surface.

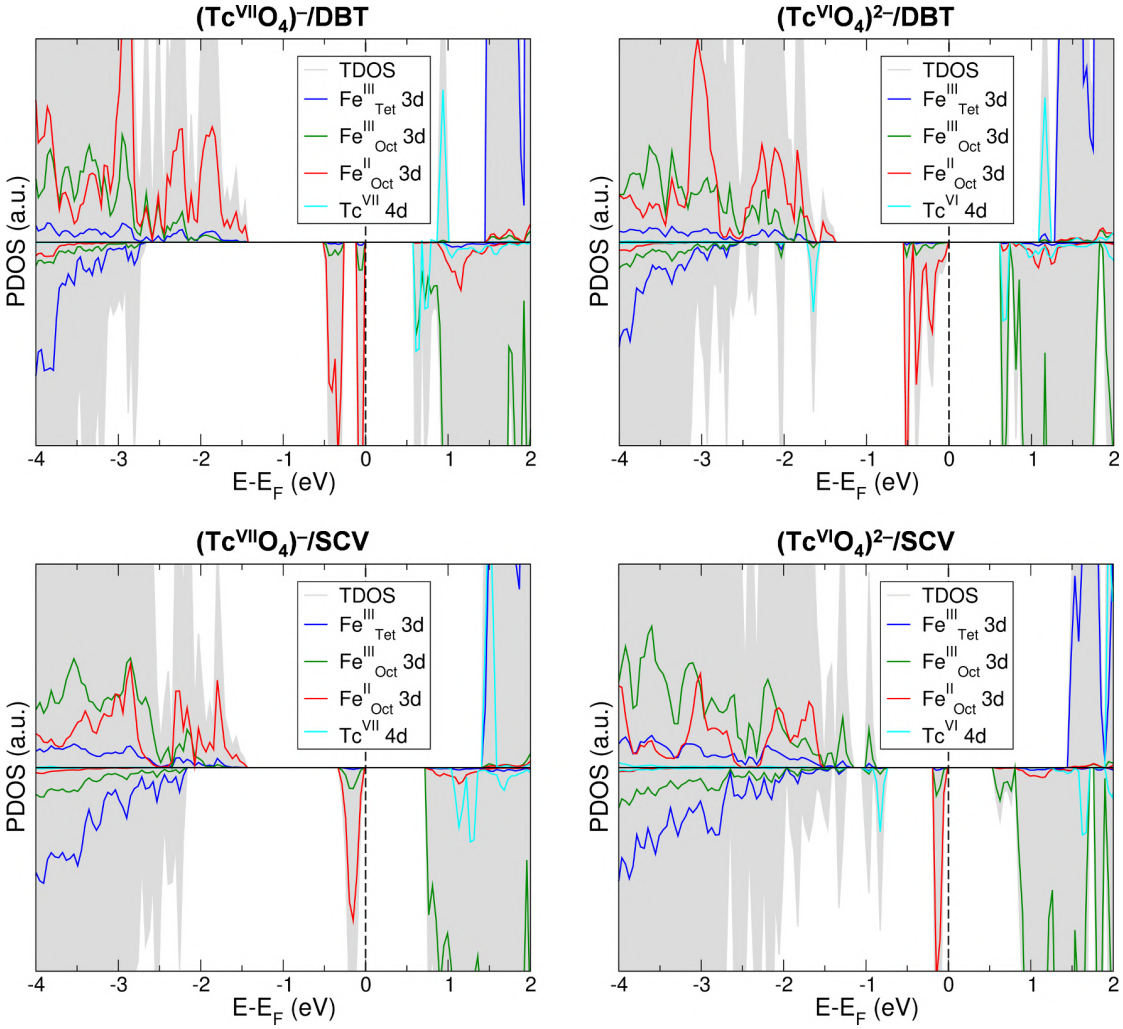

Figure 4.2: PDOS for the lowest-energy TcO_4^{n-} complexes adsorbed onto the DBT (on the top) and SCV (on the bottom) $Fe_3O_4(001)$ surfaces, shown in Figure 4.1.

The reduction of Tc^{VII} to Tc^{VI} by a *simple* electron transfer (from the magnetite surface to the technetium atom) is likely the first step of a *complex* redox process, which is known to proceed rapidly to Tc^{IV} end-members at slightly alkaline pH, involving the oxidation of Fe^{II} close to the Tc adsorbate, changing the Tc geometry from tetrahedral to octahedral [274] — similarly to what happens during the reduction of $Mn^{VII}O_4^-$ to $Mn^{IV}O_2$, passing through $Mn^{VI}O_4^{2-}$ [275]. Given the complexity of the process and the lack of more specific information regarding the chemical species involved, the simulation of the full $Tc^{VII}O_4^-$ reduction is out of the scope of this work. Therefore, we restrict our study to hypothetical final products: incorporation of Tc^{IV} in the magnetite slab and formation of $Tc^{IV}O_2{\cdot}2H_2O$ chains adsorbed on the magnetite surface.

4.3.2 Incorporation of Tc^{IV} in the $Fe_3O_4(001)$ surface

In Figure 4.3 two models for the incorporation of Tc into the DBT surface are shown, where we replaced a subsurface Fe_{Oct} in the third layer with a substitutional Tc atom (Tc_S) with (on the right) and without (on the left) the formation of a Fe_{Oct} vacancy (Fe_V). The (Tc_S)@DBT model presents a Tc in the IV oxidation state in place of a Fe^{III}, as confirmed by the Mulliken charge value, which is lower than those found for Tc^{VII} and Tc^{VI}, and almost identical to that obtained for Tc in the rutile phase of TcO_2. The charge balance of the system is achieved by the reduction of a Fe^{III} ion to Fe^{II}, indicated by the decrease of the Mulliken charge (15%) and spin density (from 4.2 to 3.7 μ_B). This incorporation scheme consists of two Fe^{III} ions being replaced with a Tc^{IV}-Fe^{II} pair, as already observed in previous computational studies investigating Tc incorporation in bulk hematite and magnetite [184, 276].

Similarly to (Tc_S)@DBT, the (Tc_S+Fe_V)@DBT model also presents Tc in the IV oxidation state. However, in this case, the Mulliken charges indicate that one Tc^{IV} ion replaces two Fe^{II} ions, keeping the charge neutrality of the system, as previously observed for Tc-doped bulk magnetite [184]. This model resembles what is observed in the oxidation process from magnetite (Fe_3O_4) to maghemite (γ-Fe_2O_3), which have the same structure, but the Fe^{II} ions in magnetite are replaced by Fe^{III} ions and vacancies in maghemite [265]. Nonetheless, both (Tc_S)@DBT and (Tc_S+Fe_V)@DBT have Tc incorporated as Tc^{IV} in octahedral coordination and are, thus, possible end products of the TcO_4^- reduction by magnetite.

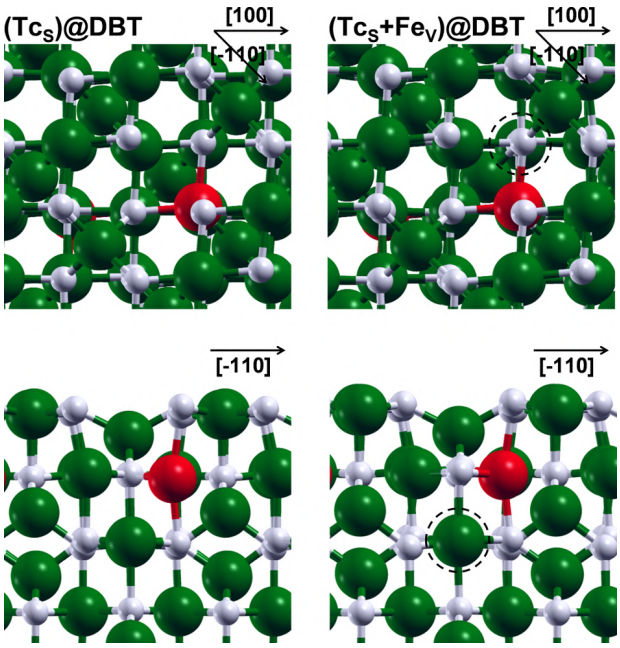

Figure 4.3: Top and side views of the optimized structures for the Tc^{IV} incorporated (Tc_S) into the (on the left) DBT $Fe_3O_4(001)$ surface and (on the right) DBT $Fe_3O_4(001)$ surface with a Fe_{Oct} vacancy (Fe_V) in the fifth layer, indicated by a dashed circle. White, green, and red beads represent O, Fe, and Tc, respectively. Black arrows indicate the crystallographic directions.

4.3.3 Adsorption of $Tc^{IV}O_2{\cdot}2H_2O$ chains on the $Fe_3O_4(001)$ surface

An alternative surface reactivity discussed in the literature would lead to the formation of hydrated $Tc^{IV}O_2$ dimers or chains on the magnetite surface [20, 185, 277]. To study this possibility, we first investigated a free-standing $Tc^{IV}O_2{\cdot}2H_2O$ chain, as described in Methods and Models section. The β-$TcO_2{\cdot}2H_2O$ chain was found to be the most stable chain, with Tc-Tc and Tc-O distances of ca 2.4 and 1.9 Å, respectively. The α-$TcO_2{\cdot}2H_2O$ chain is found to be less stable by +0.758 meV per Tc atom (as reported in Table 4.1), with alternating Tc-Tc distances of ca 2.2 and 3.3 Å. Consequently, also Tc-O distances present alternating values: 1.9 Å when O is bridging Tc-Tc at smaller distance and 2.1 Å when bridging the Tc-Tc at longer separation. The γ-$TcO_2{\cdot}2H_2O$ transformed to the α chain during the geometry optimization.

As a next step, we investigated the interaction between the $TcO_2{\cdot}2H_2O$ chains with the magnetite surface. The periodicity of the magnetite surface and, in particular, of the alternating O-O distances along the [-110] direction matches

Table 4.1: Relative total energies per Tc atom (in meV) of the α-$TcO_2{\cdot}2H_2O$, β-$TcO_2{\cdot}2H_2O$, and γ-$TcO_2{\cdot}2H_2O$ chains in vacuum and adsorbed onto the SCV $Fe_3O_4(001)$ surface.

	α-$TcO_2{\cdot}2H_2O$	β-$TcO_2{\cdot}2H_2O$	γ-$TcO_2{\cdot}2H_2O$
Vacuum	+758	0	-
Adsorbed on $Fe_3O_4(001)$	+16	+343	0

that of the α-$TcO_2{\cdot}2H_2O$ chain. The adsorbed α-$TcO_2{\cdot}2H_2O$ chain (Figure 4.4, α-$TcO_2{\cdot}2H_2O$/SCV) presents only one kind of Tc (Figure 4.4, red beads), that is six-coordinated by four O from the chain itself (Figure 4.4, blue beads), one O shared with magnetite, and one O from a water molecule (Figure 4.4, white beads). Half of the O bridges in the chain (indicated with a yellow star in Figure 4.4) interacts with exposed undercoordinated Fe (Figure 4.4, green beads). The adsorption is driven by two types of interaction: one between Tc^{IV} and magnetite O, and the other between surface Fe^{III} and O belonging to $TcO_2{\cdot}2H_2O$ chains. α-$TcO_2{\cdot}2H_2O$/SCV presents different alternating Tc-Tc distances with respect to the free-standing chain: ca 2.8 and 3.1 Å versus 2.2 and 3.3 Å. This significant difference is due to the periodicity of the magnetite surface and, in particular, of the alternating O-O distances along the [-110] direction, i.e., the direction along which the α chain is adsorbed.

Perpendicularly to the [-110] direction the surface periodicity is significantly different. In particular, the periodicity of the almost constant O-O distances along the magnetite [110] direction matches that of the γ-$TcO_2{\cdot}2H_2O$ chain, which was not stable in vacuum. The adsorbed γ-$TcO_2{\cdot}2H_2O$ chain (Figure 4.4, γ-$TcO_2{\cdot}2H_2O$/SCV) presents only one kind of Tc, whose coordination sphere is analogue to the one in α-$TcO_2{\cdot}2H_2O$/SCV. Still in analogy to α-$TcO_2{\cdot}2H_2O$/SCV, half of the O atoms in the chain is interacting with superficial undercoordinated Fe. These structural similarities are translated into comparable energies: the total energies difference between the adsorbed γ and α chain is only 16 meV per Tc atom (as reported in Table 4.1), in favor of the former.

The free-standing β chain has a shorter lattice parameter than the α and γ chains due to its zigzag configuration. Consequently, it is not possible to efficiently adsorb the β-$TcO_2{\cdot}2H_2O$ along the diagonal direction of the cell as previously done for the α and γ one. Therefore, we studied the adsorption of the β-$TcO_2{\cdot}2H_2O$ along the [100] direction (Figure 4.4, β-$TcO_2{\cdot}2H_2O$/SCV). In this case, two different kinds of Tc are present: one farther from the surface and one closer to it, labeled as Tc_{up} and Tc_{down} in Figure 4.4, respectively. Both Tc_{up} and Tc_{down} species are six-coordinated. Each Tc_{up} is coordinated by four O from the chain itself and by two O from two different water molecules, whereas each Tc_{down} is

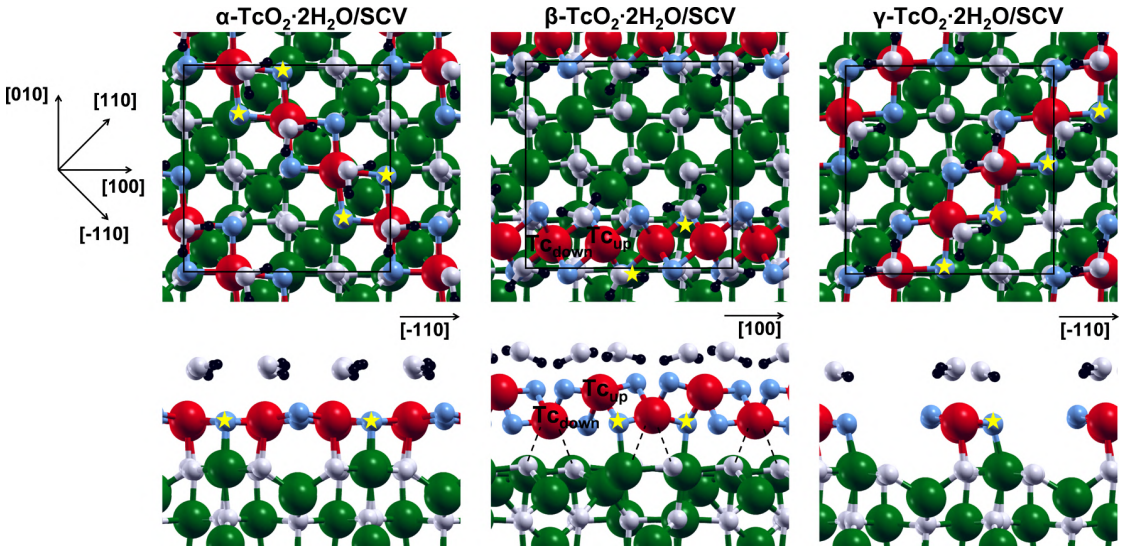

Figure 4.4: Top and side views of the optimized structures for the α-$TcO_2{\cdot}2H_2O$, β-$TcO_2{\cdot}2H_2O$, and γ-$TcO_2{\cdot}2H_2O$ chains adsorbed on the SCV surface. The axis orientation for the top views is shown on the left, whereas for the side views it is shown in each single panel. Black, white, blue, green, and red beads represent H, O belonging to H_2O and Fe_3O_4, O belonging to TcO_2, Fe, and Tc, respectively. Yellow stars indicate O of TcO_2 interacting with surface Fe. Black dashed lines indicate weak Tc-O interactions.

coordinated by four O from the chain itself and by two O shared with magnetite (Figure 4.4, dashed lines). Tc-Tc distances and other structural parameters of the adsorbed chain are not significantly different from what is observed for the free-standing chain. This configuration is found to be less favored than the α and γ one by +0.327 and +0.343 meV per Tc atom (see Table 4.1), respectively. This is an unexpected result, since the β-$TcO_2{\cdot}2H_2O$ chain is the most stable one in vacuum. This finding can be understood in terms of the (i) lower number (half compared to α and γ cases) of chain O atoms interacting with the magnetite surface (indicated with a yellow star in Figure 4.4) and (ii) weaker Tc-O interactions (2.3-2.4 versus 1.9-2.0 Å for the α and γ chains) between the chain and the magnetite surface (Figure 4.4, dashed lines).

Finally, we compared the experimental EXAFS spectra for the sorption complex by Yalçintaş et al. [185] (Figure 4.5, black dashed curve) and for the aged $TcO_2{\cdot}2H_2O$ precipitate by Oliveria et al. [264] (Figure 4.5, black dotted curve) with the calculated EXAFS spectra obtained for the simulated $TcO_2{\cdot}2H_2O$ chains adsorbed on the magnetite (001) surface just described. Regarding the experimental sorption complex curve, there is no match with the calculated curves of the simulated $TcO_2{\cdot}2H_2O$ chains models. We also modeled a magnetite/TcO2-dimer complex (shown in Figure 4.6) in line with what suggested by Yalçintaş and col-

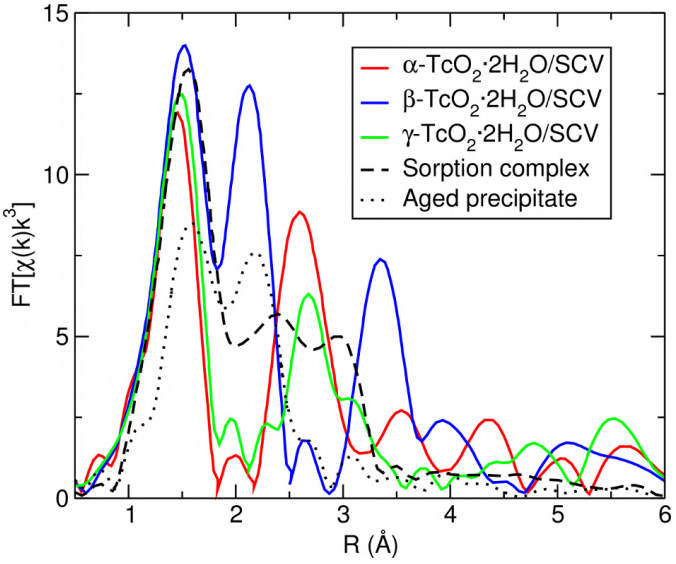

Figure 4.5: Experimental EXAFS spectra for the sorption complex by Yalçintaş et al. [185] (black dashed line) and aged $TcO_2{\cdot}xH_2O$ precipitate by Oliveira et al. [264] (black dotted line), and simulated EXAFS spectra for the α-$TcO_2{\cdot}2H_2O$ (red line), β-$TcO_2{\cdot}2H_2O$ (blue line), and γ-$TcO_2{\cdot}2H_2O$ (green line) chains adsorbed onto the SCV $Fe_3O_4(001)$ surface.

laborators [185]. However, also in this case, the simulated EXAFS spectrum does not match the experimental one for the sorption complex. These results suggest that TcO_2 chains (or dimers) are probably not formed as an inner-shell adsorption complex with the $Fe_3O_4(001)$ surface, at least not immediately. Regarding the aged $TcO_2{\cdot}xH_2O$ precipitate curve, there are few similarities with the calculated β-$TcO_2{\cdot}2H_2O$/SCV curve (Figure 5, blue curve). In particular, the positions of the first and second peak are in fair agreement, as well as the presence of a small shoulder on the right of the second peak, but the third peak in the computed curve finds no correspondence in the experimental one. This result suggests that β-$TcO_2{\cdot}2H_2O$ chains might be formed in solution, not as an inner-shell adsorption complex with magnetite, and only afterward might precipitate and adsorb on the surface. Indeed, the formation of β-$TcO_2{\cdot}2H_2O$ chains is energetically favored over that of the α and γ ones in vacuum, not on the $Fe_3O_4(001)$ surface (see Table 4.1). However, the agreement between the experimental aged precipitate curve and the computed β-$TcO_2{\cdot}2H_2O$/SCV one is not good enough to definitively sustain this hypothesis. Therefore, the comparison between the experimental and the calculated data suggests the possibility that in the above mentioned experiments [185, 264] different magnetite surfaces might be involved, such as the (111) and (110) ones, which were not considered in this work.

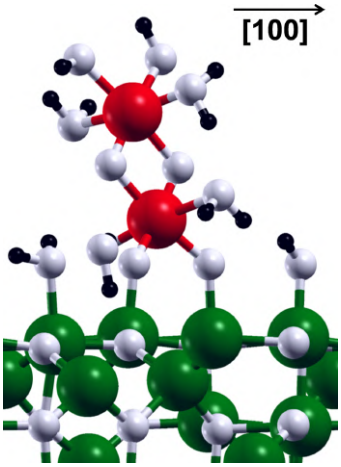

Figure 4.6: Side view of the optimized structure for the lowest-energy SCV $Fe_3O_4(001)/TcO_2$-dimer complex. Different SCV $Fe_3O_4(001)/TcO_2$-dimer models were constructed to explore different orientations and adsorption mode. All structures were optimized and only the lowest energy structure is shown here. Black, white, green, and red beads represent H, O, Fe, and Tc, respectively. Black arrow indicates the crystallographic direction.

4.4 Conclusions

In this work based on a comprehensive hybrid DFT study, we investigate the chemistry of the interaction and retention of Tc^{VII} and Tc^{IV} species at the $Fe^3O_4(001)$ surface.

As a first step, we studied the interaction and reactivity of the $Tc^{VII}O_4^{n-}$ ion with the magnetite surface. We suggest a possible initiation step for the reduction of Tc^{VII} to Tc^{IV} upon contact with $Fe_3O_4(001)$ surface. The adsorption of the $Tc^{VII}O_4^{n-}$ ion onto the magnetite surface leads to the formation of a reduced Tc^{VI} species without any change in the Tc coordination sphere, through an electron transfer that is favored by the magnetite surfaces with a higher Fe^{II} content.

Furthermore, we explored various model structures for the possible final products of the full reduction from Tc^{VII} to Tc^{IV}: Tc^{IV} incorporation or adsorption in the form of $Tc^{IV}O_2{\cdot}2H_2O$ chains. The Tc incorporation into an octahedral site leads to the presence of a six-coordinated Tc^{IV}. Regarding the adsorption of $TcO_2{\cdot}2H_2O$ chains on magnetite, we propose three model structures which are characterized by three different symmetries. The periodicity of the $Fe_3O_4(001)$ surface matches that of the $TcO_2{\cdot}2H_2O$ chains and the adsorption is driven by two types of interaction: one between Tc^{IV} and magnetite O, and the other between surface Fe^{III} and O belonging to $TcO_2{\cdot}2H_2O$ chains. However, the comparison between the experimental and computed EXAFS spectra suggests that in exper-

iments $TcO_2 \cdot xH_2O$ chains were probably not formed as an inner-shell adsorption complex with the $Fe_3O_4(001)$ surface.

To summarize, we have demonstrated that the $Fe_3O_4(001)$ surface can adsorb and reduce Tc^{VII} complexes and retain Tc^{IV} species. In particular, we propose an initiation step for the reduction of Tc^{VII} and two retention mechanisms, i.e., Tc^{IV} ions incorporation into octahedral subsurface sites and adsorption in the form of $TcO_2 \cdot 2H_2O$ chains. Therefore, our results furnish a solid basis for any future study whose aim is to elucidate the overall mechanism of the complex reduction of Tc^{VII} to Tc^{IV} and, on the basis of the EXAFS analysis, could stimulate further investigations to understand whether the formation of $TcO_2 \cdot xH_2O$ chains could take place in solution or at other Fe_3O_4 surfaces as well.

Chapter 5

Improving Oxygen Evolution Reaction on $Fe_3O_4(001)$ with ad-hoc Single-Atom Catalysts

In this chapter, we investigated the $Fe_3O_4(001)$ surface as support material for *single-atom catalysts* (SACs) for the *oxygen evolution reaction* (OER). Doping magnetite surfaces with transition metal atoms is a promising strategy to improve the catalytic performance towards the OER, which governs the overall efficiency of the water electrolysis and hydrogen production. First, we prepared and optimized models of trapped inexpensive and abundant transition metal atoms, such as Ti, Co, Ni, and Cu, in various configuration on the $Fe_3O_4(001)$ surface. Then, we studied their structural, electronic, and magnetic properties through HSE06 hybrid functional calculations. As a further step, we investigated the performance of these model electrocatalysts towards the OER, considering different possible mechanisms, in comparison with pristine magnetite surface, on the basis of the computational hydrogen electrode (CHE) model developed by Nørskov and coworkers. Co-doped systems are found to be the most promising electrocatalytic systems among those considered in this work. Overpotentials values ($\sim$0.35 V) are in the range of those experimentally reported for mixed Co/Fe oxide (0.24-0.49 V).

The results reported in this chapter have been submitted as a full article to a peer-reviewed journal.

5.1 Introduction

Renewable resources to produce electricity, such as solar or wind power, are emerging alternatives to decrease the use of fossil fuels. However, their fluctuating nature imposes great challenges since energy storage solutions are required to compensate for downtime in production. Water electrolysis, also known as electrochemical water splitting, is a promising technology for the storage of surplus electric energy via conversion into chemical energy in the form of hydrogen gas fuel.

The process comprises two half-cell reactions separated by a membrane: the cathodic *hydrogen evolution reaction* (HER)

$$2H^+ + 2e^- \longrightarrow H_2$$

and the anodic *oxygen evolution reaction* (OER)

$$2H_2O \longrightarrow O_2 + 4H^+ + 4e^-$$

under acidic conditions. OER is more kinetically sluggish because it is a four-electron transfer reaction, if compared with HER that requires only two electrons. Therefore, the key process governing the overall efficiency of water electrolysis is the OER, which is often referred to as the bottleneck of the hydrogen production from water.

State-of-the-art OER electrocatalysts contain noble metals, e.g., Ru, Ir, and Pt, and work in acidic media, showing noticeable stability and activity [278]. However, such catalysts are not convenient for large-scale applications because of the scarcity and cost of the precious metals involved in their realization. On the contrary, in alkaline solution many abundant and inexpensive metals, e.g., Fe, Co, and Ni, and their alloys show comparable catalytic performance than noble metals [189].

Nonetheless, alkaline water electrolysis has long been considered inefficient compared to acidic electrolysis, because of the poor performance of the hydroxide-conducting polymer electrolyte membranes (PEMs) separating the two half-cells, as compared to the proton-conducting ones. However, recent studies have suggested that is possibile to reach similar or even higher activities with alkaline cells through the optimization of the hydroxide-conducting PEMs that are currently used in existing systems [190, 191]. Therefore, the search for good OER catalysts in alkaline media is an active field of research, where transition metal oxides, hydroxides, and oxyhydroxides containing Ni, Co and Fe have been proposed as suitable candidates [214–219, 279–283].

Recently, magnetite (Fe_3O_4) has attracted the interest of the scientific community as a simple model surface where to investigate the complex OER mechanism, since this is still under debate when the newly emerging inexpensive transition metal oxide catalysts are involved. In particular, the $Fe_3O_4(001)$ surface, besides

being the most stable and exposed facet in magnetite nanostructures [58, 59, 61, 62, 87], it is also the best understood and well-defined in terms of the atomic structure, both in vacuum and water environment, which is a crucial aspect when trying to determine what are the reaction intermediates on the surface along the reaction path.

The stacking sequence in the [001] direction consists of A layers that contain Fe_{Tet} and B layers that contain O and Fe_{Oct}. Over time, different atomic structure models have been proposed for the (001) surface. In 2005, based on *density functional theory* (DFT) calculations, Pentcheva et al. [43] proposed a *clean* B layer termination, called *distorted bulk truncation* (DBT) model, thermodynamically more stable than other previously suggested configurations [43, 76]. In 2014, through a combined experimental and theoretical study, Bliem et al. [79] proposed a new reconstructed surface model, called *subsurface cation vacancy* (SCV), characterized by a B layer-terminated $Fe_3O_4(001)$ surface with an extra interstitial Fe_{Tet} in the second layer, replacing two Fe_{Oct} that are removed from the third layer, per each $(\sqrt{2} \times \sqrt{2})R45°$ unit cell. As detailed in Section 1.1.2, the SCV model shows a much better agreement with experimental findings [77–80] and is found to be more stable than the DBT model in vacuum and under water exposure up to elevated temperature, i.e., more than 700 K [70, 81–84]. Furthermore, the structure of the $Fe_3O_4(001)$/water interface has also been elucidated in recent years [70, 245, 261].

Fe_3O_4 was experimentally reported to be characterized by a good stability and a fair activity towards OER. Through *low-energy electron diffraction* (LEED), *scanning tunneling microscopy* (STM), and *atomic force microscopy* (AFM) measurements, Mullner et al. [24] did not register any change in the SCV surface morphology after having increased the pH up to the values that are typically used for the water oxidation by transition metal oxides in alkaline conditions. They also observed that the SCV surface morphology was unchanged after having performed the OER, i.e., several cyclic voltammetry scans at an overpotential value of 0.48 V. Similarly, also Grumelli et al. [25] confirmed the stability of the SCV surface reporting an overpotential of 0.44 V. In less oxidizing potential conditions (but still in the OER regime), they also succeeded in stabilizing the unreconstructed DBT surface, for which they measured an overportential value of 0.49 V.

From the computational point of view and by means of DFT+U calculations, Righi et al. [84] have recently investigated the stability and the electrochemical performance towards OER for both SCV and DBT models of $Fe_3O_4(001)$ surface. First, they studied the interaction of these surface models with water molecules and their relative stability in an aqueous and electrochemical environment in a wide range of oxygen chemical potentials. Second, they proposed and investigated two different mechanisms for the OER taking place at the $Fe_3O_4(001)$ surface. One

mechanism is based on the conventional *adsorbate evolution mechanism* (AEM), which implies the O−O bond formation through the addition of a water molecule or a hydroxide ion (depending on the pH) on an oxo group. The other mechanism is based on the *lattice oxygen-mediated mechanism* (LOM), which involves oxygen atoms originally belonging to the oxide surface, rather than to the adsorbates, in the O−O bond formation. The two mechanisms were found to be competitive on both DBT and SCV surfaces. In 2014, Li and Selloni [284] performed a similar investigation on the DBT surface (SCV was proposed only few months later [79]), considering only the LOM mechanism, and obtained analogous results.

On the reconstructed $Fe_3O_4(001)$ surface, transition metal adatoms have been successfully isolated, exploting the presence of arrays of strongly binding sites (periodicity 0.84 nm along the [110] direction), on which metal atoms coordinate two surface lattice oxygen atoms [23, 58, 78, 79]. Transition metals are found to be stable against thermal sintering on Fe_3O_4, but some of them such as Ti [205], Mn [205], Co [205, 206], Ni [205, 207], Zr [205], Rh [208], Pd [285], and Ir [209], between room temperature and 500 K, tend to diffuse, and, in some cases, agglomerates in clusters or, in others, fill the Fe_{Oct} vacancies and become incorporated into the surface layers, leading to the restoring of a DBT-like surface structure. On the contrary, metals such as Cu [210], Ag [210, 211], Au [78, 79], and Pt [212, 213] do not become incorporated in the spinel lattice and remain stable as adatoms until the reconstruction is thermally lifted at 700 K.

Mixed Fe oxides being among the most promising materials for OER electrocatalysts [216–218, 280, 282, 283], with rather low overpotentials, one would reasonably expect that incorporating or loading as adatoms transition metal atoms at the $Fe_3O_4(001)$ surface, forming so-called *single-atom catalysts* (SACs), could improve the overall catalytic performance of magnetite. This is still an open question and whether having few transition metal adatoms on the surface would be as efficient as a mixed metal oxide is still to be proved. A recent experimental study on Ni-doped $Fe_3O_4(001)$ catalysts does not seem to corroborate this hypothesis for the case of Ni [26].

To the best of our knowledge, no theoretical mechanistic investigation has been yet presented elucidating the performance, together with the reaction pathways, of transition metal single atoms at the $Fe_3O_4(001)$ surface towards OER. Up to now, existing computational studies are limited to the investigation of pristine $Fe_3O_4(001)$ surface, as detailed above.

In this chapter, we present a thorough study, based on a wide set of hybrid density functional theory calculations (see Section 5.2 for the details on methods and models), where we investigate the potential of $Fe_3O_4(001)$-supported SACs as electrocatalytic systems for OER and use the pristine DBT $Fe_3O_4(001)$ surface as the reference system. Different mechanisms are considered as described

in Section 5.3. In Section 5.4, first, we assess the chosen computational setup by comparing our results on the pristine DBT $Fe_3O_4(001)$ surface with those already present in the literature [84, 284]. Second, we discuss structural, electronic and magnetic properties of isolated transition metal atoms (Ti, Co, Ni, and Cu) on the $Fe_3O_4(001)$ surface. In particular, Ti atoms are considered only when incorporated in the DBT-like surface model, because experiments indicate that they are not stable as adatoms, even at room temperature [205]. Co is studied both as adatom on an SCV surface model and as incorporated in the DBT-like surface model, in line with the experimental findings [205, 206]. Ni and Cu dopants are studied only as adatoms on the SCV surface model because Ni becomes incorporated only at a temperature higher than 415 K [205, 207], and Cu is not observed to become incorporated at any temperature where the SCV is stable [210]. Finally, for all the designed transition metal doped surface models, we analyze OER intermediates and reaction pathways, to evaluate their catalytic performance in terms of computed Gibbs free energy profiles and theoretical overpotentials. On the basis of these results, we will be able to establish whether small quantities of single atoms at the $Fe_3O_4(001)$ surface perform as good catalysts as mixed Fe oxides.

5.2 Methods and models

Hybrid DFT calculations (HSE06 [233, 240], see Section 2.1 for further details about the method) were carried out using the CRYSTAL17 package [247, 248] to study structural, electronic, magnetic, and thermodynamic properties of all systems under investigation. For the validation against experimental data of the standard hybrid functional HSE06 as a robust theoretical approach to describe structural, electronic, and magnetic properties of magnetite system, please refer to ref. [33] and corresponding Supporting Information, where the effect of reducing the fraction of the exact exchange was analyzed, in comparison with B3LYP calculations and PBE+U calculations with different U values. The Kohn-Sham orbitals were expanded in Gaussian-type orbitals: the all-electron basis sets are H-511G(p1), O-8411G(d1), (Ti, Fe, Co, Ni)-86411G(d41), and Cu-864111G(d41). The convergence criterion of 10^{-7} hartree and $4.5 \cdot 10^{-5}$ hartree/bohr for total energy and forces, respectively, were used during self-consistent field, geometry optimization, and vibrational frequencies calculations. For these calculations, the irreducible Brillouin zone was sampled with a $3 \times 3 \times 1$ k-points grid generated with the Monkhorst-Pack scheme [267]. For the calculation of the *projected density of states* (PDOS), a denser k-points mesh of $6 \times 6 \times 1$ was used. The PDOS were analyzed through the band center of mass (COM) descriptor, that was computed

using the formula:

$$band\ COM = \frac{\int_{-\infty}^{E_F} E\rho(E)dE}{\int_{-\infty}^{E_F} \rho(E)dE} \tag{5.1}$$

where E is the energy, E_F the Fermi energy (which is set to 0), and $\rho(E)$ the electronic density of states [250–252, 286].

Vibrational frequencies of each isolated molecule (H_2, O_2, and H_2O), isolated surface, and adsorbate bound to the surface were calculated at the Γ point within the harmonic approximation. To do so, numerical Hessian matrices were constructed from finite displacements and force components on each atom. The adsorbed intermediates, as well as the transition metal and oxygen atoms nearest to the intermediates themselves, were displaced by ±0.003 Å in all three Cartesian directions from their equilibrium positions. The resulting Hessian matrix then was diagonalized to yield vibrational frequencies corresponding to each mode. Enthalpic and entropic contributions were calculated at standard-state conditions using the ideal gas, rigid rotor, and harmonic approximation to evaluate respectively the translational, rotational, and vibrational terms for each isolated molecule (H_2, O_2, and H_2O), along with only vibrational terms for the isolated surface and adsorbate bound to the surface.

The OER Gibbs free energy profiles were derived within the framework of the *computational hydrogen electrode* (CHE) [220] using the *reversible hydrogen electrode* (RHE) at pH = 14 as reference [287]. The proton and electron Gibbs free energy $G(H^+ + e^-)$ can be rewritten as:

$$G(H^+ + e^-) = \frac{1}{2}G(H_2) - k_B T \cdot \mathrm{pH} \cdot \ln 10 - |e|U \tag{5.2}$$

where $G(H_2)$ is the Gibbs free energy of H_2, and $|e|U$ is the applied electrode potential per electron. Being at pH = 14, because experiments for the OER on Fe_3O_4 are conducted under very alkaline conditions [24–26], the release of H^+ and e^- is replaced by the consume of OH^- and the release of e^-, whose Gibbs free energy can be written as:

$$G(OH^- - e^-) = G(H_2O) - \frac{1}{2}G(H_2) + k_B T \cdot \mathrm{pH} \cdot \ln 10 + |e|U \tag{5.3}$$

where $G(H_2O)$ is the Gibbs free energy of H_2O and $G(OH^- - e^-)$ is the Gibbs free energy of the hydroxide ion and electron pair (the minus sign indicates that one species is consumed and the other is released). $G(H_2O)$ was computed at 0.035 bar because at this pressure, gas-phase water is in equilibrium with liquid water at 300 K, i.e., $G(H_2O_{liquid}) = G(H_2O_{gas,p=0.035bar})$ [220]. The theoretical overpotential (η) is defined for a given mechanism in which the most endoergic elementary step involves a redox reaction. It is calculated by subtracting the cumulative free

energies of all of the steps in the mechanism divided by the number of electrons involved (here, four), which gives the theoretical thermodynamic potential (U_0), from the potential of the most endoergic redox step. The onset potential (U^{onset}) is given by the sum of the overpotential and thermodynamic potential ($U^{onset} = U_0 + \eta$) and represents the minimum applied potential required to release the products.

Both DBT and SCV surface models [43, 79] were used to model pristine $Fe_3O_4(001)$ surfaces and were constructed as a (1×1) 17-layer slab with inversion symmetry, in line with previous works by our group [70, 243, 245]. The atoms in the central five layers of the slab were kept fixed to the bulk position, whereas the atoms in the other layers were fully relaxed. For the adsorption or incorporation of transition metal atoms and for the OER intermediates, atoms were put on both sides of the slab.

Incorporated Ti and Co atoms were modeled by substituting a Fe^{III}_{Oct} ion in the third layer of the DBT surface, as shown in the left panels of Figure 5.1(a). These models are named Ti_{in}@DBT and Co_{in}@DBT, respectively. Co, Ni, and Cu adatoms on the SCV surface were modeled as bound to two surface lattice oxygen atoms (see right panels in Figure 5.1(a)) which have been previously recognized to be the most reactive [78, 79, 254–256]. These models are named Co_{ad}@SCV, Ni_{ad}@SCV, and Cu_{ad}@SCV, respectively.

As an approximate description of the presence of the solvent, one dissociated water molecule was adsorbed on the slabs [284, 288]: the OH fragment was adsorbed on an exposed five-fold coordinated Fe^{III}_{Oct} (in the case of clean DBT, Ti_{in}@DBT and Co_{in}@DBT, left panels in Figure 5.1(b)) or on an adatom (in the case of Co_{ad}@SCV, Ni_{ad}@SCV, and Cu_{ad}@SCV, right panels in Figure 5.1(b)), whereas the H species was adsorbed on an exposed surface oxygen nearby. The adsorption energy (E_{Ads}) for the dissociated water molecule was calculated as follows:

$$E_{Ads} = E_{Total} - (E_{Surface} + E_{H_2O}) \tag{5.4}$$

where E_{Total} is the total energy of the whole system (surface and adsorbed water), $E_{Surface}$ the energy of the isolated $Fe_3O_4(001)$ surface, and E_{H_2O} the energy of one isolated water molecule.

5.3 Mechanism of OER on a metal oxide surface

As mentioned in the introduction, is it widely accepted that OER on a transition metal oxide can proceed through two different reaction paths: the conventional AEM and the LOM [289]. The AEM is typically assumed to involve four concerted *proton-coupled electron transfer* (PCET) reactions centered on the metal ion, and the O−O bond formation goes through the addition of a water molecule

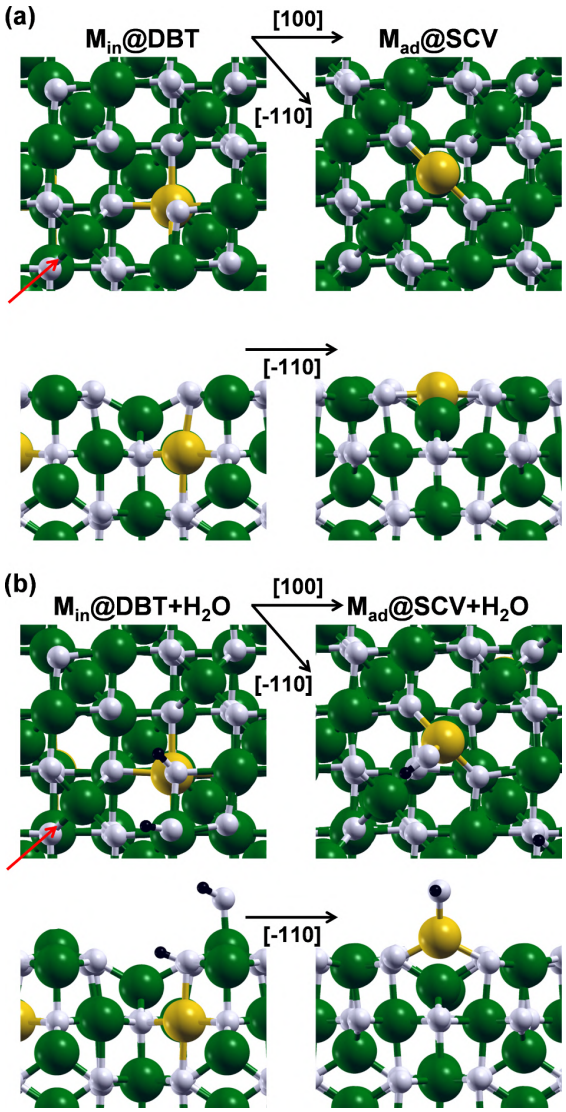

Figure 5.1: Top (first row) and side (second row) views of a transition metal atom incorporated in the DBT surface (on the left) and loaded as adatom on the SCV surface (on the right), in absence (a) and in presence (b) of a dissociated water molecule. The green, white, black, and yellow beads represent Fe, O, H, and doping transition metal atoms, respectively. For the left panels, M = Ti, Co. For the right panels, M = Co, Ni, Cu. The black arrows indicate the crystallographic directions, whereas the red arrows indicate the direction of the side views.

(in acidic environments) or a hydroxide ion (in alkaline environments) on an oxo group previously obtained from the deprotonation of an adsorbed water molecule or hydroxide ion [290–292]. Differently, the LOM may involve non-concerted proton-electron transfers and the reaction steps do not proceed only the metal site, as in the case of AEM, but they also involve oxygen atoms originally belonging to the oxide surface for the O−O bond formation [293, 294].

In this work, the AEM is studied according to the conventional scheme shown in Figure 5.2. The starting point is the OH adsorbed on an exposed metal site (A_1 in Figure 5.2) and the first step consists in its dehydrogenation. As a second step, the adsorbed O (A_2 in Figure 5.2) undergoes an addition by a hydroxide ion forming the hydroperoxo OOH (A_3 in Figure 5.2). As a third step, the adsorbed OOH is dehydrogenated to form the OO superoxo (A_4 in Figure 5.2) on the same metal site. As a fourth and final step, O_2 is released, and the catalyst is reestablished through the adsorption of a hydroxide ion on the metal site.

The LOM is studied according to the scheme proposed by Li and Selloni [284] for the $NiFe_2O_4(001)$ surface, as shown in Figure 5.2. The starting point is the OH group formed by the adsorption of the hydrogen dissociated from water to an oxygen of the surface (L_1 in Figure 5.2). The first step consists in the dehydrogenation of such OH, leading to L_2 in Figure 5.2. As a second step, the OO peroxo is formed within the surface lattice and, simultaneously, the OH adsorbed on an exposed five-fold coordinated Fe^{III}_{Oct} is hydrogenated to form a water molecule (L_3 in Figure 5.2). As a third step, this water molecule is dehydrogenated leading to L_4 in Figure 5.2. As a fourth and final step, the catalyst is restored through the adsorption of a hydroxide ion into the lattice oxygen vacancy left by the O_2 release. We wish to mention that, for both mechanisms, all the steps were treated as PCET reactions and different intermediates were investigated, but they resulted to be less favored than those just described.

In this chapter, the AEM is studied for all the models defined in the previous section. On the contrary, the LOM is investigated only for the DBT-based models. The reason for this choice will be discussed in detail below. The nomeclature is defined according to the following relus: the name starts with the type of mechanism (AEM or LOM), then proceeds with the surface model used (DBT or SCV or M_{in}@DBT or M_{ad}@SCV) followed by additional formula of -$MO_{nc}H$, where M indicates the metal atom where the OH species taking part to the OER is specifically adsorbed and the subscript nc defines the coordination number of the oxygen involved, i.e., $1c$ for an O atom in the hydroxide ion and $3c$ for a lattice oxygen. In the case of O_{1c}, the reaction proceeds via AEM, while in the case of O_{3c}, it proceeds via LOM.

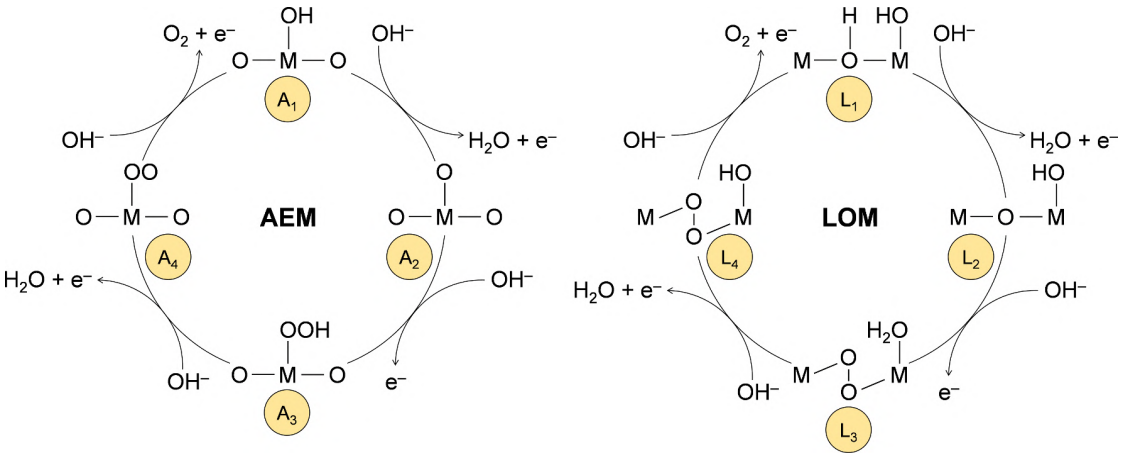

Figure 5.2: Schematic representation of the studied OER mechanisms, namely AEM on the left and LOM on the right.

5.4 Results and discussion

5.4.1 OER on clean DBT surface

Two mechanisms were investigated for the OER on a clean DBT surface. The first (namely, AEM[DBT-$FeO_{1c}H$]) involves an OH adsorbed on an exposed five-fold coordinated Fe^{III}_{Oct} and proceeds via the conventional AEM, whereas the second (namely, LOM[DBT-$FeO_{3c}H$]) involves an OH formed by the adsorption of a proton on a three-fold coordinated surface O atom and proceeds via the LOM. Figure 5.3 shows the structures of the intermediates and the energy profiles of the two reaction paths.

In the AEM[DBT-$FeO_{1c}H$] mechanism, the first step, i.e., the dehydrogenation of the adsorbed OH (A_1), consists in the formation of a O^- species (A_2) that is computed to hold a Mulliken spin density value of $-0.7\ \mu_B$ (compatible with one unpaired electron) and a Mulliken charge value that is half that of the hydroxyl O atom. After the addition of a hydroxide ion to the O^- species in the second step, a negatively charged hydroperoxo OOH intermediate is formed (A_3). It interacts also in a bridging fashion with another exposed five-fold coordinated Fe^{III}_{Oct} in the surroundings. The OOH oxygen atoms holds no spin density and Mulliken charge values similar to that of the O^- species and the O−O bond length is 1.46 Å, in line with the features of a peroxo species. The third step, i.e., the dehydrogenation of the hydroperoxo, leads to a superoxo OO intermediate that bridges two exposed five-fold coordinated Fe^{III}_{Oct} (A_4). Each of the OO oxygen atoms has a Mulliken spin density value of $-0.4\ \mu_B$ (compatible with an overall unpaired electron) and a Mulliken charge value which is half that of the O^- species. Furthermore, this third

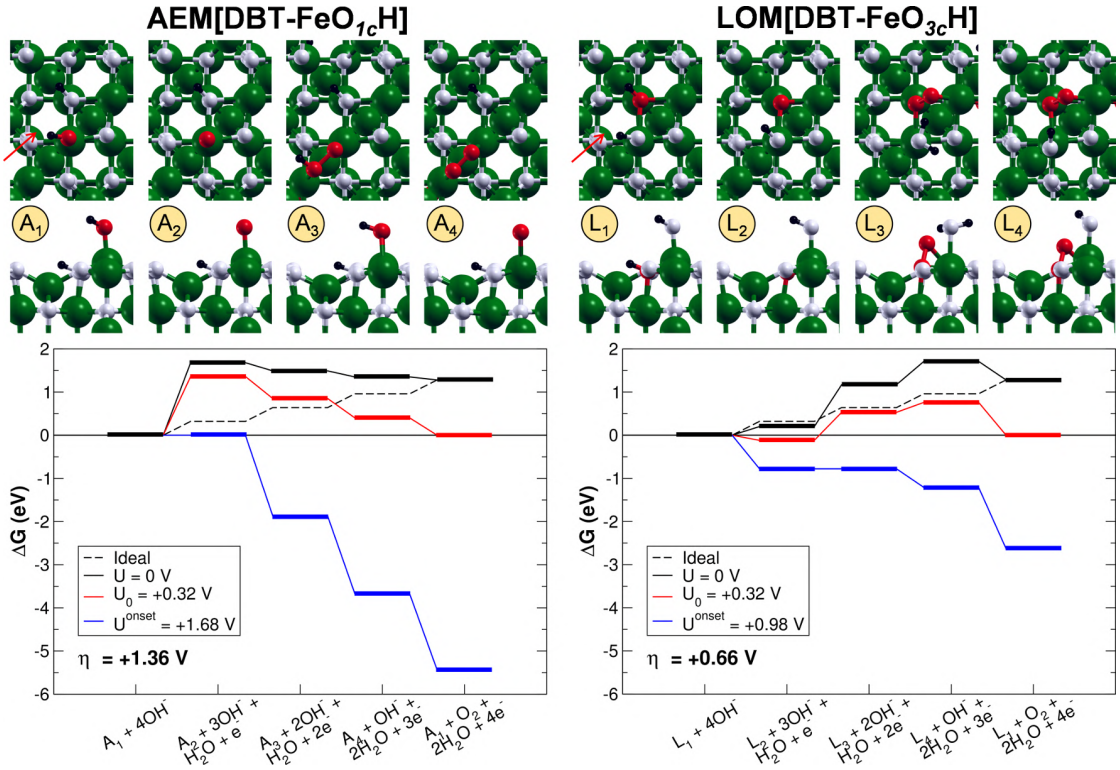

Figure 5.3: Top (first row) and side (second row)) views of the intermediates and energy profiles of the AEM[DBT-FeO_{1c}H] and LOM[DBT-FeO_{3c}H] OER pathways. The intermediates are labeled as in Figure 5.2. The green, black, white, and red beads represent Fe, H, O and O involved in the OER intermediates, respectively. The orientation of the crystallographic directions is the same as in Figure 5.1. The red arrows indicate the direction of the side views.

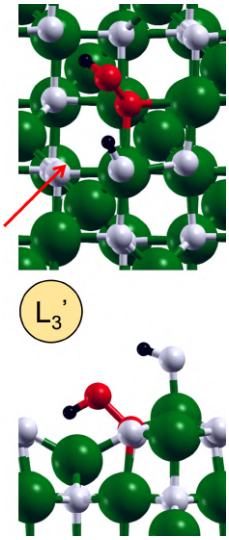

Figure 5.4: Top and side view of the hydroperoxo OOH intermediate as proposed by Righi et al. [84] for the LOM[DBT-$FeO_{3c}H$] OER pathway. The intermediate is labeled according to Figure 5.2. The green, black, white, and red beads represent Fe, H, O and O involved in the OER intermediates, respectively. The orientation of the crystallographic directions is the same as in Figure 5.1. The red arrow indicates the direction of the side view.

step causes a shortening of the O−O bond length to a value of 1.32 Å, which is a definitive proof of the transition from peroxo to superoxo. Finally, in the fourth step, the catalyst is regenerated and one gaseous O_2 molecule is released.

The most energetically demanding step of the overall reaction, i.e., the PDS, is the first step with an overpotential η of 1.36 V. Here, the dehydrogenation of the adsorbed OH leads to the formation of the O^- species, which is found to be highly unstable with respect to the other intermediates. Such high instability can be justified by the fact that the O^- species in the model is not stabilized by any interaction with the surface, whereas the successive intermediates interact with superficial five-fold coordinated Fe^{III}_{Oct}. Righi et al. [84] found the same step to be the PDS, but with a smaller overpotential of 0.67 V. This discrepancy could be due to the fact that, in their study, the oxo species is stabilized by the presence of both implicit and explicit aqueous solvent. Moreover, the theoretical description of the Fe^{III}-O^- pair is a sensitive issue, which depends on the computational method adopted (in particular, the percentage of exact exchange in the hybrid functional, as discussed by Righi et al. [295]), and may affect the energetics of the reaction.

In the LOM[DBT-$FeO_{3c}H$] mechanism, the first step consists in the dehydrogenation of the OH group formed by the adsorption of the dissociated proton from water on a surface oxygen ($L_1 \rightarrow L_2$). In this case, no O^- species is formed because

the electron to be extracted is removed from one Fe^{II} deep in the Fe_3O_4 slab and not from the surface oxygen. The oxidation of one Fe^{II} ion is confirmed by the increase in its Mulliken spin density and charge (from 3.7 to 4.2 μ_B and from 1.9 to 2.2, respectively). In the second step, the peroxo OO intermedate is formed inside the magnetite lattice and, at the same time, a proton transfer to the OH on a five-fold coordinated Fe^{III}_{Oct} takes palce leading to an adsorbed undissociated a water molecule (L_3). The initial amount of Fe^{II} ions is now restored in the surface. The OO oxygen atoms have no significant spin density and Mulliken charge values are half those of the OH group, a O−O bond length is of 1.47 Å, in line with the features of a peroxo species. We have also investigated a different intermediate structure at this step of reaction, as proposed by Righi et al. in Reference [84], where a hydroperoxo OOH species is formed through the binding of a hydroxide ion to a surface oxygen (see Figure 5.4). This alternative intermediate is, however, much less stable, probably because the surface O atom acquires a four-fold coordination, which is not compatible with a -I oxidation state. As a third step, the adsorbed water molecule in the most stable L_3 intermediate is dehydrogenated. Again, a hydroxide ion is formed, and the electron is removed from one Fe^{II} deep in the Fe_3O_4 slab model. The peroxo OO intermediate is not affected by this reaction, as confirmed by the Mulliken spin density and charge values. Finally, in the fourth step, the catalyst is regenerated and one gaseous O_2 molecule is released.

The PDS of the LOM reaction path is the second step with an overpotential η of 0.66 V. The formation of the peroxo OO intermedate inside the lattice is reasonably the most energetically demanding step because it implies the intercalation of one oxygen atom in the Fe_3O_4 lattice. An overpotential of 0.66 V is in line with the values reported in the computational literature for bare magnetite [84, 284], as discussed above.

5.4.2 Incorporated Ti and Co in DBT surface

Incorporated Ti and Co atoms (namely, Ti_{in}@DBT and Co_{in}@DBT) were studied through the substitution of one Fe^{III}_{Oct} ion in the third layer of the DBT surface slab model, as represented in the left panels of Figure 5.1(a). For both metals, different electronic configurations were investigated by varying the overall magnetization of the system. Only the lowest-energy spin configurations are reported and discussed below.

Ti is found to be in the +IV oxidation state (d^0), in line with the absence of spin density. The substitution of one Fe^{III} with one Ti^{IV} causes the reduction of one neighboring Fe^{III} ion to Fe^{II} in order to keep the charge neutrality of the system (i.e., one Fe^{III}-Fe^{III} pair is substituted by one Ti^{IV}-Fe^{II} pair). The appearance of an additional Fe^{II} ion in the slab model is confirmed by the reduction of the Mulliken spin density and charge (from 4.2 to 3.7 μ_B and from 2.2 to 1.9, respectively) on

that Fe site. Another configuration with Ti^{III} (d^1) is also found. The Ti atom is characterized by a Mulliken spin density of +0.9 μ_B, indicating the presence of one unpaired electron, and a reduced Mulliken charge with respect the Ti^{IV} one. Here, none of the Fe^{III} ions is reduced to Fe^{II}. However, this alternative spin configuration is higher in energy by ∼0.7 eV, therefore we did not further consider it in the following for the OER investigation.

Co is found to be in the +II oxidation state (d^7) in the high spin configuration, as demonstrated by a Mulliken spin density value of +2.7 μ_B, compatible with three parallel (spin-up) unpaired electrons. The substitution of one Fe^{III} with one Co^{II} causes the oxidation of one neighboring Fe^{II} ion to Fe^{III} in order to keep the charge neutrality of the system (with the net effect of exchanging one Fe^{II} ion with one Co^{II}). The oxidation of one Fe^{II} ion is confirmed by the increase in its Mulliken spin density and charge values (from 3.7 to 4.2 μ_B and from 1.9 to 2.2, respectively). Another configuration with low spin Co^{III} (d^6) is also found. No significant spin density is observed on the Co atom, whose Mulliken charge is higher with respect to that of Co^{II}. None of the Fe ions are involved in any change of oxidation state. The Co^{III} configuration being higher in energy by ∼1.4 eV, it will not be further considered in the following for the OER investigation.

5.4.3 OER on DBT surface incorporating Ti and Co

As already done for the pristine DBT surface, two mechanisms were investigated for the OER on Ti_{in}@DBT and Co_{in}@DBT. The first mechanism (namely, AEM[Ti_{in}@DBT-FeO_{1c}H] and AEM[Co_{in}@DBT-FeO_{1c}H]) involves an OH adsorbed on an exposed five-fold coordinated Fe^{III}_{Oct} and proceeds via the conventional AEM, whereas the second (namely, LOM[Ti_{in}@DBT-TiO_{3c}H], LOM[Ti_{in}@DBT-FeO_{3c}H], and LOM[Co_{in}@DBT-CoO_{3c}H]) involves an OH formed by the adsorption of a proton from water dissociation on a surface oxygen and proceeds via the LOM. The Ti_{in}@DBT-TiO_{3c}H and Ti_{in}@DBT-FeO_{3c}H cases differ only in the coordination sphere of the OH, which is the starting point of the reaction: in LOM[Ti_{in}@DBT-TiO_{3c}H], the OH is directly bonded to the Ti^{IV} ion, whereas in LOM[Ti_{in}@DBT-FeO_{3c}H], it is only coordinated to Fe ions. In Figure 5.5 and Figures 5.6 and 5.7, the structures of the intermediates and the energy profiles of the first and the second type of mechanism are reported, respectively.

First, the AEM[Ti_{in}@DBT-FeO1cH] and AEM[Co_{in}@DBT-FeO1cH] reaction pathways are analyzed (see Figure 5.5). The OER is found to proceed through the same intermediates that were characterized above for the clean DBT surface. The formation of the O^- species (with Mulliken spin density values of -0.7 μ_B) is followed by that of the hydroperoxo OOH species (oxygen atoms with no spin density and Mulliken charge values like that of the O^- species). The subsequent formation of the superoxo OO through the dehydrogenation of OOH shortens the O−O

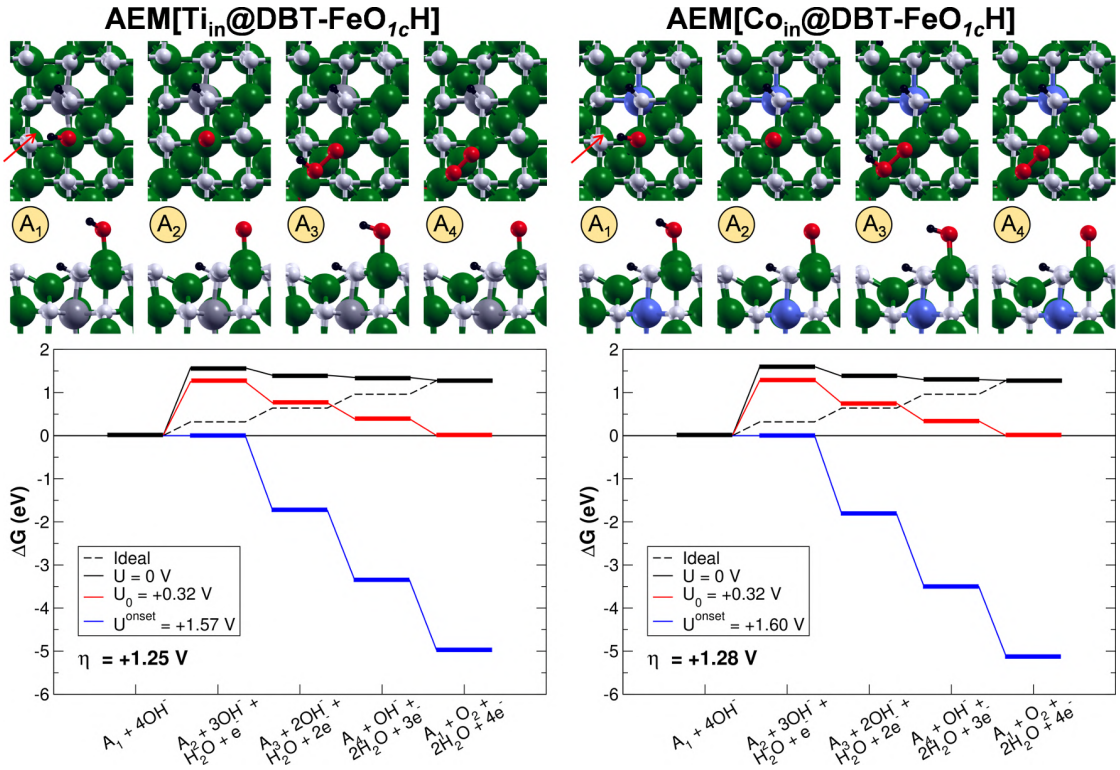

Figure 5.5: Top (first row) and side (second row) views of the intermediates and energy profiles of the AEM[Ti$_{in}$@DBT-FeO$_{1c}$H] and AEM[Co$_{in}$@DBT-FeO$_{1c}$H] OER pathways. The intermediates are labeled as in Figure 5.2. The green, black, white, red, grey, and blue beads represent Fe, H, O, O involved in the OER intermediates, Ti, and Co respectively. The orientation of the crystallographic directions is the same as in Figure 5.1. The red arrows indicate the direction of the side views.

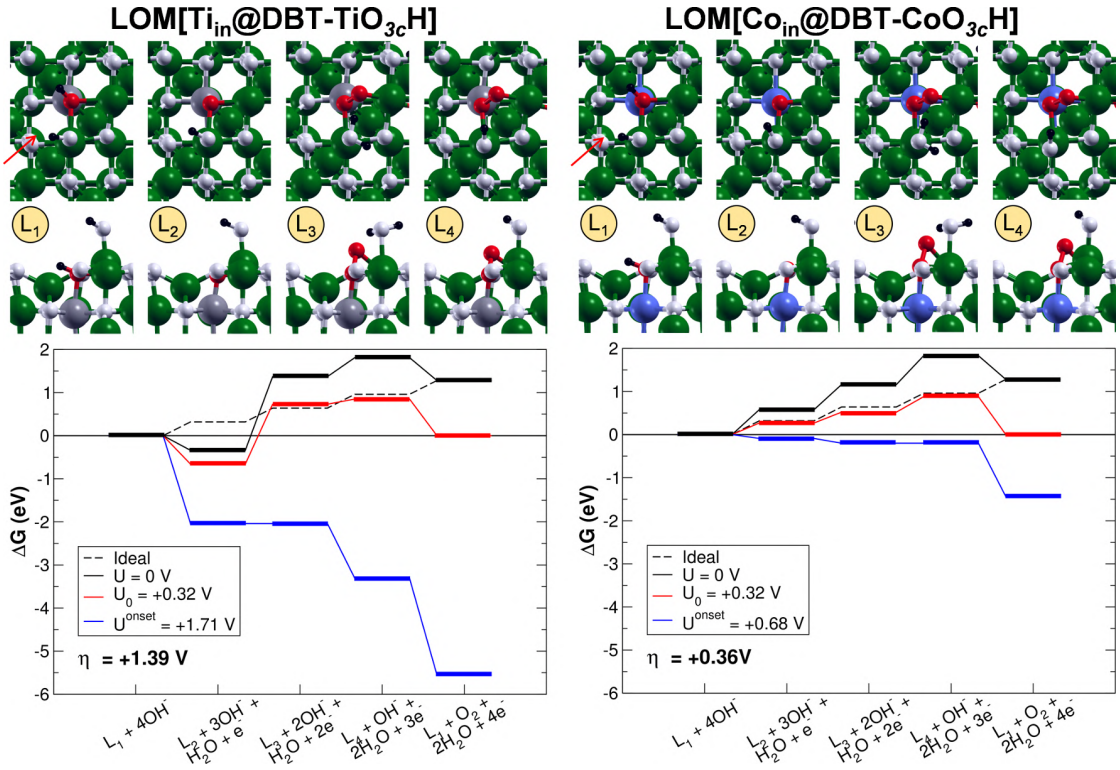

Figure 5.6: Top (first row) and side (second row) views of the intermediates and energy profiles of the LOM[Ti_{in}@DBT-TiO_{3c}H] and LOM[Co_{in}@DBT-CoO_{3c}H] OER pathways. The intermediates are labeled as in Figure 5.2. The green, black, white, red, grey, and blue beads represent Fe, H, O, O involved in the OER intermediates, Ti, and Co respectively. The orientation of the crystallographic directions is the same as in Figure 5.1. The red arrows indicate the direction of the side views.

bond from 1.46 to 1.32 Å. Each of the OO oxygen atoms holds a Mulliken spin density value of $-0.4\ \mu_B$ (AEM[Ti_{in}@DBT-FeO1cH]) and $+0.6\ \mu_B$ (AEM[Co_{in}@DBT-FeO_{1c}H]), which is compatible with one overall unpaired electron on the superoxo OO group, and a Mulliken charge value that is half that of the O^- species. For both AEM[Ti_{in}@DBT-FeO1cH] and AEM[Co_{in}@DBT-FeO_{1c}H], the OOH and OO fragments bind in a bridging fashion with exposed five-fold coordinated Fe^{III}_{Oct} ions in the surroundings, as observed for the clean DBT surface.

Also the energetics seems not to be significantly affected by the presence of the dopants. As in the case of AEM[DBT-FeO_{1c}H], the PDS is the first step, i.e., dehydrogenation of the adsorbed OH, with overpotential values of 1.25 and 1.28 V for AEM[Ti_{in}@DBT-FeO_{1c}H] and AEM[Co_{in}@DBT-FeO_{1c}H], respectively, similar to that found for the clean DBT (1.36 V).

Thus, the incorporation of Ti and Co in the third layer of the Fe_3O_4(001) surface (Ti_{in}@DBT and Co_{in}@DBT) does not affect the AEM for the OER, either in structural or energetic features. On the contrary, when incorporated dopants are directly involved in the OER intermediates, the energetics of the reaction is noticeably changed, as detailed below.

The LOM[Co_{in}@DBT-CoO_{3c}H], LOM[Ti_{in}@DBT-TiO_{3c}H] (see Figure 5.6), and LOM[Ti_{in}@DBT-FeO_{3c}H] (see Figure 5.7) pathways are analyzed. Again, the OER is found to proceed through the same intermediates as found for the clean DBT surface above. The deprotonation of the lattice OH and the concomitant oxidation of one Fe^{II} are followed by the formation of the peroxo OO species inside the surface lattice. Subsequent proton and electron exchanges lead to the release of one gaseous O_2 molecule and regeneration of the catalyst. In all cases, the OO oxygen atoms have no significant spin density, Mulliken charge values are half those of the O atom in the OH group and the O−O bond length is of 1.47 Å, in line with the features of a peroxo species. The mechanism via the formation of the alternative intermediate, i.e., a lattice hydroperoxo, has also been evaluated, but again it is found to be very unstable as for the LOM[DBT-FeO_{3c}H] case.

If the presence of the dopants does not affect the intermediates and their structure, we cannot state the same regarding the energetics for the reaction profiles in the case of LOM[Ti_{in}@DBT-TiO_{3c}H] and LOM[Co_{in}@DBT-CoO_{3c}H]. Only for LOM[Ti_{in}@DBT-FeO_{3c}H] we observe almost identical results as for the bare surface: the PDS is the formation of the peroxo OO intermediate inside the lattice with an overpotential of 0.64 V (versus 0.66 V for the clean DBT). This is due to the fact that the lattice OH — which is the starting point for the OER — and the other intermediates are coordinated only to Fe ions, as in the case of the clean surface. On the contrary, for LOM[Ti_{in}@DBT-TiO_{3c}H], the same PDS is characterized by a large increase in the overpotential value up to 1.29 V. From Figures 5.6 and 5.7 it may seem that this is due to an additional stabilization

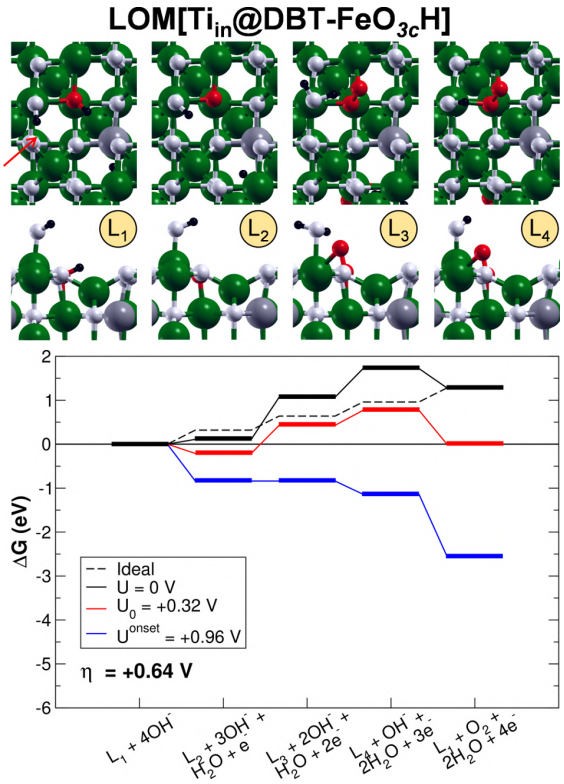

Figure 5.7: Top (first row) and side (second row) views of the intermediates and energy profiles of the LOM[Ti_{in}@DBT-FeO_{3c}H] OER pathway. The intermediates are labeled as in Figure 5.2. The green, black, white, red, and grey beads represent Fe, H, O, O involved in the OER intermediates, and Ti, respectively. The orientation of the crystallographic directions is the same as in Figure 5.1. The red arrow indicates the direction of the side views.

of the oxo O intermediate in LOM[Ti_{in}@DBT-TiO_{3c}H], but this is not the actual reason. All the other intermediates in LOM[Ti_{in}@DBT-TiO_{3c}H] are destabilized with respect to their equivalent in LOM[Ti_{in}@DBT-FeO3cH] (compare Figures 5.6 and 5.7), whereas the oxo O one is almost energetically equivalent. Such behavior may suggest that OH and OO intermediates have a lower affinity with Ti than with Fe.

Interestingly, in the case of LOM[Co_{in}@DBT-CoO_{3c}H], the PDS is the third step, which corresponds to the dehydrogenation of the water molecule adsorbed on an exposed five-fold coordinated $Fe^{III}_{O}ct$, with an overpotential of 0.36 V. The promising energy profile associated to this mechanism could be related to the good affinity between OER intermediates and Co, whose oxophilicity — especially when involved in Fe alloys — is well-known. Indeed, mixed Fe-Co oxides and oxyhydroxides are some of the most promising materials for OER electrocatalysts [216–219, 280, 282, 283].

5.4.4 Co, Ni, and Cu adatoms on SCV

Co, Ni, and Cu adatoms (namely, Co_{ad}@SCV, Ni_{ad}@SCV, and Cu_{ad}@SCV) were studied by binding them with two lattice O atoms of the SCV surface, as represented in the right panels of Figure 5.1(a). Different electronic and spin configurations were investigated by varying the overall magnetization of the system. Only the lowest-energy configurations are reported and discussed in the following.

Similarly to the what was observed when Co was incorporated in the magnetite lattice in previous sections, Co adatom preferentially adopts the +II oxidation state (d^7) in the high spin configuration, as confirmed by the Mulliken spin density value of +2.5 μ_B, compatible with the three parallel unpaired electrons with respect to the aligned lattice Fe_{Oct} ions. For the charge neutrality of the system, the oxidation of the Co adatom to the +II oxidation state must be compensated by the reduction of two Fe^{III} ions, which is confirmed by the reduction of their Mulliken spin density and charge (from 4.2 to 3.7 μ_B and from 2.2 to 1.9, respectively). The spin flip of the Co^{II} unpaired electrons from a parallel to an antiparallel spin configuration with respect to the aligned lattice Fe_{Oct} (Mulliken spin density value from +2.5 to −2.6 μ_B) is found to be slightly unfavored of $\sim$ 0.1 eV. We notice that water dissociation on the surface inverts this tendency by stabilizing the antiparallel configuration, which will be considered when we compute the reaction energy profile for OER in the next section. We could also localize the high and low spin configurations for Co^{I} (d^8), but they are unfavored by $\sim$ 0.2 and $\sim$ 1.2 eV, respectively. In these cases, the Co center is characterized by Mulliken charges smaller than Co^{II} one and Mulliken spin densities of −1.8 μ_B and 0.1 μ_B, respectively.

Differently from Co, Ni adatom prefers the +I oxidation state ($3d^8 4s^1$) in the low spin configuration, as confirmed by the Mulliken spin density value of -1.0

μ_B, compatible with one antiparallel unpaired electron with respect to the aligned lattice Fe_{Oct} ions. Notice that the parallel configuration is $\sim$ 0.1 eV higher in energy. The presence of the adatom in its +I oxidation state implies the reduction of one Fe^{III} ion, which is confirmed by a lower Mulliken spin density and charge. A high spin Ni^{II} (d^8) configuration (with two antiparallel unpaired electrons and Mulliken spin density of -1.7 μ_B) is also found, although it is unfavored by $\sim$ 0.2 eV. However, after water dissociation on the surface (see Figure 5.1(b)), only Ni^{II} species could be localized and, thus, it will be used in the next section as a staring point for the OER reaction paths.

Like Ni, Cu prefers the +I oxidation state (d^{10}), as proved by the absence of significant spin density. One Fe^{III} ion in the slab model becomes reduced to Fe^{II} in order to keep the charge neutrality of the system. After heterolytic water dissociation, the Cu is further oxidized to the +II oxidation state and one more Fe^{III} ion in the slab is reduced. This species, i.e., Cu^{II} in d^9 configuration with one antiparallel unpaired electron with respect to the aligned lattice Fe_{Oct} ions (Mulliken spin density of -0.6 μ_B), will be further considered as the starting point of the OER investigation.

5.4.5 OER on Co, Ni, and Cu adatoms on SCV

For the OER on Co_{ad}@SCV, Ni_{ad}@SCV, and Cu_{ad}@SCV catalysts, only the conventional AEM mechanism was investigated (namely, AEM[Co_{ad}@SCV-CoO_{1c}H], AEM[Ni_{ad}@SCV-NiO_{1c}H], and AEM[Cu_{ad}@SCV-CuO_{1c}H]), starting from an OH species adsorbed on the metal adatoms. In Figures 5.8, 5.9, and 5.10, the structures of the intermediates and the energy profiles of these OER pathways are reported. The LOM mechanism was not considered for these systems because the OER intermediates in LOM would not directly involve the metal adatoms. As a consequence of this, it is reasonable to expect similar results compared to those found for the clean surface (LOM[DBT-FeO_{3c}H]), as also observed for AEM[Co_{in}@DBT-FeO_{1c}H], AEM[Ti_{in}@DBT-FeO_{1c}H], and LOM[Ti_{in}@DBT-FeO_{3c}H], whose reaction intermediates did not directly interact with the dopants and whose results are almost identical to those of the bare surface (AEM[DBT-FeO_{1c}H] and LOM[DBT-FeO_{3c}H], respectively).

The reaction intermediates via AEM[Co_{ad}@SCV-CoO_{1c}H] (see Figure 5.8), AEM[Ni_{ad}@SCV-NiO_{1c}H] (see Figure 5.9), and AEM[Cu_{ad}@SCV-CuO_{1c}H] (see Figure 5.10) pathways are the same as for the DBT-based electrocatalyst models, i.e., AEM[DBT-FeO_{1c}H], AEM[Ti_{in}@DBT-FeO_{1c}H], and AEM[Co_{in}@DBT-FeO_{1c}H]. The O^- species, formed by the dehyrogenation of the OH group on the metal adatom, is attacked by a hydroxide ion to generate the hydroperoxo OOH fragment. The O^- species are characterized by Mulliken spin densities of $-1.1/-1.2$ μ_B, whereas the OOH oxygen atoms have no significant Mulliken spin density and Mulliken charges similar to those of the O^- species. In the AEM[Ni_{ad}@SCV-NiO_{1c}H] and AEM[Cu_{ad}@SCV-CuO_{1c}H] cases, the OOH fragment interacts through a weak hydrogen bond (bond length of 1.8 Å, and bond angle of 130° and 145°, respectively) with a surface oxygen, whereas for AEM[Co_{ad}@SCV-CoO_{1c}H] it does not. As a third step, the dehydrogenation of the hydroperoxo OOH leads to the superoxo OO species with a shortening the O−O bond length from 1.48, 1.46, and 1.43 to 1.35, 1.32, and 1.30 Å, for AEM[Co_{ad}@SCV-CoO_{1c}H], AEM[Ni_{ad}@SCV-NiO_{1c}H], and AEM[Cu_{ad}@SCV-CuO_{1c}H], respectively. In the case of Co and Ni, a side-on superoxo is formed: the unpaired electron is equally shared between the two oxygen atoms, as confirmed by the Mulliken spin densities of -0.6 μ_B for each of them. In the case of Cu, an end-on superoxo species is formed: the unpaired electron is more localized on the oxygen atom bonded to the Cu adatom (Mulliken spin density of -0.7 versus -0.5 μ_B for the terminal oxygen atom) resulting in a more negative Mulliken charge on the terminal oxygen atom.

Although the reaction intermediates are the same as on the pristine surface, the energetics is largely affected by the presence of the adatoms. The PDS is still identified for all the systems with the oxo O^- formation but the overpotential is reduced with respect to the other systems investigated for the OER via AEM

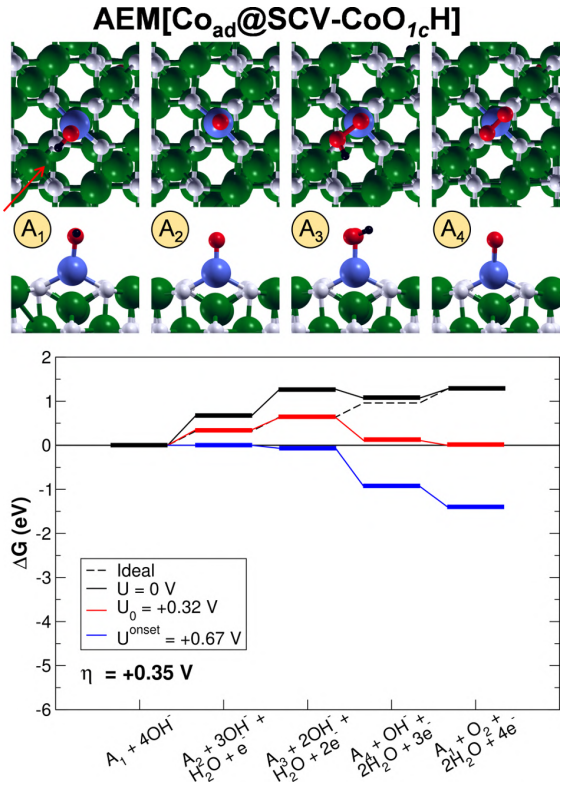

Figure 5.8: Top (first row) and side (second row) views of the intermediates and energy profiles of the AEM[Co_{ad}@SCV-CoO_{3c}H] OER pathway. The intermediates are labeled as in Figure 5.2. The green, black, white, red, and blue beads represent Fe, H, O, O involved in the OER intermediates, and Co, respectively. The orientation of the crystallographic directions is the same as in Figure 5.1. The red arrow indicates the direction of the side views.

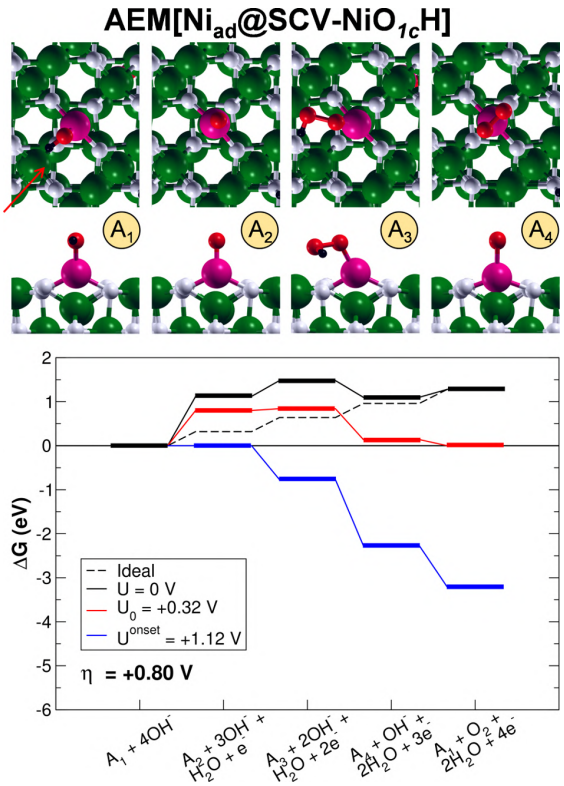

Figure 5.9: Top (first row) and side (second row) views of the intermediates and energy profiles of the AEM[Ni_{ad}@SCV-NiO_{3c}H] OER pathway. The intermediates are labeled as in Figure 5.2. The green, black, white, red, and pink beads represent Fe, H, O, O involved in the OER intermediates, and Ni, respectively. The orientation of the crystallographic directions is the same as in Figure 5.1. The red arrow indicates the direction of the side views.

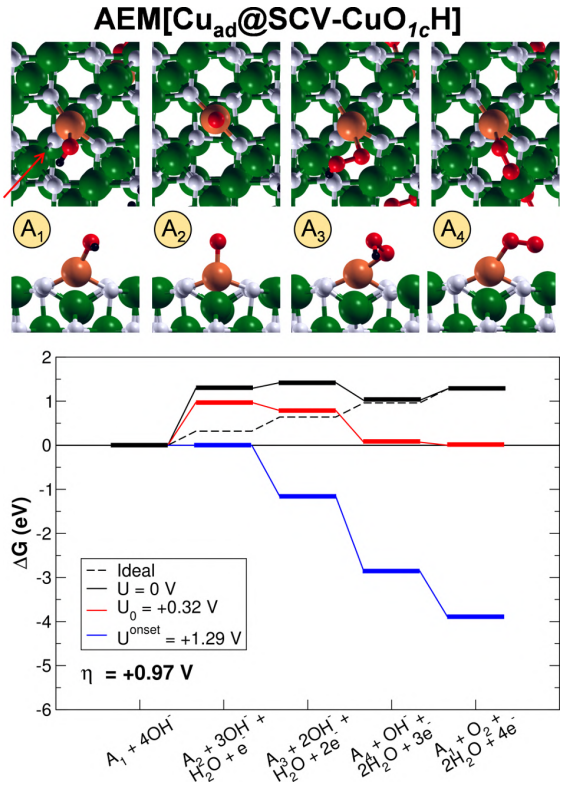

Figure 5.10: Top (first row) and side (second row) views of the intermediates and energy profiles of the AEM[Cu_{ad}@SCV-CuO_{3c}H] OER pathway. The intermediates are labeled as in Figure 5.2. The green, black, white, red, and brown beads represent Fe, H, O, O involved in the OER intermediates, and Cu, respectively. The orientation of the crystallographic directions is the same as in Figure 5.1. The red arrow indicates the direction of the side views.

(namely, AEM[DBT-FeO_{1c}H], AEM[Ti_{in}@DBT-FeO_{1c}H], and AEM[Co_{in}@DBT-FeO_{1c}H)]. In particular, η values are 0.35, 0.80, and 0.97 eV for AEM[Co_{ad}@SCV-CoO_{1c}H], AEM[Ni_{ad}@SCV-NiO_{1c}H], and AEM[Cu_{ad}@SCV-CuO_{1c}H], respectively. Despite mixed Fe-Ni and Fe-Co oxides are both excellent OER electrocatalysts [216–218, 280, 282, 283], here only Co adatoms are found to improve significantly the catalytic performance of magnetite towards OER with respect to the clean surface. Ni adatoms present high overpotentials, in agreement with recent experimental findings [26].

As in the case of OER via LOM (LOM[Co_{in}@DBT-CoO_{3c}H]), the Co-doped system is the best performing also via AEM (AEM[Co_{ad}@SCV-CoO_{1c}H]). These results could be due to the good affinity (neither too strong nor too weakly bound) between the OER intermediates and Co. To give ground to this thesis, adsorption energies (E_{Ads}) were computed for the dissociative adsorption of one water

molecule on Co_{ad}@SCV, Ni_{ad}@SCV, and Cu_{ad}@SCV. The adsorption of OH on Co is more favored than on Ni and Cu (−0.79 versus −0.58 eV, respectively), in line with the statement above.

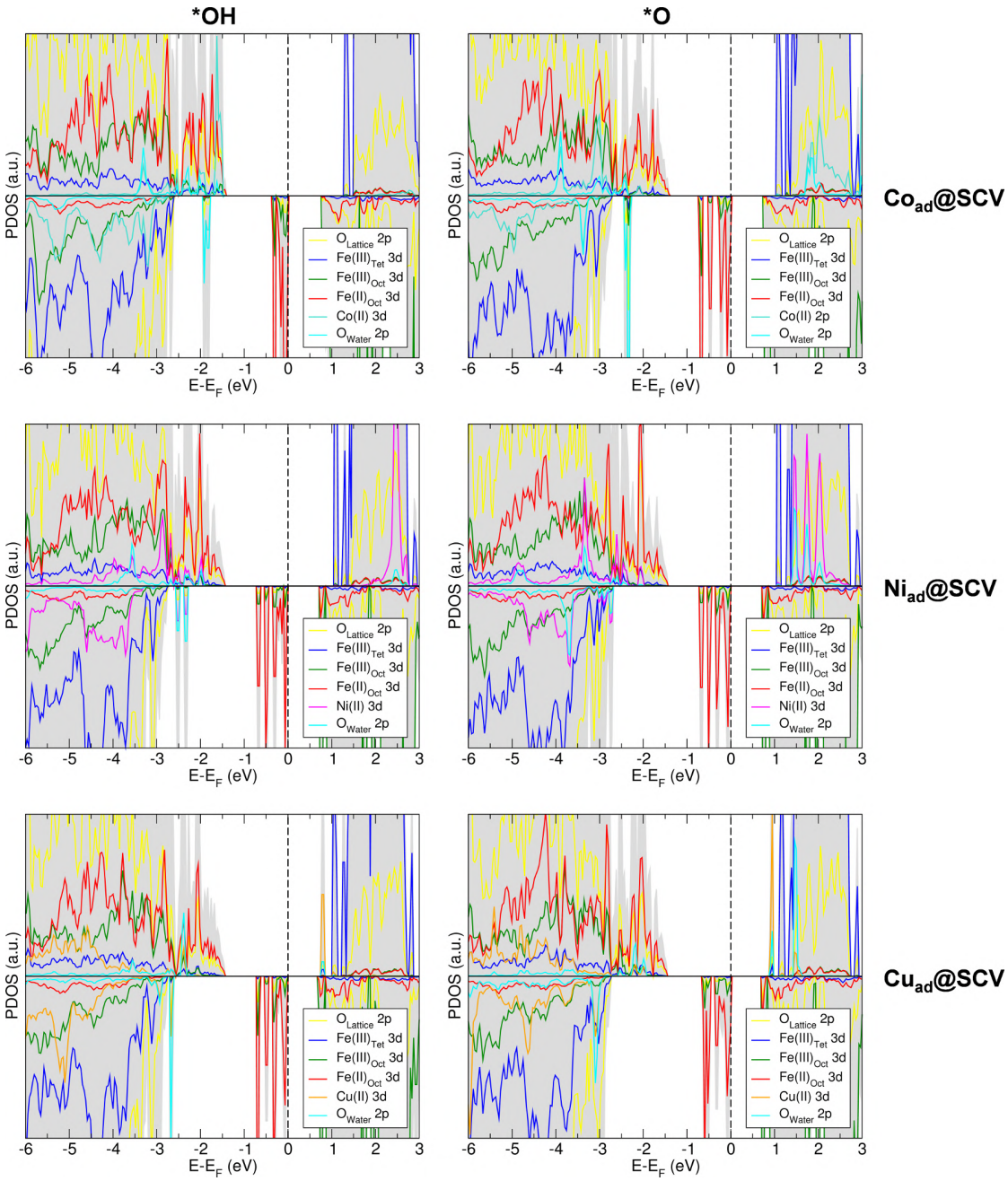

Figure 5.11: PDOS of the OH and O intermediates on the Co_{ad}@SVC than Ni_{ad}@SCV and Cu_{ad}@SCV model electrocatalysts.

Furthermore, the O^- species — whose formation corresponds to the PDS — is more stable on the Co adatom rather than on Ni and Cu adatoms, while the energetics of the other intermediates is similar on all three adatoms, as suggested by the OER profiles shown in Figure 5.8, 5.9, and 5.10. To understand this trend, the electronic structures of the species under investigation were computed and analyzed. In Figure 5.11, the PDOS of the OH and O intermediates for the AEM[Co_{ad}@SCV-$CoO_{1c}H$], AEM[Ni_{ad}@SCV-$NiO_{1c}H$], and AEM[Cu_{ad}@SCV-$CuO_{1c}H$] OER pathways are shown, where the cyan curves represent the $2p$ states of the oxygen of the adsorbed intermediates (originated from the dissociative adsorption of one water molecule). These states are partially left empty in the alpha channel when OH is dehydrogenated to form the O^- species, as proven by the appearance of $2p$ states in the conduction band (alpha channel) of the O intermediates. The $2p$ states of the OH oxygen are closer to the Fermi energy for Co_{ad}@SVC than Ni_{ad}@SCV and Cu_{ad}@SCV, as confirmed by the computed $2p$-band COM values of -4.2, -4.7 and -4.9 eV, respectively. These descriptors indicate that $2p$ states are more easily depleted, leading to a more stable subsequent O^- intermediate, when the OH species is adsorbed on the Co adatom.

5.5 Conclusions

In this hybrid DFT study, we performed a comparative investigation of the OER on pristine and metal-doped $Fe_3O_4(001)$ model electrocatalysts.

For the clean $Fe_3O_4(001)$ DBT surface, two OER mechanisms were investigated: the LOM and the conventional AEM. As regards the pathway based on the LOM (i.e., involving a surface oxygen atom of the magnetite lattice), the OER proceeds through the intermediates proposed for $NiFe_2O_4(001)$ by Li and Selloni [284], giving an overpotential value of 0.66 V, which is similar to that computed by Righi et al. [84], even if for a slightly different pathway. As regards the pathway based on the AEM (i.e., involving the oxygen of the adsorbed hydroxide), a high overpotential value of 1.36 V is found, due to the highly unstable oxo O^- species.

The metal-doped $Fe_3O_4(001)$ systems were investigated considering both (i) metal atom incorporation in a subsurface vacancy in the third layer (Ti and Co) or (ii) metal deposition as adatom on the surface (Co, Ni, and Cu). When metal atoms are incorporated in the lattice, results are similar to those observed for the clean surface, expect when a direct bond between the reaction intermediates and metal is established. Indeed, conventional AEM-based OER pathways on Ti_{in}@DBT and Co_{in}@DBT give almost identical results to those for the clean DBT. On the contrary, LOM-based OER results on the same systems are affected by the dopants: Ti-incorporated magnetite presents an increased overpotential (η = 1.39 V), whereas Co-incorporated a reduced one (η = 0.36 V), as compared

with the clean DBT ($\eta = 0.66$ V). In the case of metal adatoms deposited on the surface, the Co-loaded system is found to be the most promising for the OER with a reasonably low oveportential ($\eta = 0.35$ V), whereas Ni and Cu do not improve the performance with respect the clean surface ($\eta = 0.80$ and 0.97 V, respectively).

To summarize, transition metal atoms affect the electrocatalytic performance of magnetite only when they are directly involved in the formation of intermediates through chemical bonds, i.e., metal dopants do not exercise any significant proximity or long range effects able to affect the OER energetics. In particular, Co-doped systems (Co_{in}@DBT and Co_{ad}@SCV), independent of whether the Co is *incorporated in* or *deposited on* the surface, are found to be the most promising electrocatalysts among those investigated in this study, due to the well-balanced affinity between the transition metal atom and the OER intermediates, leading to a decrease in the OER overpotential value of ca 0.3 eV with respect to the clean magnetite surface.

To conclude, the large set of data reported in this study has proven that both transition metal atoms loading on or incorporating in the magnetite surface could be successful strategies to improve its electrocatalytic activity for the OER. However, the doping approach should involve the surface layers because the incorporated metal atoms must take part in the formation of the intermediates. The good performance of incorporated surface Co dopants (0.36 V) agrees with the generally recognized high efficiency of mixed Co/Fe oxides as OER catalysts (experimental range: 0.24 V $< \eta <$ 0.49 V) [218, 282, 283]. Furthermore, the 0.36 V overpotential value is extremely close to that computed for the $CoFe_2O_4(001)$ surface, which is 0.38 V, as reported in a recent computational study based on DFT calculations [296]. This new result, by proving that the same performance towards OER can be obtained by introducing a limited quantity of Co on Fe_3O_4 surface than by using a Co/Fe mixed oxide, suggests experimentalists a clear and practical way to cut the catalyst cost.

Chapter 6

Parametrization of the Fe-O_{Water} Cross-Interaction for a More Accurate Fe_3O_4/Water Interface Model

In this chapter, a set of CLASS2 force field parameters is optimized for the description of the $Fe-O_{Water}$ cross-interaction to catch the main features of iron oxides/water interfaces. We used as references hybrid density functional theory (HSE06) calculations of the potential energy function for a single water molecule adsorbed on the $Fe_3O_4(001)$ surface and Hubbard-corrected density functional tight-binding (DFTB+U) molecular dynamics simulations for a water tri-layer on the same surface. We assessed the performance of the new parameters through the analysis of the number density profile of a water bulk (12 nm) sandwiched between two magnetite slabs of large surface area. Finally, we tested their transferability for the water adsorption on the curved surface of a spherical Fe_3O_4 nanoparticle of realistic size (2.5 nm).

The results reported in this chapter have been published in: Siani, P.; Bianchetti, E.; Liu, H.; Di Valentin, C. *Journal of Chemical Physics* **2021**, *154*, 034702.

6.1 Introduction

Iron oxides/water interfaces are involved in many fundamental and technological processes, therefore accurate force field parameters for the description of the bond between surface iron sites and water oxygens, which we provide through this work, are critical to perform useful molecular dynamics simulations in this fast-developing research field.

Water adsorption on the low-index (001) Fe_3O_4 facet has been extensively investigated in the past both through experiments and theoretical calculations [70, 86, 261, 297–303]. In particular, a mixed undissociated and dissociated adsorption mode was determined for one water monolayer adsorbed on the surface by means of a combined experimental and computational study [261]. On half of the metal adsorption sites, water molecules dissociate forming a partially hydroxylated surface, whereas on the remaining adsorption sites water adsorbes molecularly. In a previous work by my group [245] based on the research activity for my master thesis, we investigated the behaviour of water multilayers with increasing thickness up to 12 nm comparing quantum mechanics (QM) with molecular mechanics (MM) results.

However, the classical model that we used [245], although catching the general aspects of the water structure and of solvation, has shown limited accuracy in the description of the details of the water coordination to the exposed surface undercoordinated iron sites. In the above-mentioned model, longer distances (∼2.7-2.8 Å) were observed between the superficial iron atoms and the oxygen atoms of adsorbed water molecules (from now on $Fe{-}O_{Water}$) compared to higher-level calculations using hybrid DFT (short for *density functional theory*) and Hubbard-corrected SCC-DFTB (short for *self-consistent redistribution of charges density functional tight-binding*), from now on DFTB+U, methods that predict Fe-O_{Water} distances about 2.2 Å.

Herein, we provide an optimized set of CLASS2 force field parameters that corrects this issue and, therefore, accurately describes at the classical level the water coordination on the Fe sites over the partially hydroxylated Fe_3O_4(001) surface. In addition, a quantitative agreement of surface and bulk properties is observed between classical molecular mechanics molecular dynamics (from now on MM-MD) simulations and DFTB+U molecular dynamics (from now on DFTB-MD) simulations for a bulk water density distribution along the Fe_3O_4(001) surface normal. Finally, the transferability of the optimized parameters is tested for the description of the water adsorption on the curved surface of a spherical Fe_3O_4 nanoparticle, from now on nanosphere (NS), of realistic size with a diameter of 2.5 nm. All the MM simulations were performed by my colleague Paulo Siani.

6.2 Methods and models

All atomistic MM simulations were carried out with the LAMMPS program (version 7 Aug 2019) [304]. We made use of the CLASS2 potentials (see Reference [305] for a full description of the COMPASS/CLASS2 force field (FF)). This FF describes the non-bonded interactions for the repulsive and dispersive van der Waals forces through a Lennard-Jones 9-6 potential form (Equation (6.1)), whereas the long-range electrostatic interactions are modeled by a classical Coulomb functional form (Equation (6.2)):

$$E_{VdW} = \sum_{i,j} \varepsilon_{ij} \left[2\left(\frac{\sigma_{ij}^0}{r_{ij}}\right)^9 - 3\left(\frac{\sigma_{ij}^0}{r_{ij}}\right)^6 \right], \tag{6.1}$$

$$E_{Elec} = \frac{1}{4\pi\varepsilon_0} \sum_{i,j} \frac{q_i q_j}{r_{ij}}. \tag{6.2}$$

Here, σ_{ij} defines the inter-atomic distance between a pair of atoms at which the potential energy function assumes a minimum value, ε_{ij} the potential well depth for this pairwise potential, and q_i and q_j the partial atomic charges on the atoms i and j. Bonded and non-bonded parameters for the CLASS2-based three-site water model and the hydroxyl group are taken from the INTERFACE-FF [306]. The LJ(9-6) parameters for the Fe^{II}, Fe^{III}, and O^{-II} atom-types were taken from Reference [307], and the partial-atomic charges for these atoms were derived from the hybrid DFT (HSE06) calculations and reported in Table 6.1. For unlike atom-types, the sigma and epsilon cross-parameters are given by the sixth power combining rules [305] accordingly to the following equations:

$$\sigma_{ij} = \left[\frac{(\sigma_i^0)^6 + (\sigma_j^0)^6}{2} \right]^{\frac{1}{6}} f_1, \tag{6.3}$$

$$\varepsilon_{ij} = 2\sqrt{\varepsilon_i \varepsilon_j} \left[\frac{(\sigma_i^0 \sigma_j^0)^3}{(\sigma_i^0)^6 + (\sigma_j^0)^6} \right] f_2. \tag{6.4}$$

The scanning of both sigma $\sigma[\mathrm{Fe{-}O_{Water}}]$ and epsilon $\varepsilon[\mathrm{Fe{-}O_{Water}}]$ $\mathrm{Fe{-}O_{Water}}$ cross-parameters consist of systematic variation in the f_1 (Equation (6.3)) and f_2 (Equation(6.4)) factors over their original values (case in which f_1 and f_2 are equal to the unit) until the error function reaches satisfactory agreement against the reference data set:

$$RMSE = \sqrt{\frac{\sum_{i=1}^{n} (X_{MM,i} - X_{QM,i})^2}{n}} \tag{6.5}$$

Error function values close to zero indicate good agreement, whereas deviations to larger values indicate a more flawed agreement between the MM ($X_{MM,i}$) and the QM reference ($X_{QM,i}$) predictions for the peaks maximum position in the number density profiles. To accurately determine the QM reference data in Equation (6.5), the first, second, and third maxima peaks in the DFTB-MD density profiles were estimated through a non-linear Gaussian fitting. This protocol is in line with a previous published protocol [308].

The atomic coordinates of the Fe, O and H in the Fe_3O_4 slab and NS were fixed at the DFTB+U-optimized geometry by zeroing the forces on these atoms every MM-MD simulation step. To avoid spurious effects due to water evaporation at the trilayer/vacuum interphase in the MM-MD simulations, sufficient water molecules were included between the third water layer and the vacuum phase to keep the inner solvation layers stable on the surface. For further details regarding the MM simulations set up, please refer to Reference [309].

6.2.1 Potential energy function (PEF) calculations

Density functional theory calculations of a single water molecule adsorbed on bare $Fe_3O_4(001)$ surface were used as a first benchmark to tune the force field parameters. The system was allowed to ionically relax to a stable configuration. The adsorption of water oxygen (O_{Water}) on top of a surface 5-coordinated Fe ion at octahedral site was observed in agreement with a previous study [261]. Therefore, hybrid DFT (HSE06) calculations were performed for 23 configurations of the water molecule at different distances from the surface Fe. For this purpose, the adsorbed water molecule has been rigidly shifted along the surface normal. The adsorption energies of these configurations were obtained performing *self-consistent field* (SCF) calculations without any ionic relaxation. Then, a distance-dependent (Fe–O_{Water}) potential energy function (PEF) was built up.

6.2.2 Density profile calculations

For the second refinement of the FF parameters, linear number density profiles (atoms/Å) were calculated to fit the MM-MD and DFTB-MD results, in which only O atoms belonging to the molecular water were considered. First, the space was divided along the z coordinate in equally sized bins (Δz) of thickness set at 0.1 Å. Then, the particles count for each bin was normalized by the total count of particles and by its size.

6.2.3 DFT and DFTB computational details

To tune the force field parameters, hybrid DFT calculations (HSE06 [233, 240], see Section 2.1 for further details about the method) were performed through the CRYSTAL17 package [247, 248]. In these calculations, the Kohn-Sham orbitals were expanded in Gaussian-type orbitals: the all-electron basis sets are H−511G(p1), O−8411G(d1) and Fe−86411G(d41), according to the scheme previously used for Fe_3O_4 [33, 70, 125, 245]. The convergence criterion of 10^{-6} hartree for total energy and $4.5{\cdot}10^{-4}$ hartree/bohr for forces during geometry optimization was used. The k points grid generated by the Monkhorst-Pack scheme was chosen to be $3 \times 3 \times 1$ since total energy difference was found to be below 1 meV when compared with larger grids up to $6 \times 6 \times 1$. According to a previous report [46], the inclusion of the van der Waals correction (DFT+D2 [310]) slightly changes only the adsorption energy of water on the Fe_3O_4(110) surface, so no van der Waals correction is included in this work.

To further refine the force field parameters, molecular dynamics simulations were performed using the SCC-DFTB method implemented in the DFTB+ package [241]. Here, DFTB is used as a shorthand for SCC-DFTB. For the Fe-Fe, Fe-H and Fe-C interactions, we used the "trans3d-0-1" set of parameters [242]. For the O-O, H-O, H-H, O-C, H-C and C-C interactions we used the "mio-1-1" set of parameters [234]. For the Fe-O interactions, we used the Slater-Koster files fitted by my group previously [243], which can well reproduce the results for magnetite bulk and surfaces from HSE06 and PBE+U calculations. To properly deal with the strong correlation effects among Fe $3d$ electrons [244], DFTB+U with an effective U-J value of 3.5 eV was adopted according to previous work on magnetite by my group [125, 243, 245]. The conjugate gradient optimization algorithm was used for geometry optimization with the convergence criterion of 10^{-4} a.u. for forces. The convergence threshold on the self-consistent charge (SCC) procedure was set to be 10^{-5} a.u. for Fe_3O_4(001) surface and $5{\cdot}10^{-3}$ a.u. for Fe_3O_4 NS geometry optimization calculations. The k points grid generated by the Monkhorst-Pack scheme was chosen to be $6 \times 6 \times 1$ for Fe_3O_4(001) surface calculations. We further checked that the structure for the adsorption of water molecules is not affected by the inclusion of the van der Waals correction (DFTB+D3) [311, 312]. Since the variations are within 0.1 Å, no correction will be presented in the following. DFTB+U molecular dynamics (DFTB-MD) were performed within the canonical ensemble (NVT) using an Andersen thermostat to keep the temperature constant at 300 K. The total simulation time is 50 ps with a time step of 1 fs. The convergence threshold on SCC procedure was set to be $5{\cdot}10^{-3}$ a.u. and the k points grid generated by the Monkhorst–Pack scheme was chosen to be $4 \times 4 \times 1$ (since total energy difference was found to be below 1 meV when compared with larger grids up to $6 \times 6 \times 1$). To well describe the hydrogen bonds, a modified hydrogen

bonding damping (HBD) function was introduced with a $\zeta = 4$ parameter [313].

For the $Fe_3O_4(001)$ surface, the SCV model was used [79]. Here, the same structure used in previous works by my group [70, 243, 245] was adopted: a (1×1) 17-layer slab with inversion symmetry. In the z-direction, vacuum for more than 12 Å was introduced to avoid the spurious interaction between the slabs periodically replicated. Five layers in the middle of the slab were kept fixed to the bulk positions, whereas the other layers were fully relaxed. For water adsorption, molecules were put on both sides of the slab. For the Fe_3O_4 NS, the model (with about 1000 atoms) proposed in a previous work by my group [125] was used.

To evaluate the stability of one water molecule adsorbed on the $Fe_3O_4(001)$ surface and on the Fe_3O_4 NS, the adsorption energy (E_{Ads}) was calculated as follows:

$$E_{Ads} = E_{Total} - (E_{Surface/NS} + E_{H_2O}) \tag{6.6}$$

where E_{Total} is the total energy of the whole system (surface or NS and adsorbed water), $E_{Surface/NS}$ the energy of the $Fe_3O_4(001)$ surface or Fe_3O_4 NS, and E_{H_2O} the energy of one isolated water molecule.

6.3 Results and discussion

As stated earlier, the original sets of CLASS2-FF parameters adopted in Reference [245], by merely applying the sixth power combining rules to describe the cross-interaction between this pair of unlike atoms (see Equations (6.3) and (6.4)), led to an overestimated $Fe{-}O_{Water}$ distance. To tackle this issue, a systematic *ad hoc* parametrization of both the repulsive (step 1) and attractive (step 2) components in the Lennard Jones (9-6) potential (from now on LJ, see Equation (6.1)) for this pair of unlike atoms was carried out. The procedure consisted of an iterative two-step optimization: (1) tuning the sigma cross-parameter ($\sigma[Fe{-}O_{Water}]$) to seek for the best agreement between the hybrid DFT (HSE06) and the classical MM potential energy function (from now on PEF) for the adsorption of a single water molecule on the bare $Fe_3O_4(001)$ surface, and (2) tuning of the epsilon cross-parameters ($\varepsilon[Fe{-}O_{Water}]$) in a systematic fashion to find the best match between classical MM-MD and DFTB-MD predictions for the water-trilayer density profile. An objective error function (see Equation (6.5)) was built to measure the agreement between the QM reference data set and the corresponding classical MM results. Steps 1 and 2 were repeated until a satisfactory agreement between the classical MM-MD and the DFTB-MD predictions was obtained. The set of optimized CLASS2-FF parameters are reported in Table 6.1. Since the accuracy of the DFTB+U method was already validated against hybrid DFT calculations [245], DFTB-MD results were used as the reference data set for the water density profile.

Table 6.1: Optimized non-bonded LJ-parameters for the Fe−O_{Water} cross-interaction and partial atomic charges for magnetite atoms.

Parameters	Values
σ[Fe−O_{Water}] (Å)	3.508
ε[Fe−O_{Water}] (Kcal/mol)	0.035
q[Fe^{III}] (e)	+2.200
q[Fe^{II}] (e)	+1.920
q[O^{-II}] (e)	-1.502

Moreover, such a large number of atoms is unpractical for standard higher-level calculations (e.g., ab initio DFT-MD simulations). It is also important to mention again that partial atomic charges on the classical atoms are derived based on the hybrid DFT level of theory and were kept fixed during all this optimization procedure (see Table 6.1).

6.3.1 Fitting hybrid DFT PEF for single water molecule adsorption on Fe_3O_4(001) surface

Figure 6.1 shows the PEFs for the adsorption of a single water molecule on the bare Fe_3O_4(001) surface. Starting from the HSE06-optimized structure, the water molecule was rigidly shifted along the normal to the surface. To fit the target QM data, a systematic scanning of the σ[Fe−O_{Water}] cross-parameter was carried out by employing multiplicative factors over the original parameter of the CLASS2-FF set (brown curve), taken as starting-point in this optimization procedure. The σ[Fe−O_{Water}] cross-parameter mainly defines inter-atomic equilibrium distances between pair of atoms. By reducing the original σ[Fe−O_{Water}] cross-parameter at about 90% of its original value improves the match between the hybrid DFT reference data and the classical PEF profiles (see Figure 6.1). The optimized σ[Fe−O_{Water}] cross-parameter is reported in Table 6.1. However, even with enhanced compromise between the hybrid DFT and classical PEF profiles, only tuning the repulsive component in the MM model (i.e., the sigma cross-parameter) was not enough to reproduce via MM-MD the water molecules behavior under more realistic conditions as those in the DFTB-MD simulations.

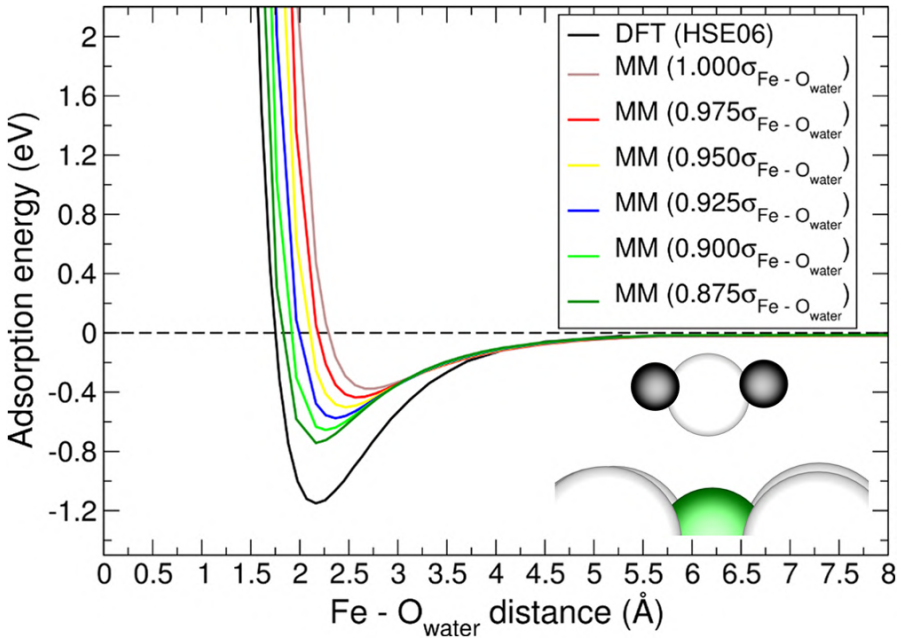

Figure 6.1: PEFs for the adsorption of a single water molecule on the bare $Fe_3O_4(001)$ surface calculated at the DFT/HSE06 and the MM level of theory. The hybrid DFT curve is shown in black. All other colors represent each set of CLASS2 parameters and their respective profiles obtained by scanning up the cross-parameters epsilon and sigma between the $Fe{-}O_{Water}$ atoms. The inset shows the side view of the single water molecule adsorbed on the surface. The green, black, small and large white beads represent Fe, H, O from water and O from the surface, respectively.

6.3.2 Comparing MM-MD and DFTB-MD density profile for a water trilayer on $Fe_3O_4(001)$ surface

To assess the performance of this prime set of CLASS2-FF parameters obtained from the fitting of the hybrid DFT adsorption PEF (step 1), classical MM-MD simulations were performed for the trilayer model system. We observed unsatisfactory agreement between the classical MM-MD predictions and the DFTB-MD target data for the water-trilayer density profile along the $Fe_3O_4(001)$ surface normal, i.e., the first solvation shell still splits up in two prominent peaks as previously observed for the original model (blue curve in Figure 6.2). Although it showed a definite improvement over that obtained by the original CLASS2-FF parameters in the previous publication by my group [245], it was necessary to carry out a further step of refinement to enhance the agreement between the classical MM-MD results and the DFTB-MD reference data set. In this second-step parametrization, a fine-tuning of the $\varepsilon[\mathrm{Fe{-}O_{Water}}]$ cross-parameter, i.e., the parameter which mainly defines the well depth of the LJ potential, was carried out.

First, a rough screening of $\varepsilon[\mathrm{Fe{-}O_{Water}}]$ values in a large range (i.e., 0.90-0.10$\times\varepsilon[\mathrm{Fe{-}O_{Water}}]$) was carried out, varying by successive decreasing of 10% over the original $\varepsilon[\mathrm{Fe{-}O_{Water}}]$ cross-parameter value and maintaining constant the optimized $\sigma[\mathrm{Fe{-}O_{Water}}]$ cross-parameter from the first-step parametrization. An imporvement of the agreement with the DFTB-MD reference data was observed after decreasing the $\varepsilon[\mathrm{Fe{-}O_{Water}}]$ cross-parameter at about 20% of its original value ($0.80\times\varepsilon[\mathrm{Fe{-}O_{Water}}]$). Second, a fine scan of with the smaller variation of 5% around $0.80\times\varepsilon[\mathrm{Fe{-}O_{Water}}]$ was carried out. To decide the most suitable set of $\varepsilon[\mathrm{Fe{-}O_{Water}}]$ cross-parameter, the maximum peaks position between the classical MM-MD and DFTB-MD predictions were compared for the water density profiles through the error function defined in Equation (6.5). The optimized $\varepsilon[\mathrm{Fe{-}O_{Water}}]$ cross-parameter is reported in Table 6.1.

Figure 6.2 shows the water density profiles along the $Fe_3O_4(001)$ surface normal. Classical MM-MD predictions using the final optimized set of CLASS2-FF parameters are shown in cyan (trilayer model) and green (bulk-water model). The reference data for the water density profile predicted by the DFTB-MD simulations is shown in black. For the sake of comparison, the water density profile estimated by the original model (blue) for the trilayer model was also included. The first two peaks for the MM-MD simulation with the original CLASS2-FF parameters merge into one single peak just above 10 Å for the simulation with the optimized parameters, in agreement with DFTB-MD results, thanks to the improved description of the $\mathrm{Fe{-}O_{Water}}$ cross-interaction.

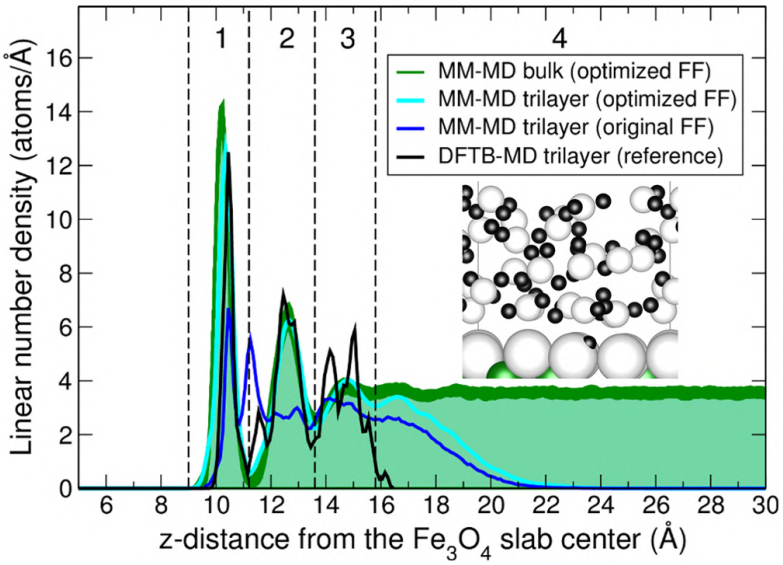

Figure 6.2: Number density profiles of water molecules along the partially hydroxylated $Fe_3O_4(001)$ surface normal. DFTB-MD simulation (black), classical MM-MD bulk-water simulation (green, thick line), classical MM-MD trilayer simulation with the optimized CLASS2-FF (cyan), and classical MM-MD trilayer simulation with the original CLASS2-FF (blue). Numbers between the dashed lines stand for different hydration shells. The inset shows the DFTB-MD water-trilayer model. The green, black, small and large white beads represent Fe, H, O from water and O from the surface, respectively.

Table 6.2: Structural parameters (in Å) of one water molecule adsorbed on bare and partially hydroxylated $Fe_3O_4(001)$ surface. The inter-atomic distance obtained through DFT/HSE06 method is taken as the reference for calculating the error.

Inter-atomic distance (Å)	DFTB+U	DFT/HSE06	MM (original)	MM (optimized)
$Fe-OH_2$	2.23	2.16	2.84 (+31.5%)	2.01 (-6.9%)
Fe−OH	1.89	1.93	1.89[a]	1.89[a]
$Fe-OH_2$	2.01	2.06	2.69 (+30.6%)	1.95 (-5.3%)
HO−HOH	1.57	1.48	1.62 (+9.5%)	1.54 (+4.1%)
$HO-OH_2$	2.57	2.52	2.60 (+3.2%)	2.53 (+0.4%)

[a]Fixed atoms in the slab.

6.3.3 Assessment of optimized FF parameters on single water molecule adsorption on $Fe_3O_4(001)$ surface

The results above indicate that a $Fe_3O_4(001)$ surface/water interface model could take advantage of these new CLASS2-FF parameters. To corroborate this last assumption, structural and energetic parameters for a single water molecule optimized adsorption on bare and partially hydroxylated $Fe_3O_4(001)$ surface were compared at different levels of theory (see Figures 6.3(a) and 6.3(b), respectively). Table 6.2 shows that the interatomic distances from the optimized set of MM parameters are in better agreement with DFTB+U and hybrid DFT results compared to the original set. In particular, for the bare surface, the $Fe-O_{Water}$ distance was 2.84 Å with the original FF, which is quite too long with respect the DFT/HSE06 reference value of 2.16 Å, as it was pointed out in the previous work of my group [245], whereas the same distance becomes 2.01 Å with optimized FF set of parameters, which is only 6.9% shorter than the reference value. Table 6.3 shows that the adsorption energy (E_{Ads}) obtained from the optimized set of FF parameters is in better agreement with DFTB+U and hybrid DFT data compared to the original FF. For instance, the E_{Ads} of -0.66 eV using the original set of FF parameters is off by 43% compared to the DFT/HSE06 reference data of -1.15 eV, while the E_{Ads} predicted by the optimized FF matches exactly the DFT/HSE06 reference value.

6.3.4 Assessment of optimized FF parameters on single water molecule adsorption on spherical Fe_3O_4 nanoparticle

In this section, the assessment of the transferability of the newly optimized set of parameters for the description of water adsorption on a Fe_3O_4 NS of realistic

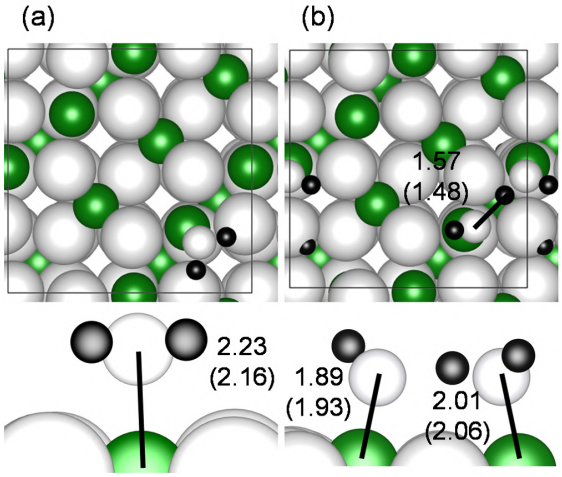

Figure 6.3: Top and side view of a single water molecule adsorbed on (a) bare $Fe_3O_4(001)$ surface and on (b) partially hydroxylated $Fe_3O_4(001)$ surface. The green, black, small and large white beads represent Fe, H, O from water and O from the surface, respectively. The hydrogen and $Fe-O_{Water}$ bonds are indicated by the solid lines. The bond length calculated by DFTB+U (outside the round brackets) and DFT/HSE06 (inside the round brackets) are given (in Å) for each configuration. The black squares represent the $(\sqrt{2} \times \sqrt{2})R45^{\circ}$ unit cell used in the calculations.

Table 6.3: Adsorption energy E_{Ads} (in eV) of one water molecule on bare and partially hydroxylated $Fe_3O_4(001)$ surface. The E_{Ads} obtained through DFT/HSE06 method is taken as the reference for calculating the error.

E_{Ads} (eV)	DFTB+U	DFT/HSE06	MM (original)	MM (optimized)
Bare	-1.30	-1.15	-0.66 (42.6%)	-1.15 (0.0%)
Hydroxylated	-1.95	-1.95	-1.28 (34.3%)	-1.56 (20.0%)

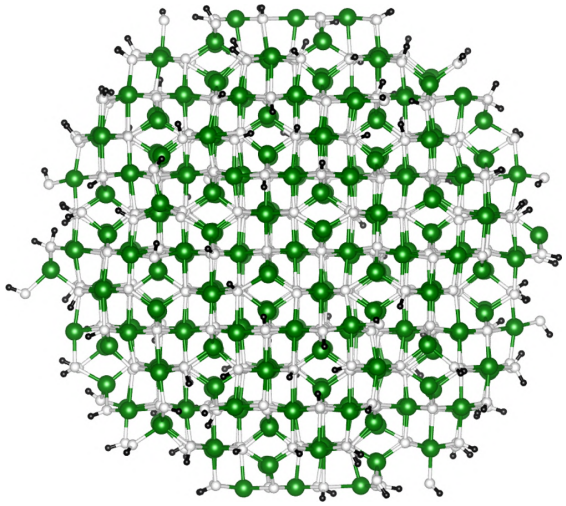

Figure 6.4: Partially hydroxylated Fe_3O_4 NS model. The green, black and white beads represent Fe, H and O, respectively.

Table 6.4: $Fe-O_{Water}$ inter-atomic distance (in Å) of one water molecule adsorbed on different sites of a partially hydroxylated Fe_3O_4 NS at DFTB+U and MM levels of theory. The distance between the water oxygen atom and the center of the NS is reported in parenthesis.

$Fe-OH_2$ (Å)	Site 1	Site 2	Site 3	Site 4	Site 5
DFTB+U	2.09 (15.06)	1.94 (15.05)	2.02 (13.83)	1.99 (13.41)	2.01 (13.29)
MM (from DFTB+U)	2.08 (15.02)	1.94 (15.01)	2.04 (13.82)	1.99 (13.41)	1.94 (13.31)
MM (from MM-MD)	...	...	...	2.10 (13.05)	2.07 (13.01)

size with about 1000 atoms (shown in Figure 6.4) is presented. To this end, the adsorption structure and energy of a single water molecule on different sites of the partially hydroxylated Fe_3O_4 NS were compared, as obtained at the MM level of theory with the CLASS2 force field parameters with the results from a QM method. In particular, DFTB+U results were used as the QM reference data set, since DFTB+U was previously validated against higher-level hybrid DFT results [245]. The MM results were obtained both through the direct optimization of DFTB+U structures (second row of Tables 6.4 and 6.5) and through the final optimization after 50 ns of MM-MD simulation at 300 K (third row of Tables 6.4 and 6.5). In all the MM calculations, the structure of the partially hydroxylated Fe_3O_4 NS was kept fixed at DFTB+U optimized geometry before water adsorption.

When one water molecule is adsorbed on sites 1, 2 and 3 (see Figure 6.5), MM structural results, both when optimized before and after molecular dynamics, very much resemble the DFTB+U ones. For the adsorption on sites 4 and 5,

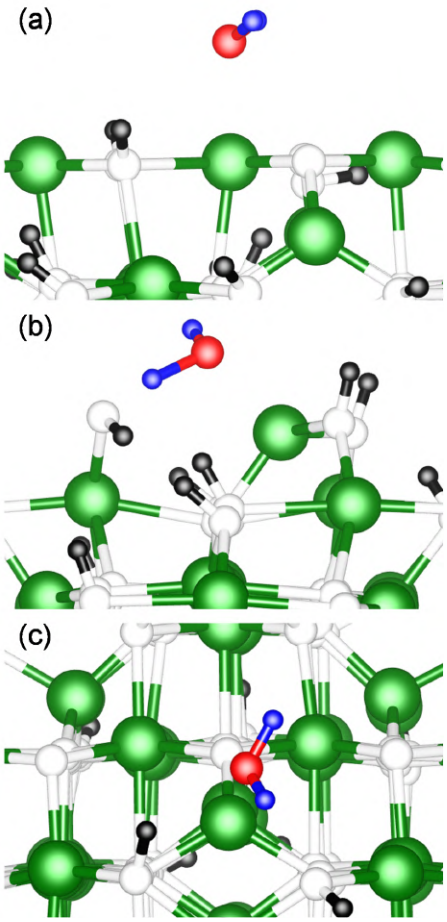

Figure 6.5: Adsorption of one water molecule on (a) site 1, (b) site 2 and (c) site 3 of the Fe_3O_4 NS at DFTB+U level. Structures optimized at MM level starting from DFTB+U ones are found to be nearly identical and they are not reported. The green, black, white, blue and red beads represent Fe, H, O from the partially hydroxylated NS and H, O from the water molecule, respectively.

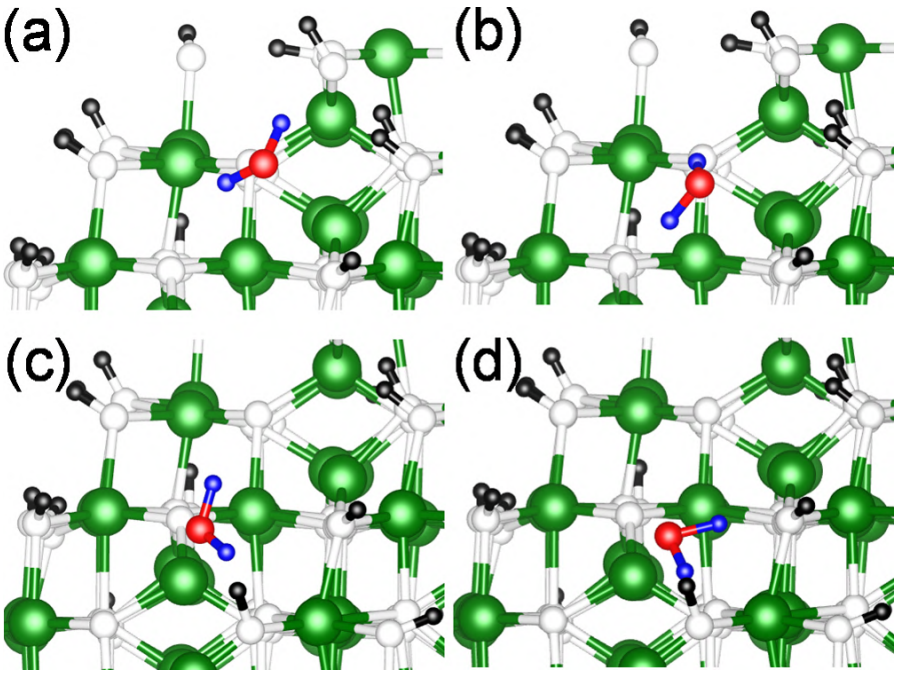

Figure 6.6: Adsorption of one water molecule on site 4 (a, b) and on site 5 (c, d) of the Fe_3O_4 NS at DFTB+U level of theory (a, c) and at MM (geometry optimization after MM-MD) level of theory (b, d). Structures optimized at MM level starting from DFTB+U ones are nearly identical and not reported. The green, black, white, blue and red beads represent Fe, H, O from the partially hydroxylated NS and H, O from the water molecule, respectively.

classical MM results before the MM-MD are in good agreement to DFTB+U ones (see Figures 6.6(a) and 6.6(c)), while classical MM results after MD are slightly different (see Figures 6.6(b) and 6.6(d)). Figures 6.6(a) and 6.6(c) show that before the MM-MD simulations, the water molecule tends to form one hydrogen bond, whereas Figures 6.6(b) and 6.6(d) show that after the MM-MD simulations, the water molecule interacts with two O atoms on the NS forming two H-bonds. Table 6.3 reports the water E_{Ads} values. A good agreement of the adsorption energies at DFTB+U and MM levels of theory is observed. It can be also observed that the optimized configuration after the MM-MD simulation (third row) is more stable than the one optimized before the MM-MD (second row). It should be noticed that, due to the formation of a second H-bond after MM-MD, the water molecule undergoes a structural rearrangement. The $Fe{-}O_{Water}$ distance is not much affected, whereas the molecule rotates to allow the formation of the new H-bonds, resulting in a significantly reduced distance between the O_{Water} atom and the NS centroid (see second and third rows in Table 6.4).

According to this assessment analysis, the transferability of the optimized

Table 6.5: Adsorption energy E_{Ads} (in eV) of one water molecule adsorbed on different sites of a partially hydroxylated Fe_3O_4 NS at DFTB+U and MM levels of theory.

E_{Ads} (eV)	Site 1	Site 2	Site 3	Site 4	Site 5
DFTB+U	-1.03	-2.71	-1.35	-1.93	-1.54
MM (from DFTB+U)	-1.14	-1.97	-0.80	-2.00	-1.92
MM (from MM-MD)	...	...	...	-2.59	-2.78

CLASS2 set of FF parameters turned out to be less accurate as the Fe neighborhood becomes less similar to that of the Fe_3O_4(001) flat surface for which the parameters have been optimized. The MM-MD simulations, depending on the site morphology, tend to maximize the number of H-bonds established by the water molecule with the NS surface atoms, as discussed above. This phenomenon in the classical Fe_3O_4(001) flat surface model was not observed because of the lower availability of neighboring surface O atoms as H-bond acceptors, as evident by Figure 6.7(a). In particular, Figure 6.7(a) shows that the adsorption site on the Fe_3O_4(001) flat surface is morphologically similar to the adsorption sites 1, 2 and 3 of the spherical nanoparticle in Figure 6.5. On the contrary, the morphology of site 5 in Figure 6.7(b) and in Figure 6.6(c) and 6.6(d), as in the case of site 4 in Figure 6.6(a) and 6.6(b), is different to that of the flat surface. Here, several surface O atoms are available as H-bond acceptors and the water molecule can thus establish strong H-bonds (with an O−H—O angle of ∼170° close to the optimal one of 180°).

It is necessary to stress that the HBD correction was used for all the DFTB+U calculations to get the best possible description of the H-bond interactions [313]. Based on the results above, it is possible to conclude that the classical model tends to overestimate the H-bond interaction between the water molecule and the NS surface.

To conclude this section, based on the results presented and discussed above, it is possible to say that the optimized set of CLASS2-FF parameters are suitable for the description of the water interface with a spherical Fe_3O_4 nanoparticle, because they perform very well in the description of the water adsorption on the surface of NS with respect to the QM reference, especially when the adsorption site is morphologically similar to that of the flat (001) surface. They still produce satisfactorily accurate results, even when the adsorption site is more affected by the curvature, except for a rigid shift of the water O atom towards the center of the nanoparticle due to a molecular rotation to achieve the highest number of H-bonds with the surface, keeping the Fe-O_{Water} distance essentially unmodified.

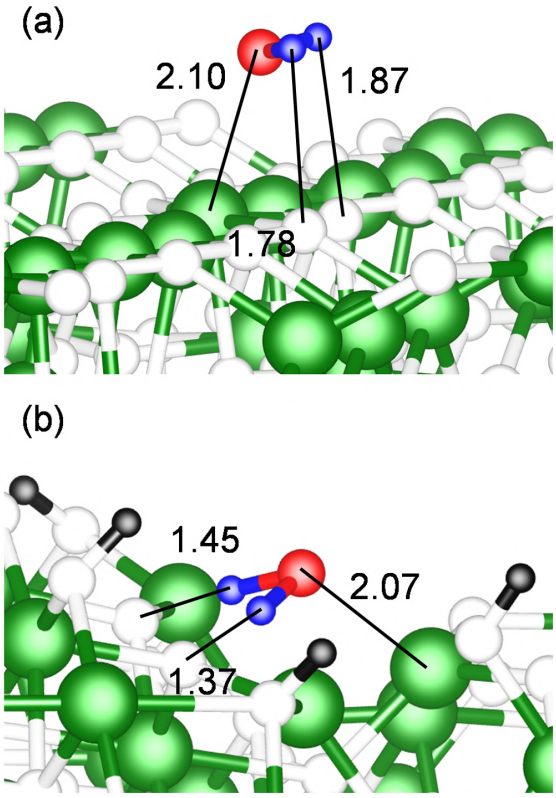

Figure 6.7: Adsorption of one water molecule on (a) the $Fe_3O_4(001)$ surface and (b) the site 5 of the partially hydroxylated Fe_3O_4 NS at the MM level of theory. Bonds are indicated by the solid black lines. The green, black, white, blue and red beads represent Fe, H, O from the partially hydroxylated NS and H, O from the water molecule, respectively.

6.4 Conclusions

In the present work, a new set of CLASS2-FF parameters was made available (see Table 6.1) for describing the molecular interaction between a partially hydroxylated $Fe_3O_4(001)$ surface and the interfacial water molecules. Further development towards a combination between both the present CLASS2-FF parameters and the well-established CLASS2-FF parameters for Fe_3O_4/organic interfaces [307], open up many possibilities on modeling and simulation of more complex Fe_3O_4/organic/water interfaces at realistic time and length scales. Here, their satisfactory transferability to the description of water adsorption on the curved surface of a spherical Fe_3O_4 nanoparticle of realistic size (2.5 nm) was proved. This fact allows the study of the atomistic details of the short range (chemical) and long range (physical) interfacial effects when a Fe_3O_4 nanoparticle is immersed in water, as done by my group in a following study [246]. In Reference [246], the atomistic structure and properties of the hydration shells around a NS immersed in bulk water were investigated by a multi-scale approach combining density functional tight-binding method and classical force field calculations (QM(DFTB+U)/MM). Parallel MM calculations leaded to very similar results, suggesting that the very cheap MM approach could be used to obtain reliable information on the dynamical behavior of Fe_3O_4 nanoparticles in aqueous media.

Chapter 7

Summary and Conclusions

Despite the increasing relevance of magnetite (Fe_3O_4) in the last decades at the forefront of the scientific research in emerging fields, such as nanomedicine, catalysis, and energy conversion, a small number of theoretical investigations has been published until few years ago. Theoretical simulations represent an extremely powerful tool to interpret and comprehend at the atomic scale experimental findings and guide the design of further experiments.

To this aim, however, accurate and solid theoretical framework and methods are often required, as in the case of magnetite. For example, standard LDA and GGA DFT approaches failed to reproduce the magnetite charge ordering [42, 43], i.e., the Fe^{II}/Fe^{III} disproportion at octahedral sites, as originally proposed by Vervey [2]. High-level quantum mechanical techniques, beyond standard DFT, are required to catch the proper electronic and magnetic properties of even the most simple bulk and flat surface magnetite systems. The lack of a theoretical framework in literature until few years ago is mainly due to the fact that the just-mentioned high-level methods became operative, available and affordable only in recent years.

Since the turn of the century, the Fe^{II}/Fe^{III} charge ordering has been observed experimentally below the Vervey transition temperature (T_V) [32, 47–49], when the crystal structure of magnetite assumes a monoclinic symmetry. Thanks to the implementation of the Hubbard correction (U) and hybrid exchange-correlation functionals in various software, Hubbard corrected LDA and GGA (LDA+U and GGA+U, respectively) [50–52] and hybrid functional [53] calculations reproduced the Fe^{II}/Fe^{III} disproportion at octahedral sites for bulk magnetite in the monoclinic phase.

More recently, in 2014, X-ray experiments provided evidence that the charge ordering is present in bulk magnetite even above T_V, when magnetite crystallizes in the cubic phase, up to room temperature [55]. This finding contradicted the state-of-the-art GGA+U [44, 46] and hybrid functional [45] investigations, which converged in the description of an average valence state of +2.5 at octahedral

sites for bulk magnetite in the cubic phase, in line with the prior hypothesis of a room-temperature symmetrical charge distribution over those iron ions.

In 2017, Liu and Di Valentin [33] put an end the debate on the electronic and magnetic properties of bulk magnetite in the cubic phase. HSE06 hybrid functional calculations were performed releasing the symmetry constraint on the electron density but not on the atomic positions. In this way, the authors were able to reproduce the Fe^{II}/Fe^{III} disproportion at octahedral sites, as confirmed by recent experiments [55]. With this computational set up, they also discussed other properties, such as the electronic band gap and iron ions magnetic moments, as already detailed in Section 1.1.1.

The foundations of this PhD thesis rely on the work done by all the groups cited above. Indeed, the electronic and magnetic properties of magnetite are a key factor in the investigation of magnetite-based nanostructures for various applications (see below) and they can be well-reproduced only within the proper theoretical framework. In particular, my research work inherited the theoretical framework adopted by Liu and Di Valentin [33] based on breaking the symmetry and HSE06 hybrid functional calculations.

In Chapter 3, we studied the effect of surface functionalization on the magnetization of Fe_3O_4 nanoparticles (NPs). We explored the effects of the adsorption of various ligands (containing hydroxyl, carboxylic, phosphonic, catechol, and silanetriol groups), commonly used to anchor surfactants during synthesis or other species during chemical reactions, onto the spin and structural disorder, which are phenomena contributing to the lowering of the NP magnetization. We simulated the spin disorder through a spin-flip process at octahedral Fe ions and correlated with the energy separation between O^{-II} $2p$ and Fe^{III}_{Oct} $3d$ states. Only through an accurate description, control, and manipulation of magnetite electronic and magnetic properties, it was possible to carry out this analysis, which involved the charge/spin ordering and magnetic moments of Fe ions at selected octahedral sites. We found that only multidentate bridging ligands hamper the spin canting process by establishing additional electronic channels between octahedral Fe ions for an enhanced ferromagnetic superexchange interaction. We also observed that the presence of anchoring organic acids interferes with structural disorder, by disfavoring surface reconstruction, whose description required, again, an accurate manipulation of Fe ions magnetic moments. In summary, the results of this chapter provide a first-principles description, at the electronic and atomistic level, of the mechanisms how surface functionalization alters the spin and structural disorder (spin canting and atomic reconstruction) in magnetite NPs and, consequently, affects their saturation magnetization.

In Chapter 4, we investigated the interaction between the pertechnetate ion ($Tc^{VII}O_4^-$), a radioactive waste whose major issue is the high mobility in the

environment, and the $Fe_3O_4(001)$ surface, starting from its adsorption and proceeding with possible products of the full reduction to Tc^{IV} species and their retention. Since the reduction of $Tc^{VII}O_4^-$ is at the expenses of magnetite Fe^{II} ions, the accurate description of the Fe^{II}/Fe^{III} disproportion at octahedral sites is a key factor, especially when comparing the reducing power of surface models with different Fe^{II}/Fe^{III} ratio. Indeed, we found that the formation of a reduced Tc^{VI} species through an electron transfer is favored by magnetite surfaces with a higher Fe^{II} ions content. Furthermore, we explored various model structures for the hypothetical final products of the full reduction from Tc^{VII} to Tc^{IV}: Tc^{IV} incorporation or adsorption in the form of $Tc^{IV}O_2{\cdot}2H_2O$ chains. Regarding the adsorption of $TcO_2{\cdot}2H_2O$ chains on magnetite, we have found that the periodicity of the $Fe_3O_4(001)$ surface matches that of the $TcO_2{\cdot}2H_2O$ chains and we have proposed three model structures characterized by different symmetries. In summary, we have demonstrated that the $Fe_3O_4(001)$ surface can adsorb and reduce Tc^{VII} complexes and retain Tc^{IV} species.

In Chapter 5, we studied the $Fe_3O_4(001)$ surface as support material for SACs for the oxygen evolution reaction (OER), which is the bottleneck of the electrochemical production of hydrogen. Inexpensive and abundant metal atoms, such as Ti, Co, Ni, and Cu, were trapped in various configuration either loaded as adatoms on the $Fe_3O_4(001)$ surface or incorporated within the topmost layers. Once again, the possibility to accurately describe and control the electronic and magnetic properties of magnetite has been fundamental to catch the effects of the dopants. These effects are then reflected in the Gibbs free energy profiles. Indeed, different results in terms of energetic with respect those observed for the clean surface were found when dopants were directly involved in the formation of the intermediates. The presence of Ti with the magnetite lattice leaded to an increased overpotential, whereas that of Cu and Ni did not produce any significant change. On the contrary, Co atoms were found to significantly improve the OER performance of magnetite via both the reaction pathways proposed. In summary, Co-doped systems, independent of whether the Co is *incorporated in* or *deposited on* the surface, have been found to be the most promising model electrocatalysts among those investigated in these study, getting closer to the generally recognized high efficiency of mixed Co/Fe oxides as OER catalysts.

In Chapter 6, we discussed the protocol we followed to make available a new set of CLASS2 force field parameters for describing the molecular interaction between a partially hydroxylated $Fe_3O_4(001)$ surface and the interfacial water molecules. We used hybrid DFT (HSE06) and Hubbard-corrected density functional tight-binding (DFTB+U) calculations as a reference, in line with the methodological discussion above. We assessed the performance and transferability of the new parameters for the water adsorption on the curved surface of a spherical Fe_3O_4

NP of realistic size (2.5 nm).

In summary, the scientific community is now facing a new era in the study of magnetite. The theoretical framework to describe such a material in an accurate and affordable manner has been made available over the years by the research groups cited at the beginning of this chapter. Consequently, the focus of the computational scientific research is currently moving to the investigation of magnetite nanosystems for biomedical applications and surfaces for catalysis. In this context, the present PhD thesis exploits the state-of-the-art theoretical methodology and tools to unravel the mechanisms underlying various process involving magnetite nanostructures and surfaces for applications in emerging fields. We demonstrate that capturing the electronic and magnetic properties of magnetite with the proper accuracy is a key factor for investigating, describing, and elucidating such mechanisms.

To conclude, the methodological protocols — as well as the chemical and physical concepts — developed here for model systems can be applied also to the study of more complex interfaces between magnetite (or even other magnetic transition metal oxides) and organic/inorganic species. Therefore, this work provides a solid and exhaustive guide for future theoretical investigations on magnetic oxides and for the experimental design of optimized nanostructures to be used in specific applications.

Bibliography

(1) Bragg, W. H. *Nature* **1915**, *95*, 561.

(2) Verwey, E. J. W. *Nature* **1939**, *144*, 327–328.

(3) Néel, L. *Annales de Physique* **1948**, *12*, 137–198.

(4) Goodenough, J. B.; Loeb, A. L. *Physical Review* **1955**, *98*, 391–408.

(5) Goodenough, J. B., *Magnetism and the Chemical Bond*; Wiley Interscience, Ed., New York, 1963.

(6) Cornell, R. M.; Schwertmann, U., *The Iron Oxides: Structure, Properties, Reactions, Occurrences, and Uses*; Wiley-VCH, Ed., Weinheim, 2003.

(7) Ratnasamy, C.; Wagner, J. P. *Catalysis Reviews* **2009**, *51*, 325–440.

(8) Tartaj, P.; Morales, M. P.; Gonzalez-Carreño, T.; Veintemillas-Verdaguer, S.; Serna, C. J. *Advanced Materials* **2011**, *23*, 5243–5249.

(9) Pankhurst, Q. A.; Connolly, J.; Jones, S. K.; Dobson, J. *Journal of Physics D: Applied Physics* **2003**, *36*, R167–R181.

(10) Gupta, A. K.; Gupta, M. *Biomaterials* **2005**, *26*, 3995–4021.

(11) Laurent, S.; Forge, D.; Port, M.; Roch, A.; Robic, C.; Vander Elst, L.; Muller, R. N. *Chemical Reviews* **2008**, *108*, 2064–2110.

(12) Sun, C.; Lee, J. S.; Zhang, M. *Advanced Drug Delivery Reviews* **2008**, *60*, 1252–1265.

(13) Colombo, M.; Carregal-Romero, S.; Casula, M. F.; Gutiérrez, L.; Morales, M. P.; Böhm, I. B.; Heverhagen, J. T.; Prosperi, D.; Parak, W. J. *Chemical Society Reviews* **2012**, *41*, 4306–4334.

(14) Wu, W.; Wu, Z.; Yu, T.; Jiang, C.; Kim, W. S. *Science and Technology of Advanced Materials* **2015**, *16*, 023501.

(15) Wu, W.; Jiang, C. Z.; Roy, V. A. *Nanoscale* **2016**, *8*, 19421–19474.

(16) Hou, Z.; Liu, Y.; Xu, J.; Zhu, J. *Nanoscale* **2020**, *12*, 14957–14975.

(17) Hou, Y.; Yu, J.; Gao, S. *Journal of Materials Chemistry* **2003**, *13*, 1983–1987.

(18) Cheng, F.; Liang, J.; Tao, Z.; Chen, J. *Advanced materials* **2011**, *23*, 1695–1715.

(19) Kobayashi, T.; Scheinost, A. C.; Fellhauer, D.; Gaona, X.; Altmaier, M. *Radiochimica Acta* **2013**, *101*, 323–332.

(20) Marshall, T. A.; Morris, K.; Law, G. T.; Mosselmans, J. F. W.; Bots, P.; Parry, S. A.; Shaw, S. *Environmental Science & Technology* **2014**, *48*, 11853–11862.

(21) Zhong, D. K.; Sun, J.; Inumaru, H.; Gamelin, D. R. *Journal of the American Chemical Society* **2009**, *131*, 6086–6087.

(22) Sivula, K.; Le Formal, F.; Grätzel, M. *ChemSusChem* **2011**, *4*, 432–449.

(23) Parkinson, G. S. *Catalysis Letters* **2019**, *149*, 1137–1146.

(24) Müllner, M.; Riva, M.; Kraushofer, F.; Schmid, M.; Parkinson, G. S.; Mertens, S. F.; Diebold, U. *The Journal of Physical Chemistry C* **2018**, *123*, 8304–8311.

(25) Grumelli, D.; Wiegmann, T.; Barja, S.; Reikowski, F.; Maroun, F.; Allongue, P.; Balajka, J.; Parkinson, G. S.; Diebold, U.; Kern, K.; Magnussen, O. M. *Angewandte Chemie - International Edition* **2020**, *59*, 21904–21908.

(26) Mirabella, F.; Müllner, M.; Touzalin, T.; Riva, M.; Jakub, Z.; Kraushofer, F.; Schmid, M.; Koper, M. T.; Parkinson, G. S.; Diebold, U. *Electrochimica Acta* **2021**, *389*, 138638.

(27) Hermanek, M.; Zboril, R.; Medrik, I.; Pechousek, J.; Gregor, C. *Journal of the American Chemical Society* **2007**, *129*, 10929–10936.

(28) Van Steen, E.; Claeys, M. *Chemical Engineering & Technology* **2008**, *31*, 655–666.

(29) Ji, M.; Chen, G.; Wang, J.; Wang, X.; Zhang, T. *Catalysis Today* **2010**, *158*, 464–469.

(30) Walz, F. *Journal of Physics: Condensed Matter* **2002**, *14*, R285–R340.

(31) Iizumi, M.; Koetzle, T.; Shirane, G.; Chikazumi, S.; Matsui, M.; Todo, S. *Acta Crystallographica Section B: Structural Crystallography and Crystal Chemistry* **1982**, *38*, 2121–2133.

(32) Senn, M. S.; Wright, J. P.; Attfield, J. P. *Nature* **2012**, *481*, 173–176.

(33) Liu, H.; Di Valentin, C. *The Journal of Physical Chemistry C* **2017**, *121*, 25736–25742.

(34) Lad, R. J.; Henrich, V. E. *Physical Review B* **1989**, *39*, 13478.

(35) Morton, S. A.; Waddill, G. D.; Kim, S.; Schuller, I. K.; Chambers, S. A.; Tobin, J. G. *Surface Science* **2002**, *513*, L451–L457.

(36) Wang, W.; Mariot, J.-M.; Richter, M. C.; Heckmann, O.; Ndiaye, W.; De Padova, P.; Taleb-Ibrahimi, A.; Le Fevre, P.; Bertran, F.; Bondino, F., et al. *Physical Review B* **2013**, *87*, 085118.

(37) Taguchi, M.; Chainani, A.; Ueda, S.; Matsunami, M.; Ishida, Y.; Eguchi, R.; Tsuda, S.; Takata, Y.; Yabashi, M.; Tamasaku, K., et al. *Physical Review Letters* **2015**, *115*, 256405.

(38) Yu, Q.; Mottaghizadeh, A.; Wang, H.; Ulysse, C.; Zimmers, A.; Rebuttini, V.; Pinna, N.; Aubin, H. *Physical Review B* **2014**, *90*, 075122.

(39) Park, J.-H.; Tjeng, L.; Allen, J.; Metcalf, P.; Chen, C. *Physical Review B* **1997**, *55*, 12813.

(40) Jordan, K.; Cazacu, A.; Manai, G.; Ceballos, S.; Murphy, S.; Shvets, I. *Physical Review B* **2006**, *74*, 085416.

(41) Hevroni, A.; Bapna, M.; Piotrowski, S.; Majetich, S. A.; Markovich, G. *The Journal of Physical Chemistry Letters* **2016**, *7*, 1661–1666.

(42) Zhang, Z.; Satpathy, S. *Physical Review B* **1991**, *44*, 13319.

(43) Pentcheva, R.; Wendler, F.; Meyerheim, H. L.; Moritz, W.; Jedrecy, N.; Scheffler, M. *Physical Review Letters* **2005**, *94*, 126101.

(44) Roldan, A.; Santos-Carballal, D.; de Leeuw, N. H. *The Journal of Chemical Physics* **2013**, *138*, 204712.

(45) Noh, J.; Osman, O. I.; Aziz, S. G.; Winget, P.; Brédas, J. L. *Science and Technology of Advanced Materials* **2014**, *15*, 044202.

(46) Aschauer, U.; Selloni, A. *The Journal of Chemical Physics* **2015**, *143*, 044705.

(47) Wright, J. P.; Attfield, J.; Radaelli, P. *Physical Review Letters* **2001**, *87*, 266401.

(48) Schlappa, J.; Schüßler-Langeheine, C.; Chang, C.; Ott, H.; Tanaka, A.; Hu, Z.; Haverkort, M.; Schierle, E.; Weschke, E.; Kaindl, G., et al. *Physical Review Letters* **2008**, *100*, 026406.

(49) Weng, S.-C.; Lee, Y.-R.; Chen, C.-G.; Chu, C.-H.; Soo, Y.-L.; Chang, S.-L. *Physical Review Letters* **2012**, *108*, 146404.

(50) Leonov, I.; Yaresko, A. N.; Antonov, V. N.; Korotin, M. A.; Anisimov, V. I. *Physical Review Letters* **2004**, *93*, 146404.

(51) Jeng, H.-T.; Guo, G. Y.; Huang, D. J. *Physical Review Letters* **2004**, *93*, 156403.

(52) Jeng, H.-T.; Guo, G.; Huang, D. *Physical Review B* **2006**, *74*, 195115.

(53) Rowan, A. D.; Patterson, C. H.; Gasparov, L. V. *Physical Review B* **2009**, *79*, 205103.

(54) Anderson, P. W. *Physical Review* **1956**, *102*, 1008.

(55) Bosak, A.; Chernyshov, D.; Hoesch, M.; Piekarz, P.; Le Tacon, M.; Krisch, M.; Kozłowski, A.; Oleś, A. M.; Parlinski, K. *Physical Review X* **2014**, *4*, 011040.

(56) Rakhecha, V.; Murthy, N. *Journal of Physics C: Solid State Physics* **1978**, *11*, 4389.

(57) Wright, J. P.; Attfield, J. P.; Radaelli, P. G. *Physical Review B* **2002**, *66*, 214422.

(58) Parkinson, G. S. *Surface Science Reports* **2016**, *71*, 272–365.

(59) Yang, T.; Wen, X.-D.; Ren, J.; Li, Y.-W.; Wang, J.-G.; Huo, C.-F. *Journal of Fuel Chemistry and Technology* **2010**, *38*, 121–128.

(60) Yu, X.; Huo, C.-F.; Li, Y.-W.; Wang, J.; Jiao, H. *Surface Science* **2012**, *606*, 872–879.

(61) Santos-Carballal, D.; Roldan, A.; Grau-Crespo, R.; de Leeuw, N. H. *Physical Chemistry Chemical Physics* **2014**, *16*, 21082–21097.

(62) Feld, A.; Weimer, A.; Kornowski, A.; Winckelmans, N.; Merkl, J. P.; Kloust, H.; Zierold, R.; Schmidtke, C.; Schotten, T.; Riedner, M.; Bals, S.; Weller, H. *ACS Nano* **2019**, *13*, 152–162.

(63) Li, Y. L.; Yao, K. L.; Liu, Z. L. *Surface Science* **2007**, *601*, 876–882.

(64) Parkinson, G. S.; Lackner, P.; Gamba, O.; Maaß, S.; Gerhold, S.; Riva, M.; Bliem, R.; Diebold, U.; Schmid, M. *Surface Science* **2016**, *649*, L120–L123.

(65) Paul, M.; Sing, M.; Claessen, R.; Schrupp, D.; Brabers, V. A. M. *Physical Review B* **2007**, *76*, 075412.

(66) Shimizu, T. K.; Jung, J.; Kato, H. S.; Kim, Y.; Kawai, M. *Physical Review B* **2010**, *81*, 235429.

(67) Sala, A.; Marchetto, H.; Qin, Z.-H.; Shaikhutdinov, S.; Schmidt, T.; Freund, H.-J. *Physical Review B* **2012**, *86*, 155430.

(68) Noh, J.; Osman, O. I.; Aziz, S. G.; Winget, P.; Brédas, J.-L. *Chemistry of Materials* **2015**, *27*, 5856–5867.

(69) Condon, N. G.; Leibsle, F. M.; Parker, T.; Lennie, A. R.; Vaughan, D. J.; Thornton, G. *Physical Review B* **1997**, *55*, 15885.

(70) Liu, H.; Di Valentin, C. *Nanoscale* **2018**, *10*, 11021–11027.

(71) Tarrach, G.; Bürgler, D.; Schaub, T.; Wiesendanger, R.; Güntherodt, H.-J. *Surface Science* **1993**, *285*, 1–14.

(72) Chambers, S. A.; Thevuthasan, S.; Joyce, S. A. *Surface Science* **2000**, *450*, L273–L279.

(73) Mijiritskii, A. V.; Boerma, D. O. *Surface Science* **2001**, *486*, 73–81.

(74) Voogt, F. C.; Fujii, T.; Smulders, P. J. M.; Niesen, L.; James, M. A.; Hibma, T. *Physical Review B* **1999**, *60*, 11193.

(75) Stanka, B.; Hebenstreit, W.; Diebold, U.; Chambers, S. A. *Surface Science* **2000**, *448*, 49–63.

(76) Łodziana, Z. *Physical Review Letters* **2007**, *99*, 206402.

(77) Pentcheva, R.; Moritz, W.; Rundgren, J.; Frank, S.; Schrupp, D.; Scheffler, M. *Surface Science* **2008**, *602*, 1299–1305.

(78) Novotny, Z.; Argentero, G.; Wang, Z.; Schmid, M.; Diebold, U.; Parkinson, G. S. *Physical Review Letters* **2012**, *108*, 216103.

(79) Bliem, R.; McDermott, E.; Ferstl, P.; Setvin, M.; Gamba, O.; Pavelec, J.; Schneider, M. A.; Schmid, M.; Diebold, U.; Blaha, P.; Hammer, L.; Parkinson, G. S. *Science* **2014**, *346*, 1215–1218.

(80) Arndt, B.; Bliem, R.; Gamba, O.; van der Hoeven, J. E.; Noei, H.; Diebold, U.; Parkinson, G. S.; Stierle, A. *Surface Science* **2016**, *653*, 76–81.

(81) Kraushofer, F.; Mirabella, F.; Xu, J.; Pavelec, J.; Balajka, J.; Müllner, M.; Resch, N.; Jakub, Z.; Hulva, J.; Meier, M.; Schmid, M.; Diebold, U.; Parkinson, G. S. *The Journal of Chemical Physics* **2019**, *151*, 154702.

(82) Arndt, B.; Creutzburg, M.; Grånäs, E.; Volkov, S.; Krausert, K.; Vlad, A.; Noei, H.; Stierle, A. *The Journal of Physical Chemistry C* **2019**, *123*, 26662–26672.

(83) Arndt, B.; Lechner, B. A.; Bourgund, A.; Grånäs, E.; Creutzburg, M.; Krausert, K.; Hulva, J.; Parkinson, G. S.; Schmid, M.; Vonk, V., et al. *Physical Chemistry Chemical Physics* **2020**, *22*, 8336–8343.

(84) Righi, G.; Fabris, S.; Piccinin, S. *The Journal of Physical Chemistry C* **2021**, *125*, 18752–18761.

(85) Arndt, B.; Sellschopp, K.; Creutzburg, M.; Grånäs, E.; Krausert, K.; Vonk, V.; Müller, S.; Noei, H.; Feldbauer, G. B.; Stierle, A. *Communications Chemistry* **2019**, *2*, 92.

(86) Mulakaluri, N.; Pentcheva, R.; Wieland, M.; Moritz, W.; Scheffler, M. *Physical Review Letters* **2009**, *103*, 176102.

(87) Zhao, L.; Zhang, H.; Xing, Y.; Song, S.; Yu, S.; Shi, W.; Guo, X.; Yang, J.; Lei, Y.; Cao, F. *Chemistry of Materials* **2008**, *20*, 198–204.

(88) Sun, S.; Zeng, H. *Journal of the American Chemical Society* **2002**, *124*, 8204–8205.

(89) Sun, S.; Zeng, H.; Robinson, D. B.; Raoux, S.; Rice, P. M.; Wang, S. X.; Li, G. *Journal of the American Chemical Society* **2004**, *126*, 273–279.

(90) Park, J.; An, K.; Hwang, Y.; Park, J. E.; Noh, H. J.; Kim, J. Y.; Park, J. H.; Hwang, N. M.; Hyeon, T. *Nature Materials* **2004**, *3*, 891–895.

(91) Zheng, R. K.; Gu, H.; Xu, B.; Fung, K. K.; Zhang, X. X.; Ringer, S. P. *Advanced Materials* **2006**, *18*, 2418–2421.

(92) Kovalenko, M. V.; Bodnarchuk, M. I.; Lechner, R. T.; Hesser, G.; Schäffler, F.; Heiss, W. *Journal of the American Chemical Society* **2007**, *129*, 6352–6353.

(93) Kim, D.; Lee, N.; Park, M.; Kim, B. H.; An, K.; Hyeon, T. *Journal of the American Chemical Society* **2009**, *131*, 454–455.

(94) Zhao, L.; Duan, L. *European Journal of Inorganic Chemistry* **2010**, *36*, 5635–5639.

(95) Li, X.; Liu, D.; Song, S.; Wang, X.; Ge, X.; Zhang, H. *CrystEngComm* **2011**, *13*, 6017–6020.

(96) Roca, A. G.; Gutiérrez, L.; Gavilán, H.; Brollo, M. E. F.; Veintemillas-Verdaguer, S.; Morales, M. d. P. *Advanced Drug Delivery Reviews* **2019**, *138*, 68–104.

(97) Margulies, D. T.; Parker, F. T.; Rudee, M. L.; Spada, F. E.; Chapman, J. N.; Aitchison, P. R.; Berkowitz, A. E. *Physical Review Letters* **1997**, *79*, 5162–5165.

(98) Voogt, F. C.; Palstra, T. T. M.; Niesen, L.; Rogojanu, O. C.; James, M. A.; Hibma, T. *Physical Review B* **1998**, *57*, R8107.

(99) Hibma, T.; Voogt, F. C.; Niesen, L.; Van der Heijden, P. A. A.; De Jonge, W. J. M.; Donkers, J. J. T. M.; Van der Zaag, P. J. *Journal of Applied Physics* **1999**, *85*, 5291–5293.

(100) Martínez, B.; Obradors, X.; Balcells, L.; Rouanet, A.; Monty, C. *Physical Review Letters* **1998**, *80*, 181–184.

(101) Morales, M. P.; Veintemillas-Verdaguer, S.; Montero, M. I.; Serna, C. J.; Roig, A.; Casas, L.; Martinez, B.; Sandiumenge, F. *Chemistry of Materials* **1999**, *11*, 3058–3064.

(102) Kodama, R. H. *Journal of Magnetism and Magnetic Materials* **1999**, *200*, 359–372.

(103) Serna, C. J.; Bødker, F.; Mørup, S.; Morales, M. P.; Sandiumenge, F.; Veintemillas-Verdaguer, S. *Solid State Communications* **2001**, *118*, 437–440.

(104) McKenna, K. P.; Hofer, F.; Gilks, D.; Lazarov, V. K.; Chen, C.; Wang, Z.; Ikuhara, Y. *Nature Communications* **2014**, *5*, 5740.

(105) Nedelkoski, Z.; Kepaptsoglou, D.; Lari, L.; Wen, T.; Booth, R. A.; Oberdick, S. D.; Galindo, P. L.; Ramasse, Q. M.; Evans, R. F.; Majetich, S.; Lazarov, V. K. *Scientific Reports* **2017**, *7*, 45997.

(106) Lak, A.; Disch, S.; Bender, P. *Advanced Science* **2021**, *8*, 2002682.

(107) Reichel, V.; Kovács, A.; Kumari, M.; Bereczk-Tompa, É.; Schneck, E.; Diehle, P.; Pósfai, M.; Hirt, A. M.; Duchamp, M.; Dunin-Borkowski, R. E.; Faivre, D. *Scientific Reports* **2017**, *7*, 45484.

(108) Dunlop, D. J.; Özdemir, O., *Rock Magnetism: Fundamentals and Frontiers*; Cambridge University Press, Ed., Cambridge, 1997.

(109) Krishnan, K. M.; Pakhomov, A. B.; Bao, Y.; Blomqvist, P.; Chun, Y.; Gonzales, M.; Griffin, K.; Ji, X.; Roberts, B. K. *Journal of Materials Science* **2006**, *41*, 793–815.

(110) Li, Q.; Kartikowati, C. W.; Horie, S.; Ogi, T.; Iwaki, T.; Okuyama, K. *Scientific Reports* **2017**, *7*, 9894.

(111) Baaziz, W.; Pichon, B. P.; Fleutot, S.; Liu, Y.; Lefevre, C.; Greneche, J. M.; Toumi, M.; Mhiri, T.; Begin-Colin, S. *The Journal of Physical Chemistry C* **2014**, *118*, 3795–3810.

(112) Unni, M.; Uhl, A. M.; Savliwala, S.; Savitzky, B. H.; Dhavalikar, R.; Garraud, N.; Arnold, D. P.; Kourkoutis, L. F.; Andrew, J. S.; Rinaldi, C. *ACS Nano* **2017**, *11*, 2284–2303.

(113) Mohapatra, J.; Zeng, F.; Elkins, K.; Xing, M.; Ghimire, M.; Yoon, S.; Mishra, S. R.; Liu, J. P. *Physical Chemistry Chemical Physics* **2018**, *20*, 12879–12887.

(114) Vestal, C. R.; Zhang, Z. J. *Journal of the American Chemical Society* **2003**, *125*, 9828–9833.

(115) Roca, A. G.; Morales, M. P.; O'Grady, K.; Serna, C. J. *Nanotechnology* **2006**, *17*, 2783–2788.

(116) Guardia, P.; Batlle-Brugal, B.; Roca, A. G.; Iglesias, O.; Morales, M. P.; Serna, C. J.; Labarta, A.; Batlle, X. *Journal of Magnetism and Magnetic Materials* **2007**, *316*, 756–759.

(117) Roca, A. G.; Marco, J. F.; Morales, M. d. P.; Serna, C. J. *The Journal of Physical Chemistry C* **2007**, *111*, 18577–18584.

(118) Daou, T. J.; Grenèche, J. M.; Pourroy, G.; Buathong, S.; Derory, A.; Ulhaq-Bouillet, C.; Donnio, B.; Guillon, D.; Begin-Colin, S. *Chemistry of Materials* **2008**, *20*, 5869–5875.

(119) Roca, A. G.; Niznansky, D.; Poltierova-Vejpravova, J.; Bittova, B.; González-Fernández, M. A.; Serna, C. J.; Morales, M. P. *Journal of Applied Physics* **2009**, *105*, 114309.

(120) Salafranca, J.; Gazquez, J.; Pérez, N.; Labarta, A.; Pantelides, S. T.; Pennycook, S. J.; Batlle, X.; Varela, M. *Nano Letters* **2012**, *12*, 2499–2503.

(121) Donadel, K.; Felisberto, M. D. V.; Fávere, V. T.; Rigoni, M.; Batistela, N. J.; Laranjeira, M. C. M. *Materials Science and Engineering: C* **2008**, *28*, 509–514.

(122) Qu, J.; Liu, G.; Wang, Y.; Hong, R. *Advanced Powder Technology* **2010**, *21*, 461–467.

(123) Novotny, Z.; Mulakaluri, N.; Edes, Z.; Schmid, M.; Pentcheva, R.; Diebold, U.; Parkinson, G. S. *Physical Review B* **2013**, *87*, 195410.

(124) Sun, M.; Wang, X.; Chen, G.; Mi, W. *Journal of Applied Physics* **2017**, *121*, 015306.

(125) Liu, H.; Di Valentin, C. *Physical Review Letters* **2019**, *123*, 186101.

(126) Harris, R. A.; Van der Walt, H.; Shumbula, P. M. *Journal of Molecular Structure* **2013**, *1048*, 18–26.

(127) Harris, R. A.; Shumbula, P. M.; van der Walt, H. *Langmuir* **2015**, *31*, 3934–3943.

(128) Rawlings, A. E.; Bramble, J. P.; Tang, A. A.; Somner, L. A.; Monnington, A. E.; Cooke, D. J.; McPherson, M. J.; Tomlinson, D. C.; Staniland, S. S. *Chemical Science* **2015**, *6*, 5586–5594.

(129) Patitsa, M.; Karathanou, K.; Kanaki, Z.; Tzioga, L.; Pippa, N.; Demetzos, C.; Verganelakis, D. A.; Cournia, Z.; Klinakis, A. *Scientific Reports* **2017**, *7*, 775.

(130) Hosseini, A.-S.; Akbarzadeh, H.; Tayebee, R., et al. *Journal of Molecular Liquids* **2018**, *254*, 64–69.

(131) Sharifi Dehsari, H.; Harris, R. A.; Ribeiro, A. H.; Tremel, W.; Asadi, K. *Langmuir* **2018**, *34*, 6582–6590.

(132) Harris, R. A. *Journal of Molecular Liquids* **2019**, *288*, 111084.

(133) Gao, K.; Chang, Q.; Wang, B.; Gao, R.; He, J. *Diamond and Related Materials* **2020**, *101*, 107627.

(134) Perez, J. M.; Josephson, L.; O'Loughlin, T.; Högemann, D.; Weissleder, R. *Nature Biotechnology* **2002**, *20*, 816–820.

(135) Liu, J.; Sun, Z.; Deng, Y.; Zou, Y.; Li, C.; Guo, X.; Xiong, L.; Gao, Y.; Li, F.; Zhao, D. *Angewandte Chemie International Edition* **2009**, *48*, 5875–5879.

(136) Heuer-Jungemann, A. et al. *Chemical Reviews* **2019**, *119*, 4819–4880.

(137) Lee, J.-H.; Chen, K.-J.; Noh, S.-H.; Garcia, M. A.; Wang, H.; Lin, W.-Y.; Jeong, H.; Kong, B. J.; Stout, D. B.; Cheon, J., et al. *Angewandte Chemie* **2013**, *125*, 4480–4484.

(138) Massart, R. *IEEE Transactions on Magnetics* **1981**, *17*, 1247–1248.

(139) Wu, S.; Sun, A.; Zhai, F.; Wang, J.; Xu, W.; Zhang, Q.; Volinsky, A. A. *Materials Letters* **2011**, *65*, 1882–1884.

(140) Basuki, J. S.; Jacquemin, A.; Esser, L.; Li, Y.; Boyer, C.; Davis, T. P. *Polymer Chemistry* **2014**, *5*, 2611–2620.

(141) Deng, H.; Li, X.; Peng, Q.; Wang, X.; Chen, J.; Li, Y. *Angewandte Chemie* **2005**, *117*, 2842–2845.

(142) Ge, S.; Shi, X.; Sun, K.; Li, C.; Uher, C.; Baker Jr, J. R.; Banaszak Holl, M. M.; Orr, B. G. *The Journal of Physical Chemistry C* **2009**, *113*, 13593–13599.

(143) Woo, K.; Lee, H. J.; Ahn, J. P.; Park, Y. S. *Advanced Materials* **2003**, *15*, 1761–1764.

(144) Holmberg, K. *Journal of Colloid and Interface Science* **2004**, *274*, 355–364.

(145) Hamley, I. W. *Angewandte Chemie* **2003**, *42*, 1692–1712.

(146) Carril, M.; Fernández, I.; Rodríguez, J.; García, I.; Penadés, S. *Particle & Particle Systems Characterization* **2014**, *31*, 81–87.

(147) Piñeiro, Y.; Gómez, M. G.; Alves, L. d. C.; Prieto, A. A.; Acevedo, P. G.; Gudiña, R. S.; Puig, J.; Teijeiro, C.; Vilar, S. Y.; Rivas, J. *Magnetochemistry* **2020**, *6*, 4.

(148) Caravan, P.; Ellison, J. J.; McMurry, T. J.; Lauffer, R. B. *Chemical Reviews* **1999**, *99*, 2293–2352.

(149) Hao, D.; Ai, T.; Goerner, F.; Hu, X.; Runge, V. M.; Tweedle, M. *Journal of Magnetic Resonance Imaging* **2012**, *36*, 1060–1071.

(150) Bae, Y. H.; Park, K. *Journal of Controlled Release* **2011**, *153*, 198–205.

(151) Mou, X.; Ali, Z.; Li, S.; He, N. *Journal of Nanoscience and Nanotechnology* **2015**, *15*, 54–62.

(152) Unterweger, H.; Tietze, R.; Janko, C.; Zaloga, J.; Lyer, S.; Dürr, S.; Taccardi, N.; Goudouri, O.-M.; Hoppe, A.; Eberbeck, D., et al. *International Journal of Nanomedicine* **2014**, *9*, 3659–3676.

(153) Di Corato, R.; Béalle, G.; Kolosnjaj-Tabi, J.; Espinosa, A.; Clement, O.; Silva, A. K. A.; Menager, C.; Wilhelm, C. *ACS Nano* **2015**, *9*, 2904–2916.

(154) Noh, S.-H.; Moon, S. H.; Shin, T.-H.; Lim, Y.; Cheon, J. *Nano Today* **2017**, *13*, 61–76.

(155) Hergt, R.; Dutz, S.; Müller, R.; Zeisberger, M. *Journal of Physics: Condensed Matter* **2006**, *18*, S2919–S2934.

(156) Glöckl, G.; Hergt, R.; Zeisberger, M.; Dutz, S.; Nagel, S.; Weitschies, W. *Journal of Physics: Condensed Matter* **2006**, *18*, S2935–S2949.

(157) Lartigue, L.; Innocenti, C.; Kalaivani, T.; Awwad, A.; Sanchez Duque, M. d. M.; Guari, Y.; Larionova, J.; Guérin, C.; Montero, J.-L. G.; Barragan-Montero, V., et al. *Journal of the American Chemical Society* **2011**, *133*, 10459–10472.

(158) Yoo, D.; Jeong, H.; Noh, S.-H.; Lee, J.-H.; Cheon, J. *Angewandte Chemie* **2013**, *125*, 13285–13289.

(159) Chalasani, R.; Vasudevan, S. *Journal of Materials Chemistry* **2012**, *22*, 14925–14931.

(160) Yang, H.; Liang, W.; He, N.; Deng, Y.; Li, Z. *ACS Applied Materials & Interfaces* **2015**, *7*, 774–781.

(161) Urbanova, V.; Magro, M.; Gedanken, A.; Baratella, D.; Vianello, F.; Zboril, R. *Chemistry of Materials* **2014**, *26*, 6653–6673.

(162) Luppa, P. B.; Sokoll, L. J.; Chan, D. W. *Clinica Chimica Acta* **2001**, *314*, 1–26.

(163) Yoshihara, K.; Omori, T., *Technetium(V) chemistry as relevant to nuclear medicine*; Springer, Ed., Berlin, Heidelberg, 1996.

(164) Icenhower, J. P.; Qafoku, N. P.; Zachara, J. M.; Martin, W. J. *American Journal of Science* **2010**, *310*, 721–752.

(165) Shi, K.; Hou, X.; Roos, P.; Wu, W. *Analytica Chimica Acta* **2012**, *709*, 1–20.

(166) Momoshima, N.; Sayad, M.; Takashima, Y. *Journal of Radioanalytical and Nuclear Chemistry* **1995**, *197*, 245–251.

(167) Momoshima, N.; Sayad, M.; Yamada, M.; Takamura, M.; Kawamura, H. *Journal of Radioanalytical and Nuclear Chemistry* **2005**, *266*, 455–460.

(168) Jurisson, S.; Gawenis, J.; Landa, E. R. *Health Physics* **2004**, *87*, 423–428.

(169) Rard, J. A.; Rand, M. H.; Anderegg, G.; Wanner, H., *Chemical Thermodynamics of Technetium*; Elsevier, Ed., Amsterdam, 1999.

(170) Boyd, G. E. *Journal of Solution Chemistry* **1978**, *7*, 229–238.

(171) Meena, A. H.; Arai, Y. *Environmental Chemistry Letters* **2017**, *15*, 241–263.

(172) Eriksen, T. E.; Ndalamba, P.; Bruno, J.; Caceci, M. *Radiochimica Acta* **1992**, *58*, 67–70.

(173) Hallam, R. J.; Evans, N. D. M.; Jain, S. L. *Mineralogical Magazine* **2011**, *75*, 2439–2448.

(174) Churakov, S. V.; Hummel, W.; Fernandes, M. M. *Chimia* **2020**, *74*, 1000–1009.

(175) Schlegel, M. L.; Bataillon, C.; Blanc, C.; Prêt, D.; Eddy, F. *Environmental Science & Technology* **2010**, *44*, 1503–1508.

(176) Heald, S. M.; Krupka, K. M.; Brown, C. F. *Radiochimica Acta* **2012**, *100*, 243–253.

(177) Cui, D.; Eriksen, T. E. *Environmental Science & Technology* **1996**, *30*, 2259–2262.

(178) Cui, D.; Eriksen, T. E. *Environmental Science & Technology* **1996**, *30*, 2263–2269.

(179) Burke, I. T.; Boothman, C.; Lloyd, J. R.; Mortimer, R. J. G.; Livens, F. R.; Morris, K. *Environmental Science & Technology* **2005**, *39*, 4109–4116.

(180) Burke, I. T.; Boothman, C.; Lloyd, J. R.; Livens, F. R.; Charnock, J. M.; McBeth, J. M.; Mortimer, R. J.; Morris, K. *Environmental Science & Technology* **2006**, *40*, 3529–3535.

(181) McBeth, J. M.; Lear, G.; Lloyd, J. R.; Livens, F. R.; Morris, K.; Burke, I. T. *Geomicrobiology Journal* **2007**, *24*, 189–197.

(182) Morris, K.; Livens, F. R.; Charnock, J. M.; Burke, I. T.; McBeth, J. M.; Begg, J. D. C.; Boothman, C.; Lloyd, J. R. *Applied Geochemistry* **2008**, *23*, 603–617.

(183) Burke, I. T.; Livens, F. R.; Lloyd, J. R.; Brown, A. P.; Law, G. T. W.; McBeth, J. M.; Ellis, B. L.; Lawson, R. S.; Morris, K. *Applied Geochemistry* **2010**, *25*, 233–241.

(184) Smith, F. N.; Um, W.; Taylor, C. D.; Kim, D. S.; Schweiger, M. J.; Kruger, A. A. *Environmental Science & Technology* **2016**, *50*, 5216–5224.

(185) Yalçintaş, E.; Scheinost, A. C.; Gaona, X.; Altmaier, M. *Dalton Transactions* **2016**, *45*, 17874–17885.

(186) Kumar, S. S.; Himabindu, V. *Materials Science for Energy Technologies* **2019**, *2*, 442–454.

(187) McHugh, P. J.; Stergiou, A. D.; Symes, M. D. *Advanced Energy Materials* **2020**, *10*, 2002453.

(188) Fabbri, E.; Schmidt, T. J. *Acs Catalysis* **2018**, *8*, 9765–9774.

(189) McCrory, C. C. L.; Jung, S.; Ferrer, I. M.; Chatman, S. M.; Peters, J. C.; Jaramillo, T. F. *Journal of the American Chemical Society* **2015**, *137*, 4347–4357.

(190) Chen, J. Y. C.; Dang, L.; Liang, H.; Bi, W.; Gerken, J. B.; Jin, S.; Alp, E. E.; Stahl, S. S. *Journal of the American Chemical Society* **2015**, *137*, 15090–15093.

(191) Schalenbach, M.; Tjarks, G.; Carmo, M.; Lueke, W.; Mueller, M.; Stolten, D. *Journal of the Electrochemical Society* **2016**, *163*, F3197.

(192) Qiao, B.; Wang, A.; Yang, X.; Allard, L. F.; Jiang, Z.; Cui, Y.; Liu, J.; Li, J.; Zhang, T. *Nature Chemistry* **2011**, *3*, 634–641.

(193) Turner, M.; Golovko, V. B.; Vaughan, O. P.; Abdulkin, P.; Berenguer-Murcia, A.; Tikhov, M. S.; Johnson, B. F. G.; Lambert, R. M. *Nature* **2008**, *454*, 981–983.

(194) Kaden, W. E.; Wu, T.; Kunkel, W. A.; Anderson, S. L. *Science* **2009**, *326*, 826–829.

(195) Crespo-Quesada, M.; Yarulin, A.; Jin, M.; Xia, Y.; Kiwi-Minsker, L. *Journal of the American Chemical Society* **2011**, *133*, 12787–12794.

(196) Yang, X.-F.; Wang, A.; Qiao, B.; Li, J.; Liu, J.; Zhang, T. *Accounts of Chemical Research* **2013**, *46*, 1740–1748.

(197) Thomas, J. M.; Raja, R.; Lewis, D. W. *Angewandte Chemie International Edition* **2005**, *44*, 6456–6482.

(198) Thomas, J. M.; Saghi, Z.; Gai, P. L. *Topics in Catalysis* **2011**, *54*, 588–594.

(199) Abbet, S.; Sanchez, A.; Heiz, U.; Schneider, W.-D.; Ferrari, A.; Pacchioni, G.; Rösch, N. *Journal of the American Chemical Society* **2000**, *122*, 3453–3457.

(200) Matthey, D.; Wang, J.; Wendt, S.; Matthiesen, J.; Schaub, R.; Laegsgaard, E.; Hammer, B.; Besenbacher, F. *Science* **2007**, *315*, 1692–1696.

(201) Bruix, A.; Lykhach, Y.; Matolínová, I.; Neitzel, A.; Skála, T.; Tsud, N.; Vorokhta, M.; Stetsovych, V.; Ševčíková, K.; Mysliveček, J., et al. *Angewandte Chemie International Edition* **2014**, *53*, 10525–10530.

(202) Sun, S.; Zhang, G.; Gauquelin, N.; Chen, N.; Zhou, J.; Yang, S.; Chen, W.; Meng, X.; Geng, D.; Banis, M. N., et al. *Scientific Reports* **2013**, *3*, 1–9.

(203) Jiang, K.; Luo, M.; Liu, Z.; Peng, M.; Chen, D.; Lu, Y.-R.; Chan, T.-S.; de Groot, F. M.; Tan, Y. *Nature Communications* **2021**, *12*, 1687.

(204) Zhang, H.; Wei, J.; Dong, J.; Liu, G.; Shi, L.; An, P.; Zhao, G.; Kong, J.; Wang, X.; Meng, X., et al. *Angewandte Chemie* **2016**, *128*, 14522–14526.

(205) Bliem, R.; Pavelec, J.; Gamba, O.; McDermott, E.; Wang, Z.; Gerhold, S.; Wagner, M.; Osiecki, J.; Schulte, K.; Schmid, M.; Blaha, P.; Diebold, U.; Parkinson, G. S. *Physical Review B* **2015**, *92*, 075440.

(206) Gargallo-Caballero, R.; Martín-García, L.; Quesada, A.; Granados-Miralles, C.; Foerster, M.; Aballe, L.; Bliem, R.; Parkinson, G. S.; Blaha, P.; Marco, J. F.; De la Figuera, J. *The Journal of Chemical Physics* **2016**, *144*, 094704.

(207) Ryan, P. T. P. et al. *Physical Chemistry Chemical Physics* **2018**, *20*, 16469–16476.

(208) Jakub, Z.; Hulva, J.; Ryan, P. T.; Duncan, D. A.; Payne, D. J.; Bliem, R.; Ulreich, M.; Hofegger, P.; Kraushofer, F.; Meier, M.; Schmid, M.; Diebold, U.; Parkinson, G. S. *Nanoscale* **2020**, *12*, 5866–5875.

(209) Jakub, Z.; Hulva, J.; Meier, M.; Bliem, R.; Kraushofer, F.; Setvin, M.; Schmid, M.; Diebold, U.; Franchini, C.; Parkinson, G. S. *Angewandte Chemie* **2019**, *131*, 14099–14106.

(210) Meier, M.; Jakub, Z.; Balajka, J.; Hulva, J.; Bliem, R.; Thakur, P. K.; Lee, T.-L.; Franchini, C.; Schmid, M.; Diebold, U., et al. *Nanoscale* **2018**, *10*, 2226–2230.

(211) Bliem, R.; Kosak, R.; Perneczky, L.; Novotny, Z.; Gamba, O.; Fobes, D.; Mao, Z.; Schmid, M.; Blaha, P.; Diebold, U.; Parkinson, G. S. *ACS Nano* **2014**, *8*, 7531–7537.

(212) Bliem, R.; van der Hoeven, J.; Zavodny, A.; Gamba, O.; Pavelec, J.; de Jongh, P. E.; Schmid, M.; Diebold, U.; Parkinson, G. S. *Angewandte Chemie* **2015**, *127*, 14205–14208.

(213) Bliem, R.; van der Hoeven, J. E.; Hulva, J.; Pavelec, J.; Gamba, O.; de Jongh, P. E.; Schmid, M.; Blaha, P.; Diebold, U.; Parkinson, G. S. *Proceedings of the National Academy of Sciences* **2016**, *113*, 8921–8926.

(214) Liao, P.; Keith, J. A.; Carter, E. A. *Journal of the American Chemical Society* **2012**, *134*, 13296–13309.

(215) Gong, M.; Li, Y.; Wang, H.; Liang, Y.; Wu, J. Z.; Zhou, J.; Wang, J.; Regier, T.; Wei, F.; Dai, H. *Journal of the American Chemical Society* **2013**, *135*, 8452–8455.

(216) Smith, R. D.; Prévot, M. S.; Fagan, R. D.; Zhang, Z.; Sedach, P. A.; Siu, M. K. J.; Trudel, S.; Berlinguette, C. P. *Science* **2013**, *340*, 60–63.

(217) Han, L.; Dong, S.; Wang, E. *Advanced Materials* **2016**, *28*, 9266–9291.

(218) Lu, X.-F.; Gu, L.-F.; Wang, J.-W.; Wu, J.-X.; Liao, P.-Q.; Li, G.-R. *Advanced Materials* **2017**, *29*, 1604437.

(219) Ye, S.-H.; Shi, Z.-X.; Feng, J.-X.; Tong, Y.-X.; Li, G.-R. *Angewandte Chemie International Edition* **2018**, *57*, 2672–2676.

(220) Nørskov, J. K.; Rossmeisl, J.; Logadottir, A.; Lindqvist, L.; Kitchin, J. R.; Bligaard, T.; Jonsson, H. *The Journal of Physical Chemistry B* **2004**, *108*, 17886–17892.

(221) Koskinen, P.; Mäkinen, V. *Computational Materials Science* **2009**, *47*, 237–253.

(222) Ashcroft, N. W.; Mermin, N. D., *Solid State Physics*; Saunders College Publishing, Ed., New York, 1976.

(223) Grosso, G.; Parravicini, G. P., *Solid State Physics*; Elsevier Academic Press, Ed., Oxford, 2014.

(224) Pisani, C., *Quantum-Mechanical Ab-initio Calculation of the Properties of Crystalline Materials*; Springer, Ed., Berlin Heidelberg, 1996.

(225) Jensen, F., *Introduction to Computational Chemistry*; Wiley, Ed., Chichester, 2007.

(226) Becke, A. D. *Physical Review A* **1988**, *38*, 3098–3100.

(227) Lee, C.; Yang, W.; Parr, R. G. *Physical Review B* **1988**, *37*, 785–789.

(228) Miehlich, B.; Savin, A.; Stoll, H.; Preuss, H. *Chemical Physics Letters* **1989**, *157*, 200–206.

(229) Perdew, J. P.; Burke, K.; Ernzerhof, M. *Physical Review Letters* **1996**, *77*, 3865–3868.

(230) Becke, A. D. *The Journal of Chemical Physics* **1993**, *98*, 5648–5652.

(231) Perdew, J. P.; Ernzerhof, M.; Burke, K. *The Journal of Chemical Physics* **1996**, *105*, 9982–9985.

(232) Adamo, C.; Barone, V. *The Journal of Chemical Physics* **1999**, *110*, 6158–6170.

(233) Heyd, J.; Scuseria, G. E.; Ernzerhof, M. *The Journal of Chemical Physics* **2003**, *118*, 8207–8215.

(234) Elstner, M.; Porezag, D.; Jungnickel, G.; Elsner, J.; Haugk, M.; Frauenheim, T.; Suhai, S.; Seifert, G. *Physical Review B* **1998**, *58*, 7260.

(235) Foulkes, W. M. C.; Haydock, R. *Physical Review B* **1989**, *39*, 12520–12536.

(236) Seifert, G.; Joswig, J.-O. *Wiley Interdisciplinary Reviews: Computational Molecular Science* **2012**, *2*, 456–465.

(237) Elstner, M.; Seifert, G. *Philosophical Transactions of the Royal Society A: Mathematical, Physical and Engineering Sciences* **2014**, *372*, 20120483.

(238) Wang, Y. X. J. *World Journal of Gastroenterology* **2015**, *21*, 13400–13402.

(239) Kirschvink, J. L.; Jones, D. S.; MacFadden, B. J., *Magnetite Biomineralization and Magnetoreception in Organisms, a New Biomagnetism*; Springer, Ed., New York, 1985.

(240) Krukau, A. V.; Vydrov, O. A.; Izmaylov, A. F.; Scuseria, G. E. *The Journal of Chemical Physics* **2006**, *125*, 224106.

(241) Aradi, B.; Hourahine, B.; Frauenheim, T. *The Journal of Physical Chemistry A* **2007**, *111*, 5678–5684.

(242) Zheng, G.; Witek, H. A.; Bobadova-Parvanova, P.; Irle, S.; Musaev, D. G.; Prabhakar, R.; Morokuma, K.; Lundberg, M.; Elstner, M.; Köhler, C.; Frauenheim, T. *Journal of Chemical Theory and Computation* **2007**, *3*, 1349–1367.

(243) Liu, H.; Seifert, G.; Di Valentin, C. *The Journal of Chemical Physics* **2019**, *150*, 094703.

(244) Hourahine, B.; Sanna, S.; Aradi, B.; Köhler, C.; Niehaus, T.; Frauenheim, T. *The Journal of Physical Chemistry A* **2007**, *111*, 5671–5677.

(245) Liu, H.; Bianchetti, E.; Siani, P.; Di Valentin, C. *The Journal of Chemical Physics* **2020**, *152*, 124711.

(246) Liu, H.; Siani, P.; Bianchetti, E.; Zhao, J.; Di Valentin, C. *Nanoscale* **2021**, *13*, 9293–9302.

(247) Dovesi, R. et al., *CRYSTAL17 User's Manual*, University of Torino, Torino, 2017.

(248) Dovesi, R.; Erba, A.; Orlando, R.; Zicovich-Wilson, C. M.; Civalleri, B.; Maschio, L.; Rérat, M.; Casassa, S.; Baima, J.; Salustro, S.; Kirtman, B. *Wiley Interdisciplinary Reviews: Computational Molecular Science* **2018**, *8*, e1360.

(249) Herng, T. S.; Xiao, W.; Poh, S. M.; He, F.; Sutarto, R.; Zhu, X.; Li, R.; Yin, X.; Diao, C.; Yang, Y.; Huang, X.; Yu, X.; Feng, Y. P.; Rusydi, A.; Ding, J. *Nano Research* **2015**, *8*, 2935–2945.

(250) Gajdoš, M.; Eichler, A.; Hafner, J. *Journal of Physics Condensed Matter* **2004**, *16*, 1141–1164.

(251) Stroppa, A.; Kresse, G. *New Journal of Physics* **2008**, *10*, 063020.

(252) Hulva, J.; Meier, M.; Bliem, R.; Jakub, Z.; Kraushofer, F.; Schmid, M.; Diebold, U.; Franchini, C.; Parkinson, G. S. *Science* **2021**, *371*, 375–379.

(253) Gamba, O.; Noei, H.; Pavelec, J.; Bliem, R.; Schmid, M.; Diebold, U.; Stierle, A.; Parkinson, G. S. *The Journal of Physical Chemistry C* **2015**, *119*, 20459–20465.

(254) Parkinson, G. S.; Mulakaluri, N.; Losovyj, Y.; Jacobson, P.; Pentcheva, R.; Diebold, U. *Physical Review B* **2010**, *82*, 125413.

(255) Mulakaluri, N.; Pentcheva, R. *The Journal of Physical Chemistry C* **2012**, *116*, 16447–16453.

(256) Bourgund, A.; Lechner, B. A.; Meier, M.; Franchini, C.; Parkinson, G. S.; Heiz, U.; Esch, F. *The Journal of Physical Chemistry C* **2019**, *123*, 19742–19747.

(257) Pavarini, E.; Koch, E.; Scalettar, R.; Martin, R., *The Physics of Correlated Insulators, Metals, and Superconductors*, Forschungszentrum Jülich, Jülich, 2017.

(258) Levstein, P. R.; Calvo, R. *Inorganic Chemistry* **1990**, *29*, 1581–1583.

(259) Rodriguez, E. E.; Poineau, F.; Llobet, A.; Sattelberger, A. P.; Bhattacharjee, J.; Waghmare, U. V.; Hartmann, T.; Cheetham, A. K. *Journal of the American Chemical Society* **2007**, *129*, 10244–10248.

(260) Tiana, D.; Hendon, C. H.; Walsh, A. *Chemical Communications* **2014**, *50*, 13990–13993.

(261) Meier, M.; Hulva, J.; Jakub, Z.; Pavelec, J.; Setvin, M.; Bliem, R.; Schmid, M.; Diebold, U.; Franchini, C.; Parkinson, G. S. *Proceedings of the National Academy of Sciences of the United States of America* **2018**, *115*, E5642–E5650.

(262) Guerrero, G.; Alauzun, J. G.; Granier, M.; Laurencin, D.; Mutin, P. H. *Dalton Transactions* **2013**, *42*, 12569–12585.

(263) Lukens, W. W.; Bucher, J. J.; Edelstein, N. M.; Shuh, D. K. *Environmental Science & Technology* **2002**, *36*, 1124–1129.

(264) Oliveira, A. F.; Kuc, A.; Heine, T.; Abram, U.; Scheinost, A. C. *Chemistry–A European Journal* **2022**, *28*, e202202235.

(265) Li, Z.; Chanéac, C.; Berger, G.; Delaunay, S.; Graff, A.; Lefèvre, G. *RSC Advances* **2019**, *9*, 33633–33642.

(266) Bianchetti, E.; Di Valentin, C. *Materials Today Nano* **2022**, *17*, 100169.

(267) Monkhorst, H. J.; Pack, J. D. *Physical Review B* **1976**, *13*, 5188–5192.

(268) Rehr, J. J.; Albers, R. C. *Reviews of Modern Physics* **2000**, *72*, 621.

(269) Rehr, J. J.; Kas, J. J.; Prange, M. P.; Sorini, A. P.; Takimoto, Y.; Vila, F. *Comptes Rendus Physique* **2009**, *10*, 548–559.

(270) Rehr, J. J.; Kas, J. J.; Vila, F. D.; Prange, M. P.; Jorissen, K. *Physical Chemistry Chemical Physics* **2010**, *12*, 5503–5513.

(271) Magneli, A.; Siitonen, S.; Skrifvars, B.; Schliack, J.; Reio, L. *Acta Chemica Scandinavica* **1957**, *11*.

(272) Ivanovskii, A. L.; Chupakhina, T. I.; Zubkov, V. G.; Tyutyunnik, A. P.; Krasilnikov, V. N.; Bazuev, G. V.; Okatov, S. V.; Lichtenstein, A. I. *Physics Letters A* **2005**, *348*, 66–70.

(273) Doudin, N.; Yuk, S. F.; Marcinkowski, M. D.; Nguyen, M. T.; Liu, J. C.; Wang, Y.; Novotny, Z.; Kay, B. D.; Li, J.; Glezakou, V. A.; Parkinson, G. S.; Rousseau, R.; Dohnálek, Z. *ACS Catalysis* **2019**, *9*, 7876–7887.

(274) Zachara, J. M.; Heald, S. M.; Jeon, B.-H.; Kukkadapu, R. K.; Liu, C.; McKinley, J. P.; Dohnalkova, A. C.; Moore, D. A. *Geochimica et Cosmochimica Acta* **2007**, *71*, 2137–2157.

(275) Ladbury, J. W.; Cullis, C. F. *Chemical Reviews* **1958**, *58*, 403–438.

(276) Skomurski, F. N.; Rosso, K. M.; Krupka, K. M.; McGrail, B. P. *Environmental Science & Technology* **2010**, *44*, 5855–5861.

(277) Wang, G.; Olszta, M. J.; Saslow, S. A.; Kim, D.-S.; Bowden, M. E.; Um, W.; Wang, J.; Kruger, A. A. *ACS Earth and Space Chemistry* **2021**, *5*, 525–534.

(278) Montoya, J. H.; Seitz, L. C.; Chakthranont, P.; Vojvodic, A.; Jaramillo, T. F.; Nørskov, J. K. *Nature Materials* **2017**, *16*, 70–81.

(279) Lyons, M.; Brandon, M. *International Journal of Electrochemical Science* **2008**, *3*, 1386–1424.

(280) Trotochaud, L.; Ranney, J. K.; Williams, K. N.; Boettcher, S. W. *Journal of the American Chemical Society* **2012**, *134*, 17253–17261.

(281) Gao, M.; Sheng, W.; Zhuang, Z.; Fang, Q.; Gu, S.; Jiang, J.; Yan, Y. *Journal of the American Chemical Society* **2014**, *136*, 7077–7084.

(282) Kubisztal, J.; Kubisztal, M. *Catalysts* **2022**, *12*, 21.

(283) Gebreslase, G. A.; Martínez-Huerta, M. V.; Lázaro, M. J. *Journal of Energy Chemistry* **2022**, *67*, 101–137.

(284) Li, Y.-F.; Selloni, A. *ACS Catalysis* **2014**, *4*, 1148–1153.

(285) Marcinkowski, M. D.; Yuk, S. F.; Doudin, N.; Smith, R. S.; Nguyen, M.-T.; Kay, B. D.; Glezakou, V.-A.; Rousseau, R.; Dohnálek, Z. *ACS Catalysis* **2019**, *9*, 10977–10982.

(286) Zhao, Z.-J.; Liu, S.; Zha, S.; Cheng, D.; Studt, F.; Henkelman, G.; Gong, J. *Nature Reviews Materials* **2019**, *4*, 792–804.

(287) Liang, Q.; Brocks, G.; Bieberle-Hütter, A. *Journal of Physics: Energy* **2021**, *3*, 026001.

(288) Tkalych, A. J.; Zhuang, H. L.; Carter, E. A. *ACS Catalysis* **2017**, *7*, 5329–5339.

(289) Song, J.; Wei, C.; Huang, Z.-F.; Liu, C.; Zeng, L.; Wang, X.; Xu, Z. J. *Chemical Society Reviews* **2020**, *49*, 2196–2214.

(290) Rossmeisl, J.; Logadottir, A.; Nørskov, J. K. *Chemical Physics* **2005**, *319*, 178–184.

(291) Rossmeisl, J.; Qu, Z.-W.; Zhu, H.; Kroes, G.-J.; Nørskov, J. K. *Journal of Electroanalytical Chemistry* **2007**, *607*, 83–89.

(292) Man, I. C.; Su, H.-Y.; Calle-Vallejo, F.; Hansen, H. A.; Martínez, J. I.; Inoglu, N. G.; Kitchin, J.; Jaramillo, T. F.; Nørskov, J. K.; Rossmeisl, J. *ChemCatChem* **2011**, *3*, 1159–1165.

(293) Grimaud, A.; Hong, W. T.; Shao-Horn, Y.; Tarascon, J.-M. *Nature Materials* **2016**, *15*, 121–126.

(294) Grimaud, A.; Diaz-Morales, O.; Han, B.; Hong, W. T.; Lee, Y.-L.; Giordano, L.; Stoerzinger, K. A.; Koper, M.; Shao-Horn, Y. *Nature Chemistry* **2017**, *9*, 457–465.

(295) Righi, G.; Plescher, J.; Schmidt, F.-P.; Campen, R. K.; Fabris, S.; Knop-Gericke, A.; Schlögl, R.; Jones, T. E.; Teschner, D.; Piccinin, S. *Nature Catalysis* **2022**, 1–12.

(296) Avcí, Ö. N.; Sementa, L.; Fortunelli, A. *ACS Catalysis* **2022**, *12*, 9058–9073.

(297) Peden, C. H.; Herman, G. S.; Ismagilov, I. Z.; Kay, B. D.; Henderson, M. A.; Kim, Y.-J.; Chambers, S. A. *Catalysis Today* **1999**, *51*, 513–519.

(298) Kendelewicz, T.; Liu, P.; Doyle, C.; Brown Jr, G.; Nelson, E. J.; Chambers, S. A. *Surface Science* **2000**, *453*, 32–46.

(299) Rustad, J. R.; Felmy, A. R.; Bylaska, E. J. *Geochimica et Cosmochimica Acta* **2003**, *67*, 1001–1016.

(300) Mulakaluri, N.; Pentcheva, R.; Scheffler, M. *The Journal of Physical Chemistry C* **2010**, *114*, 11148–11156.

(301) Parkinson, G. S.; Novotný, Z.; Jacobson, P.; Schmid, M.; Diebold, U. *Journal of the American Chemical Society* **2011**, *133*, 12650–12655.

(302) Kendelewicz, T.; Kaya, S.; Newberg, J.; Bluhm, H.; Mulakaluri, N.; Moritz, W.; Scheffler, M.; Nilsson, A.; Pentcheva, R.; Brown Jr, G. *The Journal of Physical Chemistry C* **2013**, *117*, 2719–2733.

(303) Liu, S.; Wang, S.; Li, W.; Guo, J.; Guo, Q. *The Journal of Physical Chemistry C* **2013**, *117*, 14070–14074.

(304) Plimpton, S. *Journal of Computational Physics* **1995**, *117*, 1–19.

(305) Sun, H. *The Journal of Physical Chemistry B* **1998**, *102*, 7338–7364.

(306) Heinz, H.; Lin, T.-J.; Kishore Mishra, R.; Emami, F. S. *Langmuir* **2013**, *29*, 1754–1765.

(307) Zhao, L.; Liu, L.; Sun, H. *The Journal of Physical Chemistry C* **2007**, *111*, 10610–10617.

(308) Siani, P.; Khandelia, H.; Orsi, M.; Dias, L. G. *Journal of Computer-Aided Molecular Design* **2018**, *32*, 1259–1271.

(309) Siani, P.; Bianchetti, E.; Liu, H.; Di Valentin, C. *The Journal of Chemical Physics* **2021**, *154*, 034702.

(310) Grimme, S. *Journal of Computational Chemistry* **2006**, *27*, 1787–1799.

(311) Grimme, S.; Antony, J.; Ehrlich, S.; Krieg, H. *The Journal of Chemical Physics* **2010**, *132*, 154104.

(312) Grimme, S.; Ehrlich, S.; Goerigk, L. *Journal of Computational Chemistry* **2011**, *32*, 1456–1465.

(313) Hu, H.; Lu, Z.; Elstner, M.; Hermans, J.; Yang, W. *The Journal of Physical Chemistry A* **2007**, *111*, 5685–5691.